UNIVERSIDAD DE LAS AMÉRICAS PUEBLA

School of Sciences

Department of Chemical Biological Sciences

Synthesis and characterization of $Ni_{1-x}Zn_xFe_2O_4$-chitosan-PVA nanofibers and evaluation of their performance as a magnetic hyperthermia agent

Thesis presented to fulfill the requirements of the Honors Program by the student

Ricardo González Hidalgo

ID 171271

Bachelor in Nanotechnology and Molecular Engineering

Dr. Miguel Ángel Méndez Rojas

San Andrés Cholula, Puebla Fall, 2024

Signature Sheet

Thesis presented to fulfill the requirements of the Honors Program by the student Ricardo González Hidalgo, ID 171271

Thesis Advisor

_____

Dr. Miguel Ángel Méndez Rojas

Thesis President

_____

Dr. Mónica Cerro López

Thesis Secretary

_____

Dr. Ricardo Navarro Amador

Acknowedgements

I extend my heartful gratitute to Dr. Miguel Ángel Méndez Rojas, Professor from the Department of Biological-Chemical Sciences and Advisor of my thesis, who gave me the opportunity to pursue this research project and provided me all the necessary tools for its optimal development.

I also express my appreciaton to Dr. Sergio Alberto Sabinas Hernández, Professor from the Physics Institute of BUAP, for his support on the methodology and characterization concerning the nanofibers systems. Additionally, I am indebted to Dr. Ulises Salazar Kuri and Lupita, who helped me with the XRD characterization of all my samples and gave me laboratory support.

I am very grateful to all my friends, colleagues and professors for the support and learnings they have given me. To Maryfer, Ángel, Anna, Ramón, Rodrigo, and Anouk, who backed me up during my career and thesis development.

Special thanks go to my partner, Nicole, who assisted me in creating schematic representations of my methodology steps and SEM characterizations, giving me persistent emotional and academic support, and encouraging me throughout this project.

Finally, I would like to express my deepest gratitude to my family, my sister Sandy, my mother Luisa, and my father Demetrio, for his unwavering support and encouragement during my academic pursuits. Their love and guidance have been my greatest source of strength and passion.

Ricardo González Hidalgo

Index

1. Introduction

Being one of the most well-known, urgent, incapacitating and deadly diseases impacting to many individuals and communities, cancer is the second leading cause of death worldwide at all income levels (Jean-Pierre & McDonald, 2016). This affection develops overtime, accumulating mutations and genetic changes in cells designated as the "hallmarks of cancer" (Figure 1), such as sustained proliferative ability, evasion of growth supressors, resistance to cell death, avoiding immune destruction, and the ability to invade and metastasize (Colobatiu et al., 2021), (Licciulli, 2022).

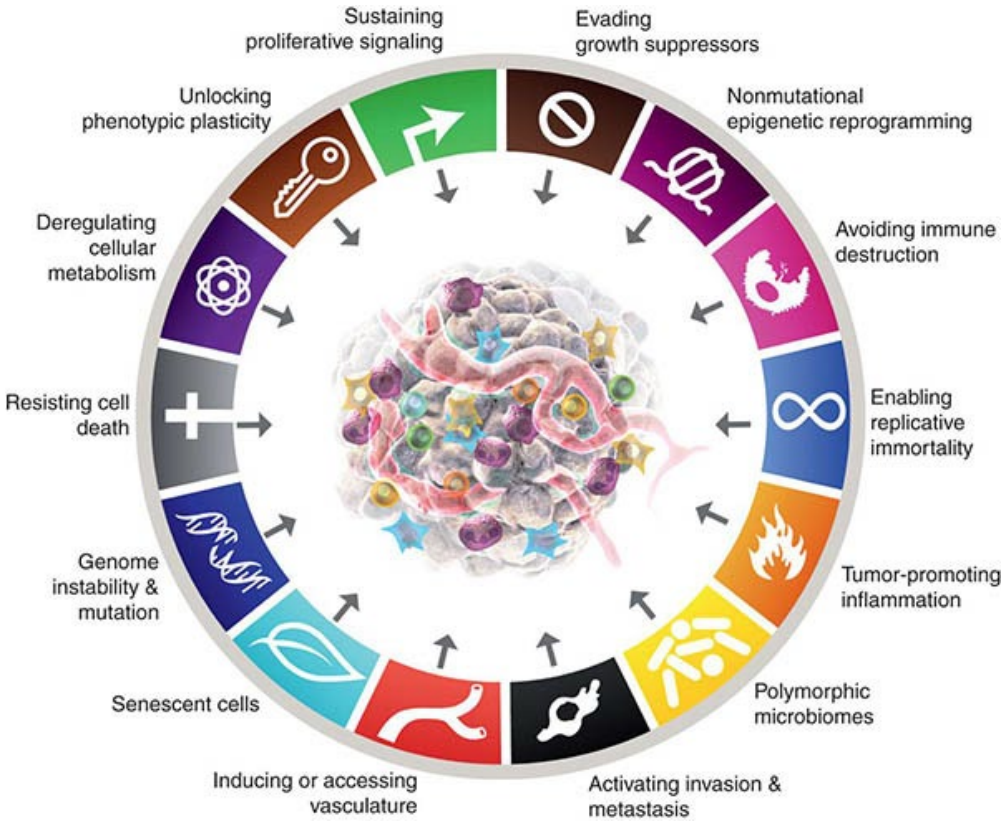

Figure 1. Hallmarks of cancer (Licciulli, 2022).

In depth, the originally proposed "cancer hallmarks" by Hanahan and Weinberg (2000) included six main characteristics: (i) self-sufficiency in growth signals (cancer cells generate

most of growth signals with no dependence on external stimuli); (ii) intensitivity to growth suppressive signals (antiproliferative signals maintaining homeostasis in normal tissues are evading by cancer cells); (iii) ability to evade programmed cell death; (iv) enabling replicative immortality (telomerase enzyme in cancer cells keeps their telomeres above a critical threshold so they proliferate indefinitely by division); (v) sustained angiogenesis (increased oxygen and nutrients allows them to grow vasculature from microscopic to macroscopic lessions); (vi) tissue invasion and metastasis (Mitra et al., 2024) (Licciulli, 2022).

Additional hallmarks have been added to the previous marks, being emerging characteristics like reprogramming energy metabolism (cancer cells can switch to aerobic glycolysis even in presence of oxygen), evading immune destruction (Hanahan & Weinberg, 2011), and phenotypic plasticity and disrupted differentiation (malignant cells can modify their indentity into something that is more likely to proliferate by cellular plasticity) (Hanahan, 2022).

With increasing knowledge about the disease, different treatments have been proposed to overcome the challenges. Conventional therapies like surgery, radiation therapy, and chemotherapy, as well as nonconventional or complementary therapeutic methods such as hormone therapy, neoadjuvant therapy, immune therapy, gene therapy and tagerted therapy, have been widely used, still with important flaws. Of these, the major disadvatages are low efficiency, nonspecificity, adverse side effects, largely distress and toxicity to healthy cells, organs and tissues, unfavorable pharamacokinetcis, poor absorption, and high-cost. Besides, it is highly dependent on indivual characteristics, such as cancer kind and stage,

tumor features, and the patient's age, health and preferences (Chandraprasad et al., 2022), (Mitra et al., 2024).

Novel therapies based on nanotechnology techniques are being developed to perform better results when dealing with different types of cancer in terms of therapeutic delivery, diagnostics, radiation therapy and imaging modalities. Then, important advantages can be obtained, such as enhanced imaging, faster diagnosis, decrease radiation exposure, lowered toxicity, increased therapeutic efficiency, multi-functionality, and allowance to combined therapies with theranostic systems (Kemp & Kwon, 2021).

In this thesis, a nanosystem of core-shell nanofibers of chitosan (Ch) coupled with PVA containing magnetic ferrite nanoparticles (MNPs) as core and ε-polycaprolactone (PCL) as shell is proposed as an agent of magnetic hyperthermia to act as a novel cancer nanotherapy. Furthermore, the Ni-Zn ferrite nanoparticles are made by a co-precipitation method using nitrate precursors, while the core-shell nanofibers are prepared using coaxial electrospinning.

Additionally the system is phyisicochemically characterized by SEM, EDS, TEM, XRD, Raman, FTIR, and TGA, and its performance as a bi-functional therapy is studied with UV-Vis spectrophotometry for drug encapsulation efficiency and delivery and with a magnetometer (MagneTherm) to evaluate its performance for magnetic hyperthermia.

2. Justification

Over the years, nanotechnology has been considered for a great part of the scientific community as a novel and viable option to reduce and solve main and demanding issues. The possibility to control and manipulate matter on a nanometer scale, allows us to create and

reveal new technological and scientific (Sabbas, 2014). Specifically, nanoparticles (NPs) range their dimensions size up to 100 nm and are broadly used in physical, chemical, biomedical, and biotechnological research, mainly due to high surface area-volume ratio, high reactivity, magnified diffusion, and easy post-synthetic modification (Sabbas, 2014) (Kush et al., 2021).

A relatively recent topic that has promising future and research is the transport and delivery of drugs using magnetic biocompatible nanoparticles as nanocarriers. This application allows scientists to reduce toxic and side effects of drugs while effectiveness and accuracy are improved. According to Popescu (2011) the main goal of drug delivery is "to guide the administration of a given drug to a specific locus within a particular population of cells in an organ or tissue". Then, nanoparticles are used in drug delivery systems in order to improve the uptake of poorly soluble drugs, the targeting of drugs to specific sites, and drug bioavailability (Suri et al., 2007).

Furthermore, Kim et al. (2012) stablish that nano-based drug delivery systems can reduce undesirable effects of current chemotherapeutics, such as lack of aqueous solubility, multidrug resistance, and relative lack of specificity (drugs attack both target and non-target cells). Additionally, NPs can improve pharmacotherapy by altering pharmacokinetics of conventional and new drugs, and so, increasing drug retention time, reducing toxicity, and increasing the half-life of drugs.

Sabbas (2014) mentioned that stability, non-toxicity, non-immunogenicity, and biocompatibility can be obtained by adding a biocompatible coating. Considering that one of the major issues of NPs application in drug delivery systems, is that they tend to agglomerate, it is necessary to modify its surface with biocompatible coatings to prevent it. Some of most

widely used components for coating are carboxylates, phosphates, sulfates, silica, gold, dextran, polysaccharides, polyvinyl butyral, poly (methyl methacrylate), polyesters, chitosan, polyethylene glycol, and polyvinyl alcohol (Mohammadi et al., 2021). It is worth to mention that, in this work, polymer-coated magnetic nanoparticles (MNPs) systems will be the most studied.

Yang et al. (2017) also proposed that drug delivery systems (DDS) should be able to cross different biological barriers in the body, depending on which is the targeted tissue and its ease of access. There are so many parameters to consider when drug delivery across biological barriers is sought, such as thickness, water content, whether is free of living cells or composed of connected cells, etc. Then, DDS requirements must be studied individually for each biological barrier, given that problems to overcome and design characteristics depend in large part on the specific barrier and the associated organ systems.

On the other hand, among many cancer therapies, magnetic hyperthermia (MH) presents a novel and effective alternative approach for the focal treatment of tumors, having as its basis the generation of heat by MNPs reacting to an alternating magnetic field (AMF). In order to improve the antitumor therapeutic efficiency, optimizations in size, composition, morphology, and surface of MNPs must be performed while synergistically combining it with different other strategies to enhance the performance (Liu et al., 2020). Thus, a bi-functional DDS with triggerable delivery dependent of magnetic hyperthermia is proposed as a potential novel theragnostic nanomaterial.

3. Objectives

3.1 General objective

Create a novel nanosystem of core-shell maganetic nanofibers containing $Ni_{1-x}Zn_xFe_2O_4$ nanoparticles coupled with chitosan (Ch) and polyvinyl alcohol (PVA) as core and ε-polycaprolactone (PCL) as shell for acting as an agent of magnetic hyperthermia.

3.2 Specific objectives

- Synthesize the core-shell magnetic nanofibers system using the co-precipitation method for the magnetic nanoparticles preparation and coaxial electrospinning for the creation of the core-shell nanofibers.
- Characterize the core-shell magnetic nanofibers system in terms of physicochemistry (size, crystallinity, shape, magnetism) using SEM, EDX, FTIR, Raman, XRD, and DLS.
- Evaluate their performance acting as an agent of magnetic hyperthermia.

4. Theoretical background

4.1 Magnetic Nanoparticles – An Overview

Magnetic nanoparticles (MNPs) are one of the most suitable nanomaterials for biomedical, medical, and pharmaceutical research. They are defined as nanoparticles prepared from metal compounds, such as iron (Fe), nickel (Ni), cobalt (Co), gold (Au), and titanium (Ti); ferrites and metal oxides, such as magnetite (Fe_3O_4) and maghemite (γFe_2O_3) (Binandeh et al., 2021).

However, nickel and cobalt are toxic and susceptible to oxidation, thus, for medical and biomedical applications, ferrites and metal oxides are the best options (Acklin & Lautens, 2012).

Furthermore, MNPs are synthesized and dispersed into homogenous suspensions, such as ferrofluids and magnetic fluids. The materials used to synthesize MNPs are classified into 5 main types: ferromagnetic, paramagnetic, diamagnetic, antiferromagnetic, and ferrimagnetic (Issa et al., 2013). MNPs characteristics like size uniformity, size dispersion, surface area, adsorption kinetics, biocompatibility, superparamagnetism, and magnetic moment can be tuned during the synthesis process, so these will influence the MNPs properties. In addition, these MNPs will require special surface coating to be applied, which consists of non-toxic and biocompatible materials that allow target delivery with particle localization in a specific area (Acklin & Lautens, 2012).

It should be mentioned that magnetic nanoparticles (MNPs) must possess monodispersity, superparamagnetism, stability, and biocompatibility to act as an effective therapeutic system (J.-E. Kim et al., 2012). Superparamagnetism is "one type of magnetism that occurs in ferromagnetic and ferrimagnetic nanostructures" (Bhattacharya, 2021), and can be shown when the grain size is below 20 nm. Superparamagnetic NPs exhibit fast response to the changes of the external magnetic field without displaying remnant or residual magnetization (Mr) and zero coercivity, meaning that additional magnetic field to return magnetization down to 0 is not needed (Gupta & Tripathi, 2012), (Mosquera et al., 2015).

Besides, superparamagnetism is strongly dependent of thermal effects, then, this property will only be displayed when temperature is above a specific value called blocking temperature (TB), which is specific for every system (Gupta & Tripathi, 2012). Additionally,

superparamagnetism is important to deliver therapeutics onto specific sites under the influence of an external magnetic field and then, being removed without leaving remanence and by only suppressing the magnetic field (Reddy et al., 2012).

4.1.1 Preparation procedures

The MNPs preparation methods can be generally classified as physical/mechanical, chemical, biological, and microfluidics. All these types of methods have common disadvantages on general aspects like costs, scalability and particle size, and distribution control, thus, the selection will depend on the researcher's preferences and objectives. The physical/mechanical methods are mainly referred as procedures that synthesize nanoparticles up to the bulk metal, for example, mechanical polishing, laser ablation, laser-induced pyrolysis, electron beam lithography, or gas-phase deposition. However, these methods are sophisticated and give a low performance, thus, they usually are not viable for industries, preferring environment-friendly, cheap, and high production methods like ball milling. Unfortunately, it has limits in different aspects like particle size distribution, functionalization, and optimization to biological applications (Kush et al., 2021), (Zhou et al., 2016).

On the other hand, chemical procedures are usually preferred due to better control in particle size, shape, and distribution. These methods involve NPs production from nucleation, growth, and condensation. Some examples are chemical co-precipitation, hydrothermal method, thermal decomposition in organic media, microemulsions method, condensation by vaporization, oxidation-precipitation, sol-gel method, non-aqueous solvent

synthesis method, high-temperature pyrolysis method, among others (Kush et al., 2021), (Zhou et al., 2016).

Furthermore, biological methods were developed because of the recent concern about manufacturing clean, non-toxic, and environmentally friendly solvents and chemicals. They are focused on using bacteria, fungus, bio-derived chemicals, and plant extracts on the biosynthesis of magnetic nanoparticles. This method provides benefits like bio-combability with pharmaceutical, biological and biochemical applications, without using high pressure, energy, temperature, and toxic chemicals on the MNPs preparation (Sabri et al., 2016).

Finally, according to the definition proposed by George Whitesides (2009) as cited by (Niculescu et al., 2021), microfluidics is "the science and technology of systems that process and manipulate small (10^{-9} to 10^{-18} L) amounts of fluids using channels with dimensions of tens to hundreds of micrometers". This method is classified into two main microreactors with the flow pattern manipulation as a variable: Single-phase flow (continuous flow) and multi-phase flow (droplet-based), which is divided into Gas-liquid segment flow and Liquid-liquid segment flow. Besides, they are portable, low-cost, disposable, and allow precise control of fluid mixing, efficient mass transport, improved heat transfer, ease of automation, and reduced reaction time, aspects that influence the size control and distribution of MNPs.

The next table, proposed by Kush et al. (2021), presents all four main preparation methods, and it shows a short comparative analysis between some of the most important aspects to consider when magnetic nanoparticles will be prepared:

Table 1. Comparative analysis between physical, chemical, biological, and microfluidics methods for the preparation of MNPs (Kush et al., 2021).

Synthesis process	Properties							
	Yield	**Reproductivity**	**Scalability**	**Stability**	**Safety**	**Size**	**Size distribution**	**Optimization**
Physical	Very high	Fair	Very good	Poor	Poor	Small	Small	Very poor
Chemical	High	Poor	Good	Very good	Good	Small	Small	Good
Biological	Low	Poor	Very good	Poor	Very good	Very small	High	Poor
Microfluidics	High	Fair	Poor	Good	Very good	Very small	High	Very good

4.1.2 Remarkable synthesis methods

- Chemical co-precipitation (Chemical)

This method consists of the precipitation of ferric and ferrous precursors (in the case of magnetite) by the addition of a base to a solution of different sources of iron. The first stage involves adding a base (usually NaOH or NH_4OH) to a solution containing a mixture of two sources of iron (chlorides, sulfates, and nitrates are the most common iron (III) and iron (II) sources used). After the mixing and reaction of the solution and the alkaline precipitation, it must be done centrifugal separation or magnetic decantation. Then it is washed, dried, and ground, obtaining finally the magnetic nanoparticle. The main advantage of this method is that the simple synthetic procedures used in the treatment can be magnified to an industrial

scale, making the reproduction more feasible and efficient (Kush et al., 2021), (Zhou et al., 2016), (Mosquera et al., 2015)

- Sol-gel method (Chemical)

This method is based on inorganic polymerization reactions with an alkoxide metal like aluminate, titanite, borate, silicate, or thiosulfate as the precursor. It involves the transition of a solution from a liquid "sol" into a solid "gel" phase, where the initial substance to produce the sol is usually alkoxide metals. It is made in 4 stages: hydrolysis, polycondensation, drying, and thermal decomposition. The hydrolysis of the precursor alkoxide metal takes place with water or alcohols, besides if an acid or a base is added, hydrolysis occurs faster. The solvent is removed after the polycondensation and to decompose the organic precursor, calcination is needed. Also, the size and the surface morphology of the MNPs depend on the solution composition, nature, and concentration of the metallic pH and temperature. The main advantages of this method are, that the initial reaction is realized in ambient conditions, the product results are homogenous, it is easy to make multi-component materials and it has good control over powder particle size, shape, and distribution (Kush et al., 2021), (Gupta & Tripathi, 2012), (Mosquera et al., 2015).

- Microemulsion technique (Chemical)

Also known as nanoreactors, microemulsions are thermodynamically stable, optically isotropic solutions of two immiscible liquids (polar and non-polar). The solution is stabilized by a surfactant, providing a micro-heterogenous medium for nanoparticles generation. The emulsion contains oil and water, and it can be presented in two forms: direct (oil dispersed in water, O/W) or reversed (water dispersed in oil, W/O). It is formed a monolayer called

micelle by the two immiscible liquids and the surfactant, and the structure of it depends on the emulsion type (Kush et al., 2021), (Gupta & Tripathi, 2012).

Furthermore, the direct micelle is formed in an aqueous medium, the hydrophobic hydrocarbon chains or "tails" of the surfactant are oriented toward the interior, and the hydrophilic "head" groups of them are in the aqueous phase. On the other hand, the reverse micelles are formed in a non-aqueous medium, the hydrophobic surfactant chains are oriented outward, and the hydrophilic groups are directed toward the core. However, the stability of the emulsion tightly depends on the particle size, particle-particle interaction, particle-water interaction, and particle-oil interaction (Kush et al., 2021), (Gupta & Tripathi, 2012).

- Thermal decomposition in organic media (Chemical)

Thermal decomposition is a method to synthesize stable monodispersed nanoparticles. Monodisperse means that the nanoparticles have a defined and unique molecular size in all monomer sequences. First, the decomposition of iron organic precursors as cuprates or carboxylates takes place at high temperatures. Then, the product is injected into a solution of organic solvents (typically phenyl ether) in the presence of surfactants like oleic acid (Sabbas, 2014a). After the thermal decomposition, the product must be centrifugated to separate the colloidal nanoparticles from the precipitates and clean the nanoparticles until the product is completely homogeneous (Odularu, 2018).

Then, nanoparticles drying can be done by alcohol drying (chemical extraction), freeze-drying (nonthermal), or in a vacuum oven (thermal) at a temperature less than 100ºC. The main variables to control the nanometric size are the duration of synthesis, temperature, reactants concentration, stabilizers, capping agents (surfactants), and types of surfactants.

Also, the temperature and pressure at which thermal decomposition occurs turn on the nature of the metallic ion and the force of the reaction. Among its advantages are fast development, economic and it's easy to synthesize monodispersed metal nanoparticles (Odularu, 2018). However, it has been observed that the synthesis of nanoparticles with this method in organic solutions restricts their applications in biology and medicine (Kush et al., 2021).

4.1.3 Characterization techniques

The main MNPs aspects studied in characterization methods are shape and size, however, these processes can be used to study more parameters, such as elemental-chemical composition, crystal structure, chemical state-oxidation state, growth kinetics, ligand binding/composition/density/arrangement/mass and surface composition, surface area, specific surface area, surface change, concentration, agglomeration state, density, single-particle properties, 3D visualization, dispersion of NP in matrices/supports, structural defects, detection of NPs, optical properties, and magnetic properties (Sabbas, 2014).

Nowadays, it can be applied a lot of characterization methods, and just like synthesis processes, choosing one will depend on the researcher's preferences, parameters, and objectives. However, it has been established special functions for typical methods, for example, electron and atomic force microscopies (AFM) are used for actual visualization of nanoparticles size, shape, and surface morphology; dynamic light scattering (DLS) and zeta potential measurement usage is for determining the size and surface charge of nanoparticles; some X-ray diffraction techniques are used to establish the crystal structure; to make some other elemental analyses of nanoparticles and nanostructures are used energy-dispersive X-ray spectroscopy and X-ray photoelectron spectroscopy, spectroscopic techniques such as

Fourier transform infrared spectroscopy (FTIR), Matrix-assisted laser desorption/ionization-Time of flight Mass spectrometry (MALDI-TOF MS), UV-visible spectroscopy, Rutherford back-scattering spectrometry, dual-polarization interferometry, and nuclear magnetic resonance techniques (Pande & Bhaskarwar, 2016).

The main techniques for characterization of magnetic properties are Superconducting quantum interference device magnetometry (SQUID), Vibrating sample magnetometry (VSM), Mössbauer spectroscopy, Ferromagnetic resonance (FMR), X-ray magnetic circular dichroism (XMCD), Magnetic susceptibility, Magnetophoretic mobility, and Superparamagnetic relaxometry (SPMR) (Mourdikoudis et al., 2018). Kush et al. (2021) synthesize several of them into a table with the main properties, advantages, and limitations of each one; properties and functions of some techniques will be complemented according to (Pande & Bhaskarwar, 2016),) (Mourdikoudis et al., 2018).

4.1.4 Remarkable characterization methods

- X-Ray Diffraction (XRD)

XRD is one of the most common and useful characterization methods for MNPs. It can be analyzed different structure parameters like crystal growth, crystal selection, and mounting, reflection intensity measurement, crystal structure solution, nature of the phase, lattice parameters, and crystalline grain size. Modern X-ray diffraction systems are mainly conformed by: X-ray, goniometer, detector, and a computer equipped with the software required to run the diffractometer. To initiate this method, first, it must be grown a good quality and suitable size (between 50 and 600 microns) crystal (Mourdikoudis et al., 2018), (Shih, 2013).

Then, the crystal must be mounted into the goniometer and affixed to the diffractometer to be exposed to an intense beam of X-ray, producing a pattern of diffractions points known as reflections. Subsequently, data is collected by the computer software (usually SHELXTL) with a charge-coupled device (CCD) or image plate (IP) (Mourdikoudis et al., 2018). This technique is limited by the crystal size require, given that it must be large to increase the diffraction efficiency and observe enough diffraction points to characterization (Kush et al., 2021), (Shih, 2013).

- Fourier-Transform Infrared Spectroscopy (FTIR)

This technique is based on the principle that each molecular vibration can absorb unique infrared radiation in the range of the electromagnetic field. Infrared radiation (IR) is an electromagnetic radiation with frequencies between 14600 and 20 cm^{-1} (Moore, 2016). The spectrum obtained from measurements of absorption radiations will show bands related to the strength and nature of bonds, and specific functional groups, providing information about molecular structures and interactions. There have been established the frequencies at characteristic functional groups in nanoparticles surface present bands, then it is easier to determine the nanoparticle structure and interactions (Mourdikoudis et al., 2018).

- UV-Vis Spectrophotometry (UV-Vis)

This technique measures the intensity of light reflected from a sample and compares it to the intensity of light reflected from reference material. As XRD, with this technique, is obtained a spectrum, and to characterize, the band's strength and wavelength must be interpreted. NPs optical properties are sensitive to size, shape, concentration, agglomeration state, and

refractive index near the NP surface, making UV-Vis important to characterize and evaluate the stability of NP colloidal structure (Mourdikoudis et al., 2018).

- Dynamic Light Scattering (DLS)

Also known as Photon Correlation Spectroscopy (PCS), DLS is an analytical technique used to size MNPs in liquid phase. It measures light scattering as a function of time and is used to calculate the hydrodynamic diameter in solution with the Stokes-Einstein assumption. The method consists of the exposure of a light beam or an electromagnetic wave on the MNPs, then, the direction and the intensity of the light are modified as an action known as scattering. The intensity variation in function of time will be used to determinate the diffusion coefficient of the particles. For spherical forms, it can be used the Stokes-Einstein equation to calculate the hydrodynamic radius (R_H):

$$D_f = \frac{k_B T}{6\pi\eta R_H} \tag{1}$$

Where D_f is the diffusion coefficient (m^2/s), k_B is the Boltzmann's constant ($1.38E^{-23}J/K$), T is the temperature of suspension (K), η is the solvent viscosity (kg/ms), and R_H is the hydrodynamic radius.

The preciseness of this method depends on parameters such as the concentration of particles suspension, scattering angle, and shape anisotropy of nanoparticles. The main benefits of this technique are the reduced time for measuring and the automatization, thus, large experience is not required, and the routine is less labor intensive. Also, the technique is non-invasive and the processed MNPs can be recycled for other purposes (Mourdikoudis et al., 2018), (Lim et al., 2013).

- Transmission Electron Microscopy (TEM)

TEM is a powerful technique that can provide a high imaging resolution down to sub-angstrom level (considered as the best imaging technique when it comes to resolution), structural information through electron diffraction and chemical composition information through the interactions of high-energy electrons with core electrons of the specimen [23]. It is used to analyze interactions between a uniform current density electron beam and a thin sample. Due to the providing of direct images of NPs and an accurate estimation of NPs homogeneity, this technique is the most common to analyze NPs size and shape, defining many physical, optical, magnetic, electronic and catalytic properties (Mourdikoudis et al., 2018). The microscope resolution can be denoted as (Luo, 2016):

$$\delta = \frac{0.61\lambda}{n sin\alpha} \tag{2}$$

Where δ is the resolution, λ is the wavelength of the energy source, n is the refractive index of the medium between the lens and the sample, and α is the semi-angle of collection of magnifying lenses.

An application of this method that can be relevant for this work is that it is widely used for analyzing the interaction between MNPs and cells in biomedical and therapeutic applications, such as drug delivery. Furthermore, it can be found the High-resolution TEM, which is an imaging mode of TEM commonly used to characterize the internal structure of NPs. Also, it can be used to identify structural defects of single crystals that can explain undesirable and unusual properties. Some limitations of TEM are that it is difficult to quantify

many NPs and there are some orientation effects that affects the resulting images (Mourdikoudis et al., 2018).

- Scanning Electron Microscopy (SEM)

SEM is a technique used to obtain high-resolution imaging of surfaces that can be employed to characterize NPs. Instead of using light as a conventional microscope, SEM uses electrons for imaging. Some differences between SEM and TEM, are that TEM uses electrons transmitted through specimens, convex lenses, and elastically scattered electrons for imaging; and SEM uses electrons emitted from surfaces of specimens on the same side as electron incidence, and inelastically scattered electrons with energy less than 50 eV for imaging. Similar as TEM technique, it was developed a High-resolution SEM (HRSEM), able to scale down and study specific spatial arrangement and interactions between NPs. (Mourdikoudis et al., 2018), (Tanaka, 2014).

- Scanning Transmission Electron Microscopy (STEM)

STEM is considered as the most promising observation and analysis method in electron microscopy. This technique has a combination of some characteristics of TEM and SEM, for example, it uses electrons transmitted though very thin specimens to imaging (as TEM) and makes imaging by scanning from upper-left to lower-right pixels of a specimen (as SEM). Some advantages of STEM are the ability to detect single atoms in annular dark-field STEM (ADF-STEM), where images are not contrast-reversed with the amount of defocus and give higher resolution than most of lens of TEM (property called as “double resolution”. However, the contrast can impede the visualization of light elements (Mourdikoudis et al., 2018), (Tanaka, 2014).

4.1.5 Properties

The MNPs properties are mainly classified into physical (included optical, electric and magnetic properties), chemical (such as *chemical reactivation* rate), and mechanical (like *strength* and *hardness*). Some magnetic properties are *Curie* (temperature at which MNPSs lose their permanent magnetic properties) and *Néel* (antiferromagnetic material becomes paramagnetic) *temperatures (*T_C and T_N respectively) and *coercivity field* (H_C). As it was mentioned before, most properties are defined according to geometric or structure data (such as size, shape, composition, and crystal structure) and magnetic data (such as *magnetization, saturation magnetization, remanent magnetization, coercivity* and *blocking temperature*) (Sabbas, 2014).

According to Zhang et al. (2018) *Saturation magnetization* (M_S) is "the maximum magnetization value of a material under a high magnetic field" and *coercivity* is "the strength of the external magnetic field to make the magnetization value of subjective materials zero". It is important to mention that magnetic effects are mainly caused by electrons, holes, protons, and positive /negative ions. Thus, a spinning electric-charged particle creates magnetic dipole, so-called magneton. When all magnetons are aligned in the same direction in a critical volume, it is called magnetic domain. So, when the particle radius is large, is categorized as a *multi-domain.* If the size is reduced, it will become *single-domain*, and if the size is still being compressed, it will be *superparamagnetic* (Sabbas, 2014a), (Akbarzadeh et al., 2012), (Issa et al., 2013), (Zhang et al., 2018).

The particle shows a *superparamagnetic* behavior when its grain size is less than 20 nm. These types of particles can be magnetized when a magnetic field is applied, but then,

when the field is turned off, the particles lose their magnetic properties and leave no remanent magnetization. No coercivity is required to bring the magnetization back to zero and this property allows MNPs to maintain structurally stable. It is important to notice that coercivity is smaller when particles are spherical, this because *shape anisotropy* is shorter (it refers to the changing of magnetic particles depending on the analysis direction) (Sabbas, 2014a), (Akbarzadeh et al., 2012), (Issa et al., 2013).

However, superparamagnetic property can be removed if the temperature is below a particular value called blocking temperature (T_B). This value can be reached when the *thermal energy* (E_{th}) exceeds the *anisotropy energy* (E_a), and it can be calculated with the zero-field-cooled (ZFC) measurement. If the sample consists of nearly equal size particles, T_B is determined by the peak of the resulting magnetization versus temperature curve, but if the sample has a high shape anisotropy and a large distribution, the value cannot be accurately determined (Sabbas, 2014a), (Akbarzadeh et al., 2012), (Issa et al., 2013).

On the other hand, for biomedical uses, the application of MNPs with superparamagnetic behavior at room temperature are preferred (this because zero coercivity is needed to leave no residual magnetization), and they must be stable in water at pH 7. MNPs also must be small to avoid precipitation due to gravitational forces. Furthermore, for medical applications, MNPs must be *biocompatible, non-immunogenic* and *non-toxic*. Their size must be in a range of 10-50 nm to preserve colloidal stability, resist MNPs aggregation or agglomeration, improve the efficiency of coating (this would contribute to increase aggregation resistance, biological clearance avoidance and better targeting), and be able to remain in circulation through the capillary systems of organs without provoking vessel

embolism. Also, the MNPs must have a high saturation magnetization to allow the particles movement control with external magnetic field and specify the targeted pathological tissue (Akbarzadeh et al., 2012), (Issa et al., 2013).

4.2 Magnetic ferrite nanoparticles

According to Kharisov et al. (2019), ferrites are "chemical compounds obtained as powder or ceramic bodies with ferrimagnetic properties formed by iron oxides as their main component, Fe_2O_3 and FeO", which can be partly changed by other transition metal oxides. Ferrites can be classified according to their crystalline structure: hexagonal ($MeFe_{12}O_{19}$), garnet ($Me_3Fe_5O_{12}$), and spinel (($MeFe_2O_4$), where Me represents one or more bivalent transition metals (Mn, Fe, Co, Ni Cu, and Zn); or according to magnetic properties: "soft" (low coercivity and easy demagnetization) and "hard" (high coercivity and difficult demagnetization) magnets (Mohallem et al., 2012).

The structure of spinel ferrites has a face-centered cubic unit cell with eight formula units per unit cell ($M_8Fe_{16}O_{32}$), containing then 96 interstices (64 tetrahedral and 32 octahedral) existing between a package of oxygen atoms. However, only 8 tetrahedral (A sites) and 16 octahedral (B sites) positions can be occupied by the metallic ions (Figure 5) (Soufi et al., 2021). Specifically, the interplanar distances between the A-site is 0.58 Å, while for the B-site is 0.73 Å (Taha et al., 2018).

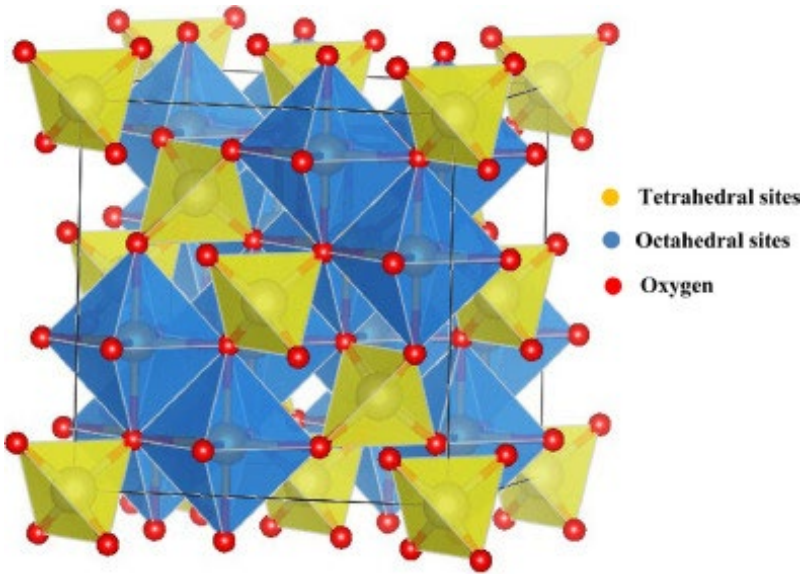

Figure 2. Unit cell structure of spinel ferrite with assigned tetrahedral (A sites) and octahedral (B sites) positions between a package of oxygen atoms (Soufi et al., 2021).

The most attractive compounds between magnetic ferrite nanoparticles (MFNPs) are magnetite (Fe_3O_4) and maghemite (γFe_2O_3), the first being an inverse spinel ferrite and the second a fully oxidize magnetite. However, it also can be found other types of ferrites, such as cobalt, nickel, copper and zinc ferrites (Kharisov et al., 2019).Now, superparamagnetic iron oxides nanoparticles (SPIONs) can be classified according to their overall diameter (including iron oxide core and dehydrated coating, aspect that will be discussed later on this work): oral or *micron*-sized SPIONs (300 nm to 3.5 μm), standard or *small* SPIONs (SSPIONS) (60 to 150 nm), *ultrasmall* SPIONs (USPIONs) (10-50 nm), and *monocrystalline* iron oxide nanoparticles (MION- a subset of USPIONs) (10-30 nm) (Kharisov et al., 2012).

4.2.1 Preparation procedures

The most common methods used in the synthesis of the ferrite colloids, Fe_3O_4 and γFe_2O_3, are physical methods like gas-phase deposition and electron beam lithography. However,

these methods are not able to control the particle size at a nanometer scale. Then, it can be used wet chemical preparation methods, such as sol-gel synthesis, oxidation method, chemical coprecipitation, hydrothermal reactions, flow injection synthesis, electrochemical method, aerosol / vapor-phase method, sonochemical decomposition reactions, supercritical fluid method, and synthesis using nanoreactors (Reddy et al., 2012).

This type of methods is efficient at obtaining crystalline particles with high magnetization, being low-cost and requiring few instruments. However, they are not completely eco-friendly, thus, many variables should be regulated, like pH, addition rate of reagents, deaeration, agitation speed and temperature (Velásquez et al., 2018). Besides, it is also used microbial methods, which are generally simple, versatile, and efficient with appreciable control over the composition and the particle geometry of the resulting material (Reddy et al., 2012).

Specifically for this work, *chemical co-precipitation* will be the most important method to discuss, due to its easiness, efficiency, and reproducibility. Magnetite nanoparticles are commonly prepared with this procedure and giving as a general reaction (3):

$$2FeCl_{3(solution)} + FeCl_{2(solution)} + 8BOH \rightarrow Fe_3O_{4(solid)} + 8BCl \quad (3)$$

Where BOH is a base with B^+ as a viable cation like Na^+ or K^+ (usually NaOH). The composition of the magnetite nanoparticles will depend on the type of anion used in the reaction (can be chloride, sulfate, or nitrate); the ratio of Fe^{+2} to Fe^{+3}, reaction temperature, and pH (Pande & Bhaskarwar, 2016). However, with this method, the magnetite

nanoparticles are not stable at ambient conditions, thus, it is likely that they will agglomerate or/and oxidize (4) to maghemite.

$$Fe_3O_4 + 2H^+ \rightarrow \gamma Fe_2O_3 + Fe^{2+} + H_2O \quad (4)$$

Besides the magnetite oxidation issue, with this method nanoparticle's size and shape can't be controlled, unless different factors are adjusted. These are pH, ionic strength, temperature, nature of the salts (perchlorates, chlorides, sulfates, and nitrates), or the Fe^{II} or Fe^{III} concentration ratio. Also, the main advantage of this method is that large amounts of magnetic nanoparticles can be synthesized (Laurent et al., 2008). In addition, magnetite-coated nanoparticles with biocompatible coatings (such as SiO_2) can be synthesized by a combination of co-precipitation and sol-gel methods (Mohammadi et al., 2021).

According to a study of spinel ferrite MFe_2O_4 (M=Co, Cu, Mn, Ni and Zn) by Xian et al. (2020), in which a comparison was made between the sol-gel, co-precipitation and solvothermal methods effects on persulfate activation for the removal of organics from aqueous solution, it was obtained that sol-gel can provide good-purity, porous structure, large surface area, and favorable element chemicals states for ferrite. $CuFe_2O_4$ was the ferrite with better results, showing better catalytic performance in the removal of organics. In addition, spinel ferrites, $NiFe_2O_4$ and $MnFe_2O_4$, were also studied by Chireh et al. (2020), demonstrating the variation of average nanocrystalline size as a function of calcination temperature in thermal treatment synthesis. It was obtained that, in a range of 420-570ºC (optimum calcination temperatures), both MFNPs size grow directly proportional to the temperature increase.

Something important to mention is that chemical synthesis techniques, such as combustion method, can lead to the formation of foreign nonmagnetic phases (e. g., hematite Fe_2O_3) due to a further thermal treatment. Szczygieł & Winiarska (2014) synthesized Mn-Zn ferrites by the sol-gel autocombustion method, obtaining that the average crystalline size was the smallest for ferrites prepared from a mixture of fuels (citric acid and ethylenediamine tetraacetic acid (EDTA)), which is 40 nm.

4.2.2 Characterization methods

Most of the characterization techniques mentioned before in this work can be used to any MFNPs, with few exceptions, such as *Nuclear magnetic resonance (NMR) spectroscopy,* given that this method is typically used to study diamagnetic and antiferromagnetic NPs and not ferri- or ferromagnetic and superparamagnetic, due to its large saturation magnetization causing variations in a local magnetic field (Mourdikoudis et al., 2018).

Velásquez et al. (2018)in their report of magnetite-maghemite synthesis by high-energy ball milling used as characterization methods XRD, TEM, room temperature Mössbauer spectroscopy, vibrating sample magnetometry, and atomic absorption spectroscopy. XRD was used to distinguish the phases and analyze the structure of the milling products by the diffractometer XPERT-PRO from PANanalyticial and the software Powder X. Besides, TEM Tecnai F20 Super Twin TMP was used to analyze morphology and particle size.

Chireh et al. (2020) used XRD to obtain the average nanocrystalline size (or crystalline mean size) by using the Scherer formula (5):

$$D = 0.89\lambda/\beta cos\theta \tag{5}$$

Where D is the crystallite size, λ is the X-ray wavelength, θ is the diffraction angle, and β is the half width at maximum height (FWHM).

The full width at half maximum (FWHM) was obtained from the XRD patterns. Also, Mössbauer spectrometer was used to determine that $NiFe_2O_4$ nanoparticles at 570ºC showed a ferromagnetic behavior, and $MnFe_2O_4$ show paramagnetic behavior at 420ºC (Chireh et al., 2020). In relation, Rodríguez-Rodríguez et al. (2018) characterized spinel ferrites, $CoFe_2O_4$, $NiFe_2O_4$ and $ZnFe_2O_4$, with XRD, High-resolution transmission electron microscopy in scanning mode (HRTEM-STEM), and UV-Vis spectroscopy.

Once more, the crystalline mean size (d_{XRD}, as denoted in the article) was obtained by the Scherer formula, resulting that $CoFe_2O_4$, $NiFe_2O_4$ and $ZnFe_2O_4$ have a d_{XRD} of 8 nm, 4 nm, and 10 nm respectively. Additionally, UV-Vis was used to demonstrate that the three spinel ferrites accomplished a good visible and ultraviolet light absorption. Finally, with HRTEM-STEM, actual images of MFNPs were obtained, and textural properties and size were analyzed.

In addition, Scherrer equation can also be used to calculate the average crystalline size of Mn-Zn ferrites. Besides, FTIR spectra is commonly utilized to monitoring the reaction progresses and then with thermal analysis (TGA/DTA) the presence of ferrite powder is confirmed (Szczygieł & Winiarska, 2014).

To characterize the magnetic properties magnetization saturation (M_S), retentivity or magnetic remanence (M_r), and coercivity (H_C), it can be used a Magnetic hysteresis curve, which is a graphic of magnetization [emu/g] in function of an external magnetic field H [Oe].

An example of this type of magnetization curve is shown in Figure 2 (Chitra Devi & Singh, 2021).

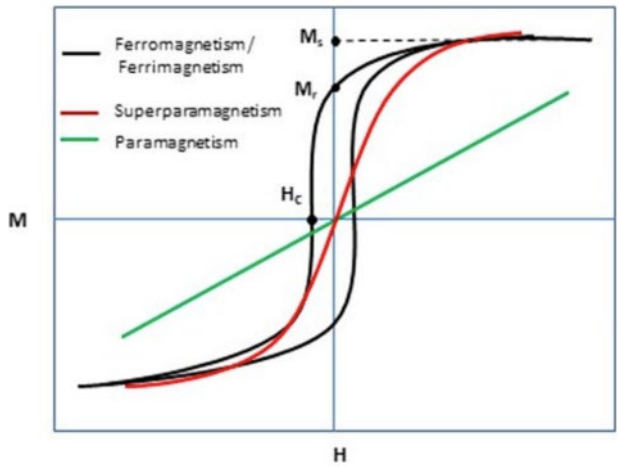

Figure 3. Magnetic hysteresis curve of three different types of magnetic materials. Significant values of coercivity, saturation magnetization and retentivity are showed (Chitra Devi & Singh, 2021).

In the previous figure, ferromagnetic, ferrimagnetic and anti-ferromagnetic materials present a S-shaped magnetization curve with a hysteresis loop, meaning that these types of magnetic materials will require certain amount of reverse magnetic field to return magnetic flux to 0 (high coercivity). However, superparamagnetic materials, as was mentioned before, will not present any value of coercivity, and paramagnetic ones will show reduced saturation magnetization. Nevertheless, these magnetic values will depend on the magnetic material and its properties (Chitra Devi & Singh, 2021). This type of curve was also used to magnetic characterization of spinel-type ferrites, $CoFe_2O_4$, $NiFe_2O_4$ and $ZnFe_2O_4$ in Rodríguez-Rodríguez research (Rodríguez-Rodríguez et al., 2018).

According to Svetlichnyi et al. (2017), TEM, SEM and Brunauer-Emett-Teller methods can be used to analyze magnetite nanostructure. It was observed with TEM that the

composition of the product was divided into a large fraction (>80 nm) and a fine fraction (1-10 nm), given that most of particles were obtained in very dense agglomerates. Besides, to study the particles composition, FTIR spectroscopy, Raman spectroscopy, differential scanning calorimetry, and XRD were applied, and to study magnetic properties, M-H, CF and ZCF curves were realized and analyzed.

4.2.3 Properties

Magnetite and some alloys have irregular particle shape when obtained by grinding bulk materials but can have spherical shape when synthesized by plasma atomization, wet chemistry, or from the gas phases or aerosol. In addition, synthesis technique largely determines the degree of structural defects or impurities in the particle as well as the distribution of such defects within the particle, therefore, determining its magnetic behavior (Akbarzadeh et al., 2012).

Spinel-type ferrites, specifically $CoFe_2O_4$, $NiFe_2O_4$ and $ZnFe_2O_4$, have demonstrated an efficient visible light absorption, good electricity conductivity, high sorption capacity (molecular adsorption-desorption), stability against photocorrosion, thermal stability, moderate magnetic saturation, low magnetic remanence, and low toxicity (Rodríguez-Rodríguez et al., 2018).

According to the results of Rodríguez-Rodríguez et al. (2019) (Figure 3), cobalt ferrites denote a ferrimagnetic behavior, showing a S-shaped curve with slim hysteresis loop. It has a M_S of 64 emu/g, M_r of 29 emu/g, and H_C of 1191 Oe. Nickel ferrites on the other hand, present superparamagnetic behavior, denoting a S-shaped curve but with no coercivity (no hysteresis loop), with M_S of 41.57 emu/g, M_r of 0.01 emu/g. Finally, zinc ferrites show

paramagnetic behavior without reaching saturation magnetization. The superparamagnetic properties could lead to the possibility of reuse these MFNPs, due to its 0 coercivity and almost 0 retentivity, being easily dispersed or magnetized. However, ferri- and ferromagnetic MFNPs cannot be well dispersed due to a high value of magnetic remanence but have the possibility of being highly attracted by a magnet. In the case of paramagnetic materials, they are weekly attracted by a magnet, thus, they cannot be easily magnetized, however, its redispersion is not complicated due to a minimum value of retentivity (Rodríguez-Rodríguez et al., 2019).

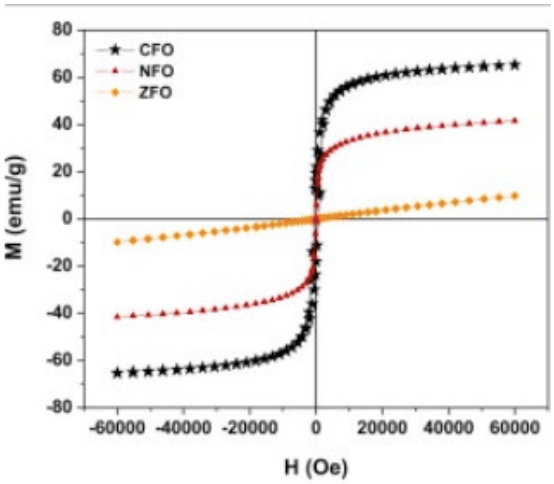

Figure 4. Magnetic hysteresis curve (M-H curve) of cobalt (CFO), nickel (NFO) and zinc (ZFO) ferrites (Rodríguez-Rodríguez et al., 2019).

On the other hand, Singh Yadav et al. (2020) synthesized $MnFe_2O_4$ nanoparticles by sonochemical technique at different sonication time. The average crystalline size and the saturation magnetization increase directly proportional to the sonication time. At 20 min, Mn ferrites presented spherical nanoparticles of 2-5 nm and M_S of 1.9 emu/g, and at 80 min, its spherical NPs to 50-80 nm as agglomerates of smaller NPs of 5-10 nm with M_S of 52.5 emu/g.

The previous information is used to demonstrate that several conditions of preparation affect to the resulting product, giving the possibility to design, in this case, manganese ferrites with desirable properties for a specific application (Singh Yadav et al., 2020).

However, most of spinel ferrites show ferrimagnetic and semiconductor properties, with general characteristics, such as high Curie temperature, large magneto crystalline anisotropy, good thermal stability, tunable size and shape, high specific surface area, high chemical stability, excellent magnetic properties, electrical resistivity, good catalytic activity, mechanical hardness, no filtration, high coercivity, no toxicity and the possibility of being modified or functionalized (Soufi et al., 2021).

4.3 Magnetic core-shell nanostructures – An Overview

According to Nomoev et al. (2015), core-shell type nanoparticles are "a type of biphasic materials which have an inner core structure, and an outer shell made of different components". One of the major issues of MNPs application, is that they tend to agglomerate, thus it is necessary to modify its surface with biocompatible coatings (Sabbas, 2014), (Mohammadi et al., 2021). Some of most widely used components for coating are carboxylates, phosphates, sulfates, silica, gold, dextran, polysaccharides, polyvinyl butyral, poly (methyl methacrylate), polyesters, chitosan, polyethylene glycol, and polyvinyl alcohol (Sabbas, 2014a). In this work, materials used for shells will be classified according to its magnetic properties into diamagnetic shell and magnetic shell.

Core-shell MNPs have been designed to enhance specific properties according to its applications, for example, for biomedical applications, organic shell can be used to improve core's reactivity, and thermal and oxidative stability (Nomoev et al., 2015). However, it can

be added new properties to the nanostructure, such as stability, biocompatibility and biodegradability (Sabbas, 2014b). Most of core-shell nanostructures are prepared in two simple steps: core synthesis and the coating of the core with the shell material (Nomoev et al., 2015). Core synthesis correspond to techniques that were described before in this work.

Also, core-shell nanoparticles can be classified according to their arrangement and number of core and shell layers (Figure 4). Single core-shell are referred to a single core surrounded by a single shell, both of different materials. Reverse core-shell consist of a structure with typical core material (in single core-shell) as coating, and typical shell material as core. Multi core-shell contain multiple cores with a single shell, inversely, multishell-core are structures with multiple shells and a single core. Multicore-multishell NPs have many materials as coating and cores. Finally, yolk-shell displayed a configuration of shell-void-core, having unique properties such as movable cores and interstitial hollow spaces (Singh & Bhateria, 2021).

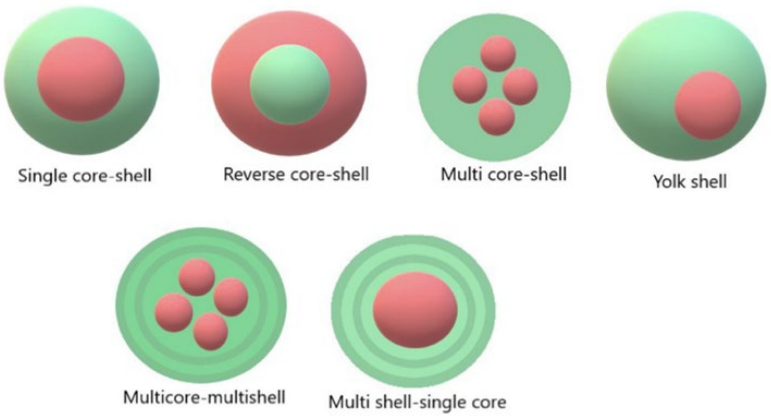

Figure 5. Classification of core-shell nanostructures based on arrangement and core and shell layers (Singh & Bhateria, 2021).

4.3.1 Core-shell nanostructures with magnetic core and diamagnetic shell

Remembering diamagnetism concept, Marghussian (2015) define it as “a very weak form of magnetism that is induced by a change in the orbital motion of electrons due to an applied magnetic field”. Its magnetic moment has a very small magnitude and opposite direction to the magnetic field; thus, it can be said that diamagnetic materials repeal magnetic fields. To function as MNPs coatings, most common diamagnetic materials are organic polymers (such as dextran, oleic acid, carbohydrates chains, among others), and ceramic materials (such as silicon dioxide or silica [SiO_2], hydroxyapatite [$Ca_5(PO_4)_3OH$], and other porous ceramic matrices) (Arteaga-Cardona et al., 2017). In general view, diamagnetic shells enhance MNPs biocompatibility, create molecular linkages, and protect them from oxidation (Chiozzi & Rossi, 2020).

One of the common forms of magnetic core-shell NPs with magnetic core and diamagnetic shell is magnetic/organic core-shell nanoparticles. The need of using organic shells exists because NPs are usually conformed by agglomerations of micrometers, and they must be controlled under a high applied magnetic field to biomedical applications *in vivo (Ghosh Chaudhuri & Paria, 2012)*.

Hydrophilic polymers and polysaccharides are commonly used for organic shells, however, some specific organic materials used to MNPs coating are polyethylene glycol, proteins like dextran and albumin, gelatin, curcumin, dopamine, siloxane, phosphonate, polyaniline, *N*-halamine, polyvinylpyrrolidone (PVP), polyethyleneimine (PEI), and poly (acrylic acid). Besides, diamagnetic shells can be a mixture of any exposed materials, for example, magnetite nanoparticles coated with dopamine, siloxane, phosphonate and other

carboxyl groups can be applied as targeted carriers for drug and other biomolecules delivery, in hyperthermia, and as highly efficient MRI contrast agents (Ghosh Chaudhuri & Paria, 2012), (Chiozzi & Rossi, 2020).

4.3.2 Chitosan

Chitosan is a non-toxic, biodegradable, fiber-like polymer of high molecular weight derived from chitin (a semi-crystalline homopolymer of $\beta - (1 \rightarrow 4)$-linked N-acetyl-D-glucosamine). Having a positive charge gives chitosan the ability to bind with negatively charged fats, lipids, cholesterol, metal ions, proteins, and macromolecules. Although it shows helpful properties, it is not soluble in water, thus chemical modifications of chitosan can be applied to improve solubility in water while maintaining interest characteristics, such as mucoadhesivity, biocompatibility, and biodegradability. Some derivates of chitosan are trimethyl chitosan, carboxymethyl chitosan, sulfated chitosan, thiolated chitosan, acyl chitosan, and grafted chitosan. Each one of them present novel properties and can be useful for different application (Tiwari, 2010).

Assa et al. (2017) presented a review article about some general properties and considerations that make chitosan a very good option to DDS. They mentioned that chitosan is low-cost, biocompatible, non-toxic, and chemically and thermally stable. Compared to its bulk form, it has outstanding physico-chemical, antimicrobial, and biological properties, making it a superior environmentally friendly material with no harm to humans. Its usage is desirable in the creation of DDS due to its ability to control the release of active agents and avoid the use of hazardous organic solvents, and its mucoadhesive character, biodegradability, pH sensitiveness, and solubility in most dilute acids.

Chitosan properties usually depend on its molecular weight and degree of deacetylation. Regarding MNPs coated with CS, the biopolymer provides protection to magnetic core from oxidation, preventing the loss of magnetism and dispersibility. Besides, it provides MNPs lower toxicity, a variety of functional groups to bind drug molecules, reduced aggregation, increased stability, and an extended storage life (Assa et al., 2017).

4.3.3 Structure influence in properties

As reviewed before, core-shell nanostructures can contain as much as substances required to enhance the desirable properties of MNPs to a specific application. Besides, features can be modified by changing the compositing materials or the core to shell ratio. The most optimal properties of core-shell MNPs for biomedical applications are stability, versatility, low toxicity, biocompatibility and biodegradability (Nuzhina et al., 2019). For example, chitosan (CS), which is a natural polysaccharide, possesses beneficial properties such as antibacterial activity, non-toxicity, biodegradability, and biocompatibility, making it an optimal choice for coating. Most of those properties will be mainly determined by the final size of particles (including shell and core), the material used as coating, the magnetic responsive component, and the stability at neutral pH (7) (Smit & Lutz, 2020).

According to Tai et al., the addition of PEG increases the control of MNPs size, therefore stability is better. They obtained that uncoated MNPs, and PEG (0.6 g, 0.8 g, 1.0 g, 2.0 g, and 3,0 g) coated MNPs had sizes of 13.60 nm, 12.30 nm, 11.90 nm, 10.70 nm, 10.40 nm, and 9.30 nm, respectively, meaning that size get lower as more concentration of PEG is added. Also, in this case, sample of 1.0 g of PEG coated MNPs showed high colloidal stability with high electrophoretic mobility (Tai et al., 2016). In addition, Markhulia et al.

(2017) confirm that PEG provides high stability and high dispersion. Besides, PEG coated Fe_3O_4 possess good bactericidal effects against *Staphylococcus epiderminis* cultures (Markhulia, 2017).

Magnetic properties are also dependents of core-shell nanostructures. For example, it was mentioned before in this work that superparamagnetic behavior strongly depends on MNPs size (Akbarzadeh et al., 2012). In addition, M_S and H_C have also a strong dependence on particle size, given that M_S decrease its value as the size arise it and H_C increase it when its size is higher (inverse correlation with superparamagnetic behavior and direct correlation with M_r) (Klomp et al., 2020).

4.3.4 Influence of core-shell behavior in magnetic properties

In summary, for structures where the shell is diamagnetic and the core is magnetic, M_S is usually reduced as shell's concentration and temperature increase, and they usually display superparamagnetic behavior with very few or 0 H_C and M_r (Tai et al., 2016), (Predescu et al., 2018), (Imran et al., 2018), (Mondal et al., 2017).

Commonly used diamagnetic materials are organic polymers (such as polysaccharides and hydrophilic polymers) and ceramic materials. Due to their diamagnetic behavior, all of them reduce the magnetic saturation of the core/shell system in comparison with uncoated core M_S. Besides, for structures with more than one diamagnetic shell (multi-shell single core) the M_S will be reduced even more. Also, diamagnetic shell could influence on magnetic core material, being possible to change it. For example, Fe_3O_4 NPs can be partially transformed to a α-Fe_2O_3 by applying a very thin surface coating of PEG (Ghosh

Chaudhuri & Paria, 2012), (Tai et al., 2016), (Predescu et al., 2018), (Imran et al., 2018), (Mondal et al., 2017).

Crystallinity is defined by Asefa and Dubovoy (2016) as "the degree of long-range structural order comprising a crystal lattice within a (solid) material" (Asefa & Dubovoy, 2016). As was reported before, ferrites can be hexagonal, garnet or spinel according to their crystalline structure. Most of the ferrites that were studied are spinel with a general chemical formula MFe_2O_4, and they usually perform ferromagnetic behavior with excellent magnetic properties, such as high Curie temperature, high coercivity, high remanence and high magnetic saturation. But in case of other spinel ferrites such as nickel ones, superparamagnetic behavior with no coercivity, no remanence and moderate magnetic saturation is displayed (Rodríguez-Rodríguez et al., 2018), (Rodríguez-Rodríguez et al., 2019), (Soufi et al., 2021).

Ferrites can be coated with several materials, such as metal oxides, metals, alloys, polymers and inorganic carbon forms, resulting in core/shell structures with varied and tunable properties. Even though magnetic saturation, blocking temperature, and permanent magnetization mainly depend on particle size, coercivity have a particular relation with shape and surface anisotropy effects (Kurian & Thankachan, 2021). Additionally, Arteaga-Cardona et al. (2017) demonstrated that preparation methods of core-shell structures can influence in magnetic properties .

4.4 Specific applications

4.4.1 Magnetic Hyperthermia

According to Brennan et al. (2020), standard hyperthermia is "a medical treatment that involves raising the temperature of the body in an attempt to treat diseases such as cancer". However, they also mention that this method, which is usually applied by using infrared light, microwaves or radiofrequency, have some negative effects to non-targeted tissues, leading to blood clots and more serious cardiovascular issues. Usually, the temperature that must be reached to achieve cell death is around 40-43ºC, thus, this technique is rarely used as a first choice because of the non-selective heating that may affect non-targeted areas (Brennan et al., 2020). It is important to mention that some other reports stablish that cell death by apoptosis occurs between 41-46ºC, however, if temperature is above 46ºC necrosis will be induced (Kesse et al., 2020).

Magnetic hyperthermia has the same basis as the standard one, with the difference that it is focused on a specific region and the increase of temperature is induced by MNPs. These have the possibility of selectively kill the malignant agent by the action of an external magnetic field and loss mechanisms, such as Brownian (heat provoked by friction emerging from particle oscillations), and Néel (heat due to rotation of the magnetic moment) effects. The main factors to be considered are MNPs heating capacity, specific absorption rate (SAR), and the modification type in MNPs surface (Sabbas, 2014b).

The heating capacity of MNPs allows to control generated temperature when MNPs are in the body and a magnetic field is applied. As was mentioned before, the temperature must be between a specific range without exceeding, according to this last resource, 45ºC.

Usually, researchers seek to synthesize MNPs with T_C around 40ºC-45ºC to achieve better control of temperature. On the other hand, SAR "measures the efficiency of the heating power of a magnetic material and is described by the amount of energy converted into heat per unit of time and mass" (extract by Sabbas, 2014) SAR mainly depends on magnetic saturation, the strength of magnetic field (H) and its frequency (f). One of the major goals is to enhance the heating efficiency and simultaneously reduce the amount of material that must be injected (Sabbas, 2014).

Other properties that must be considered are composition, size and shape of the NPs and the specific loss power (SLP) (Martinez-Boubeta et al., 2021). Osaci & Cacciola (2017) defined SLP as "the electromagnetic power lost per nanofluid mass unit, and it is expressed in watt per kilogram". They also state that there are 3 different mechanisms for heat generation through magnetic hyperthermia: susceptibility loss, hysteresis loss, and viscous heating (magnetic stirring loss).

Susceptibility loss occurs in superparamagnetic NPs, and hysteresis loss takes place when sedimentation and agglomeration increase because of a transition of small NPs to stable single-domain FM NPs. However, as was reviewed before, by increasing NPs size, agglomeration and sedimentation will induce the clogging of blood vessels, making these structures undesirable for clinical applications. Magnetic stirring loss occurs when large particles are not aligned to the applied field axis and viscous heating is produced when stirring (Osaci & Cacciola, 2017).

SAR can be calculated by the equation (6):

$$SAR = \frac{c}{m} x \frac{dT}{dt} \tag{6}$$

Where *c* is the specific heat capacity of the medium, *m* is the mass of the sample, and *dT/dt* is the initial slope of the variation of temperature with time curves. SAR is directly correlated with heating efficiency and magnetic saturation (Hammad et al., 2016).

According to Barrera et al. (2018), who synthesized core-shell Fe-oxide@SiO_2 NPs, state that to effectively function for magnetic hyperthermia, NPs should be nearly superparamagnetic, enough for preventing agglomeration and keeping their sizes small, without eliminating hysteresis losses to ensure heat generation. They compared two different samples, according if NPs were measured from static or dynamic room temperature loops. They obtained that with static loops, coercivity was extremely negligible, resulting in low values of SAR, while with dynamic loops, both coercivity and SAR values were higher.

Regarding Brownian and Néel mechanisms, Fabris et al. (2020) proposed definitions and equations for both. Brown mechanism is "the physical rotation of the MNPs characterized by the time relaxation τ_B". Brown relaxation time is given by (7):

$$\tau_B = \frac{3\eta V_{hyd}}{k_B T} \tag{7}$$

Where η is the viscosity of the medium, V_{hyd} the hydrodynamic volume of MNPs, and $k_B T$ the thermal energy. On the other hand, Néel mechanism "involves the inversion of magnetic moment within the crystal lattice". Néel relaxation time is defined by (8):

$$\tau_N = \tau_0 \exp\left(\frac{K_{eff} V_{mag}}{k_B T}\right) \tag{8}$$

Where K_{eff} is the effective anisotropy, V_{mag} the magnetic volume of the single-domain NPs, and τ_0 is the attempt relaxation time of the system (typically between 10^{-9} and 10^{-11} s).

The dominating relaxation process is always the one with the shorter relaxation time. Then, Brown relaxation rules for systems with large magnetic anisotropy and/or low viscosity, and Néel relaxation for systems with low magnetic anisotropy and/or high viscosity. They also state that it is important to "tune individual parameters that control the magnetic relaxation mechanisms in order to optimize the SLP in a medium that stimulates the viscosity of the cellular environment". So, one of these parameters than can be enhanced with soft-hard core-shell NPs is magnetic anisotropy, providing the chance of reaching the optimum heating condition for lower NPs size (Fabris et al., 2020).

On the other hand, Simeonidis et al. (2020) proposed several correlations between some individual parameters and desirable magnetic hyperthermia properties. First, ferrites NPs with small dimensions are optimal to minimize the dosage required for an effective treatment, however, Brown mechanisms for heating are nearly disabled during particles immobilization in biological environments, provoking a reduction in heating efficiency. It is important to recall that magnetic heating is primarily dependent of the magnetic anisotropy energy, the experimental heat conditions, and the dosage (Simeonidis et al., 2020).

4.4.2 Drug transport and controlled delivery

MNPs have the possibility of creating drug delivery systems (DDS) by being capable of reaching a targeted area under guidance of an external magnetic field. As the previously mentioned biomedical applications, MNPs must be coated to possess optimal properties such as biocompatibility, non-toxicity, and non-immunogenicity. Besides, core-shell MNPs as drug nanocarriers, must be able to avoid their recognition by the mononuclear phagocytic system (Popescu, 2011).

Drug delivery systems (DDS) must have certain functions and criteria. They must be optimized to reduce the amount of systematic distribution of the cytotoxic drug (decreasing associated and undesirable side effects), and to reduce the dosage required. Also, DDS must be able to avoid cell capture by reticule-endothelial system (RES); have low toxicity with few or no side effects and easy-elimination after function; transport and target accurately the drug to the site in high yield; and release effective quantities of drugs to achieve desirable concentrations(Xiong et al., 2018).

It is important to mention that each targeted area of the human body will have different complications and additional requirements when MNPs are being used as drug nanocarriers. Some of these will be discussed in this last biomedical application section, encompassing several diseases and organs such as neurological disorders (brain-targeting), lung cancer, cerebral malaria, breast cancer, prostate cancer, among others (Mathews et al., 2023).

4.5 Electrospinning process

Chitosan nanofibers can be produced through electrospinning, a technique that has proven extremely useful for preparing nanofibers for tissue engineering due to its ability to process a wide range of polymers, yielding fibers with diameters between 20 and 400 nm. Briefly, applying a sufficiently high voltage between a needle and a metallic collector overcomes the surface tension holding a droplet of liquid at the needle tip, resulting in a very thin jet of fluid projected toward the collector. During the trajectory between the needle and collector, the solvent evaporates, forming a nonwoven structure (Barbosa et al., 2011).

The applied electric field in electrospinning is influenced by various parameters, including flow rate, the distance from the tip to the collector, properties of the polymeric precursor (such as concentration, molecular weight, viscosity, surface tension, and solvent type), and environmental conditions (like humidity and temperature). Different jet configurations can emerge from the nozzle tip. As the voltage applied to the nozzle increases, the electrospinning process transitions through different modes: dripping mode, cone jet mode, and oscillating jet mode (Ahmadi et al. 2024).

In **dripping mode**, spherical or spindle-like droplets form and elongate in the direction of the electric field. The frequency of these droplets increases with voltage until a transition occurs from dripping to a stable jet, balancing electric forces with surface tension and gravity. This leads to **cone jet mode**, where the liquid forms a conical shape known as the Taylor Cone. In this mode, a steady jet emerges that is axially symmetric but can lose this symmetry under higher potentials, resulting in **oscillating jet mode** due to non-axisymmetric instabilities. At even higher voltages, the jet can split into multiple jets in **multi-jet mode**, increasing the number of micro jets produced (Vicente et al., 2021).

5. Methodology

5.1 Synthesis of magnetic nanoparticles

Initially, 50 mL of solution of each precursor nitrate were prepared and stirred for 30 min at 40°C (increase temperature to 80°C during this reaction time). Subsequently, a solution of 5 M NaOH was added until obtaining pH 12 (approx. 10 mL), while the reaction was stirred at 80°C for 1 h, taking care not to evaporate all the water in the medium to avoid the formation

of a gel. Additionally, 6 washes with DI and 4 washes with reactive ethanol by centrifugation (at 5500 rpm for 15 min) were performed, decanting magnetically between each wash.

Besides, the synthesized ferrites are dried at 80°C for a whole night, and then crushed with mortar and pistil and recovered using an acetate film, it is important to avoid scratching the mortar, and / or the corresponding recipient, to avoid contaminating the sample with Si compound. It is then calcined at 1000°C for 2 hours. Again, the ferrites are crushed and prepared for further characterization. A schematic representation of the synthesis process is showed in Figure 6. This method is adapted of techniques from Zou et al (2018) and Zou et al. (2018), and the corresponding calculus is presented in Annex 1.

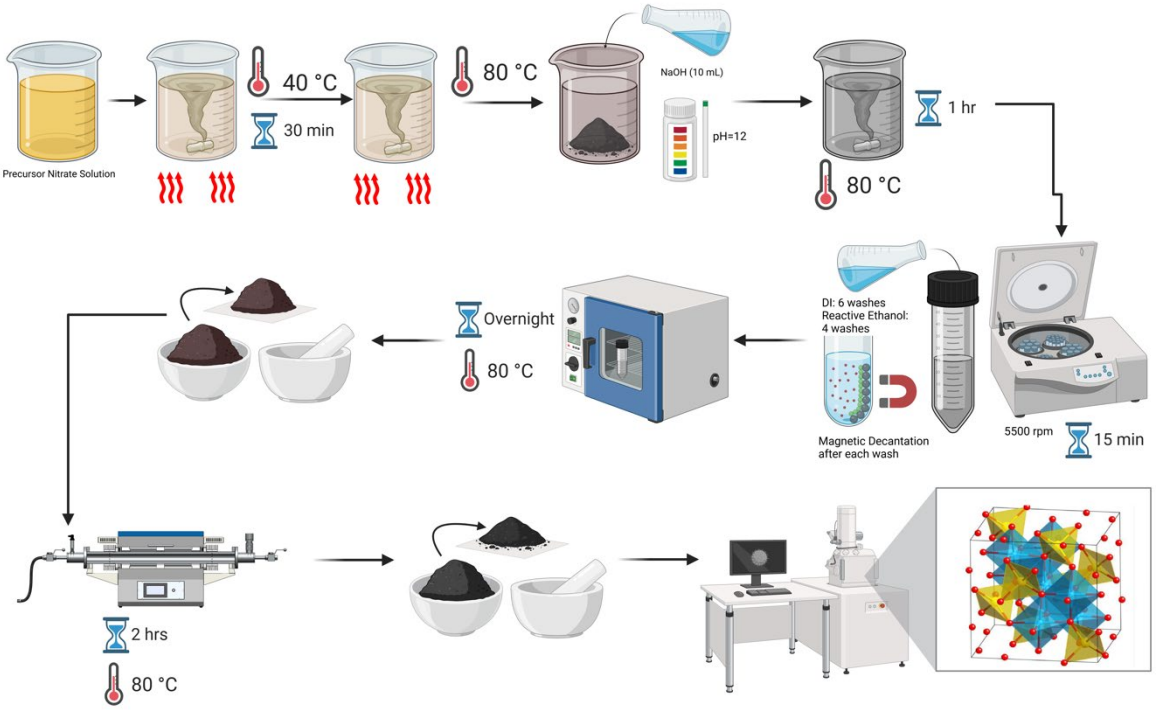

Figure 6. Schematic representation of $Ni_{1-x}Zn_xFe_2O_4$ ferrite nanoparticles synthesis by co-precipitation method (made with BioRender)

5.2 Carboxymethylation of chitosan

Pure chitosan (0.140 g) was dispersed in 5.5 mL of isopropanol. After 20 minutes of magnetic stirring at room temperature, 0.4 g of NaOH (in 1 mL DI) and a solution of monochloroacetic acid/isopropanol solution (0.161 g monochloroacetic acid in 1.69 mL DI with 0.1 mL isopropanol) were added to the suspension. The reaction was magnetically stirred for 3 h at room temperature and the solid product was then filtered, suspended in 10 mL of methanol and neutralized with glacial acetic acid using a potentiometer. The product was extensively washed with 80% ethanol and dried at room temperature using vacuum. This method is adapted from Abreu & Campana-Filho (2005). In Figure 7, a schematic representation of the carboxymethylation is proposed.

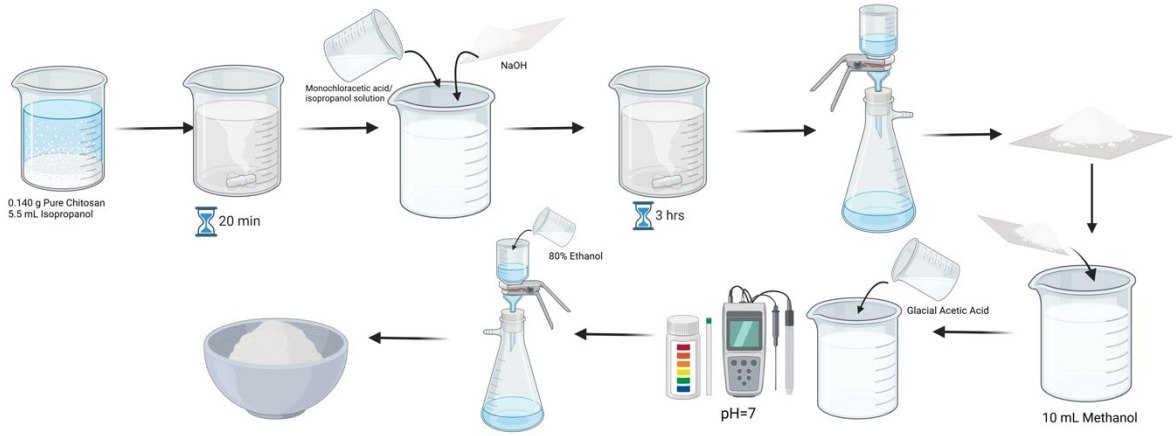

Figure 7. Schematic representation of carboxymethylation process of chitosan (made with BioRender)

5.3 Synthesis of PVA, Ch-PVA and CMC-PVA nanofibers

The chitosan/PVA nanofibers were fabricated via the electrospinning method using different concentrations and method conditions. The equipment consists of a static aluminum disk

collector connected to a power supply of a maximum of 30 kV (however, at higher values of 20 kV, the electromagnetic field causes the formation of an electric arc) and a pump for the solution injection. Firstly, 10 wt. % PVA and 12 wt. % solutions (dissolved in water) were prepared and qualitatively characterized by observation, SEM and EDX.

Secondly, the formation of carboxymethyl chitosan conjugated with PVA nanofibers was attempted by preparing a mixture of solutions with concentrations of CMC (1.5-5 wt. %) and PVA 10 wt. % (prepared in water) with volume ratios of 4:1 and 3:1 %(v/v) (CMC:PVA). The utilized solvent for dissolving the CMC was initially water and compared afterwards with a mixture of acetic acid and water 50/50 %(v/v).

The preparation procedure was made by using different concentrations (CMC: 1.5-5 wt. %, and PVA: 10-12 wt. %). The feeding rate was tested between 0.15-0.5 mL/h, while the applied voltage was between 16-21 kV. Temperatures and humidity were in the range of (24-30°C) and (30-40%), respectively, while the distance of the needle to the collector was ranged between 10-20 cm.

Additionally, trials of chitosan/PVA nanofibers were performed, with volume ratios of 3:1 and 1:3 v/v (Ch:PVA). In this case, both polymers were dissolved in a mixture of acetic acid/water 70/30 %(v/v), and the conditions of electrospinning (feeding rate, voltage, temperatures, humidity, and distance to collector) were maintained in the same interval as the tests with CMC/PVA composition.

To prepare all samples, the following procedure was followed: PVA solution was prepared by adding the corresponding weight of hydrolyzed PVA and solvent (water for CMC sample, and acetic acid/water 70:30 %(v/v) for chitosan) and magnetically stirred for

1 h at 80°C for 1 h, and then was completely dissolved by leaving the solution stirring overnight at room temperature.

The Ch and CMC solutions were prepared by dissolving the corresponding amount of compound and solvent (water or acetic 70:30 %(v/v) acid/water mixture) and were further magnetically stirred overnight at room temperature. To achieve a homogeneous solution between PVA and Ch/CMC, both compounds were mixed for 3 h at room temperature just before performing the electrospinning process. The preparation and electrospinning processes are schematized in Figure 8.

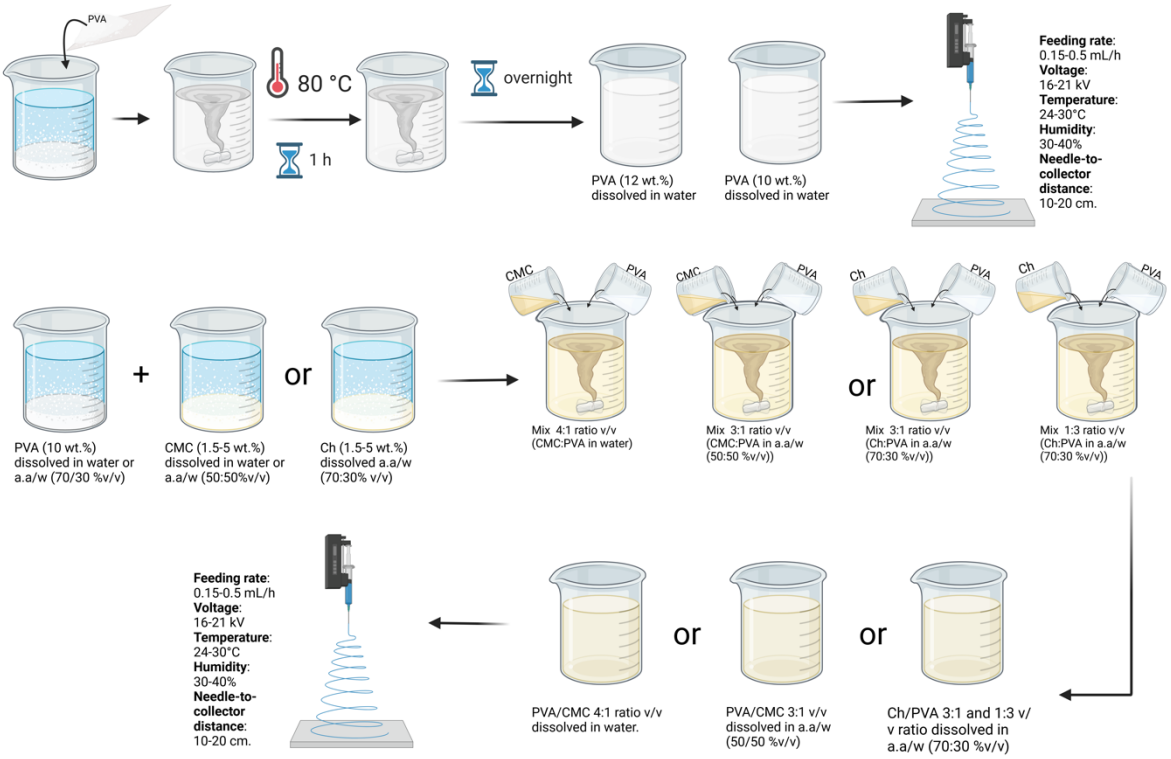

Figure 8. Schematic representation of preparation of PVA, CMC/PVA, and Ch/PVA solutions and the electrospinning process (made with BioRender)

5.4 Synthesis of Ch-PVA-MNPs nanofibers

In order to include the magnetic nanoparticles in the nanofibers, the corresponding magnetic nanoparticles at 10 and 20 wt.% per polymer weight were added to the solution of Ch/PVA and stirred at room temperature overnight for assuring complete homogeneity. To achieve this, magnetic nanoparticles were treated with a solution of HCl 10%; specifically, the magnetic nanoparticles were dissolved in the acidic solution and sonicated for 5 min. Subsequently, the solution was left interacting for 30 min without stirring.

Afterwards, a 3-step washing process was performed by magnetic decantation using distilled water. From the second and third addition of water, the resulted supernatants were later analyzed by DLS to determine the change in terms of size dispersion and stability. Then, the sample was washed with absolute ethanol one time and dried at 80°C overnight. The process is schematically presented in Figure 9.

5.5 Synthesis of core-shell nanofibers

As a preliminary attempt to obtain smooth and homogeneous core-shell nanofibers of PVA/Ch/MNPs as core and PCL as polymeric shell, PCL and PVA/Ch@PCL core-shell nanofibers were synthesized. For preparing PCL nanofibers, a 5 wt. % solution was prepared using DCM:DMF (80:20 %v/v) as solvent. The electrospinning process was performed with the static collector and with a special nozzle for coaxial electrospinning with 26 Gauge of diameter.

The feeding rate for the PCL nanofibers was tested between 1-1.5 mL/h, while the voltage was around 11.5-16 kV. The distance of tip-to-collector was varied between 10-15 cm, and

the temperature and humidity percentage were kept in ranges of 26-27°C and 25-26%, respectively.

On the other hand, for the core-shell nanofibers, the feeding rate of both core and shell were kept around 0.5-0.75 mL/h during electrospinning, and the voltage was around 18-21 kV. The distance tip-to-collector was varied between 10 and 15 cm, while the temperature and the humidity were maintained around 26-27°C and 25-26%, respectively.

5.6 Physicochemical characterization

Calcined Ni-Zn ferrite nanoparticles were analyzed in terms of size, crystallinity and lattice arrangement by XRD using a PanAlytical Empyrean with an X-ray radiation of Cu and Co with a wavelength value of 1.54184 Å and 1.78901 Å, respectively. Additionally, these physicochemical characteristics were complemented by the obtention of micrographs by SEM and patterns of EDX using a MAIA3 TESCAN.

Furthermore, functional groups and molecular vibrations were analyzed by FTIR and Raman characterizations, using an Agilent Cary 630, and a XploRA MicroRaman Spectrometer, respectively. To evaluate the size dispersion of the synthesized nanoparticles, DLS analysis was performed with a Nanotrac Wave II (Microtrac). The same analytical studies were made for the ferrite nanoparticles treated with acidic solution, except for Raman.

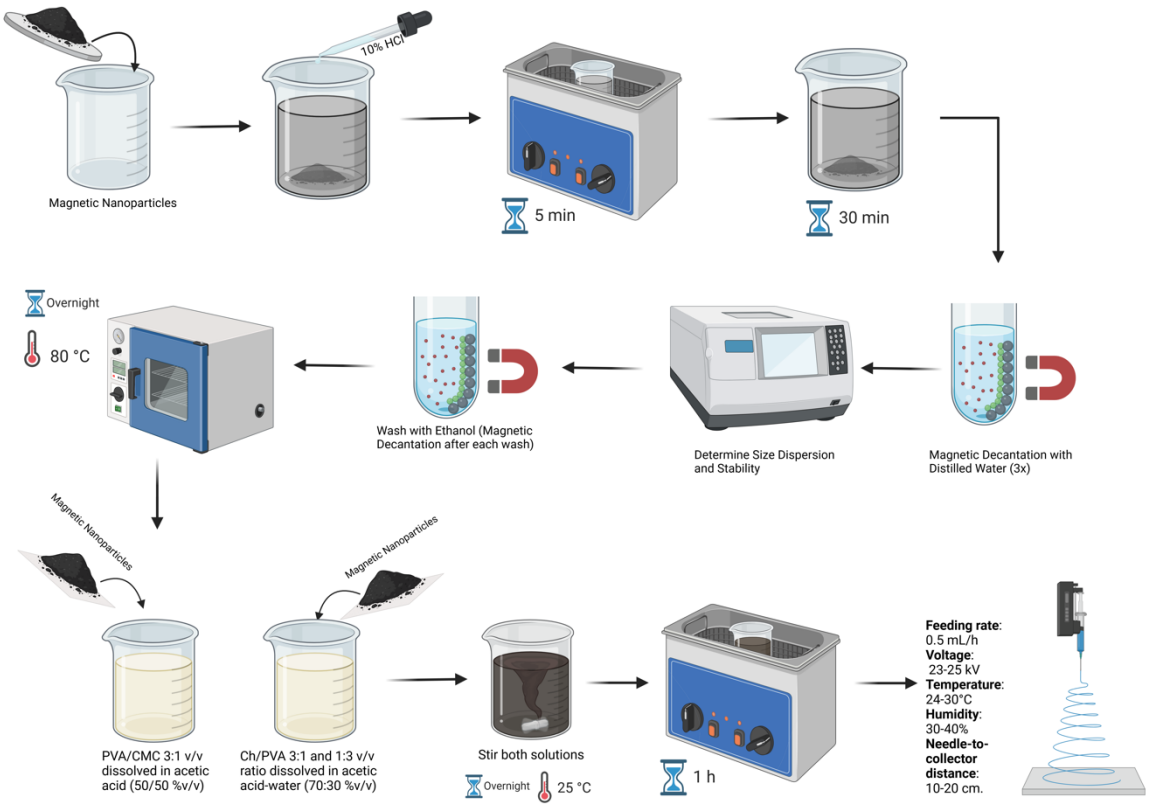

Figure 9. Schematic representation of acidic stabilization of magnetic nanoparticles and their incorporation to the polymer solution for electrospinning process (made with BioRender).

5.7 Magnetic hyperthermia study

To analyze the magnetic behavior of the samples, a magneTherm from nanoTherics was used, which consists of a Laboratory Power Supply with a voltage range of 110V/220V: 50/60V, an oscilloscope with a voltage range of 100-240/100-120V, a function generator with voltage of 115/230V: 50/60Hz, and the magnetherm with a voltage of 115/230 V: 50/60 Hz. A capacitor array C22 was selected, with a total of 17 coil turns, and using as setting a fixed

oscilloscope voltage of 20 mV, nominal frequency of 329.9 KHz, a DC power supply voltage of 30.4 V, a DC power supply current of 8.4 A, and an electrical conductivity of 10 μS.

By knowing the length of the solenoid wire (l), the applied current (I), the number of coil turns (N), and the vacuum permeability ($\mu_0 = 4\pi\ x\ 10^{-7} Tm/A$) it is possible to calculate the applied magnetic field (flux density, B) with the equation (9) (Salunkhe et al., 2016):

$$B = \frac{\mu_0 NI}{l} \tag{9}$$

Considering that the current is 8.4 A, the length is 10 cm, and the number of coils is 17, it can be estimated that the magnetic flux density is equal 17.94 mT. The magnetic tests were made to all samples at different concentrations: 4, 8, 16 and 32 mg/mL, for 300 seconds each measurement.

6. Results and discussion

6.1 Physicochemical characterization of Ni1-xFe2O4 ferrite nanoparticles

In Figure 10, the XRD patterns for $Ni_{1-x}Zn_xFe_2O_4$ ferrite nanoparticles at different zinc ratios (x=0, 0.25, 0.5, 0.75 and 1.0) are presented. As expected, characteristic peaks of ferrite nanoparticles can be seen, referring to the planes *h,k,l* (111), (220), (311), (400), (422), (511), (333), (440), and (533), at 19°, 30°, 35.5°, 43°, 54.5°, 57°, 57°, 62°, and 74°, respectively. However, between samples with different zinc concentrations, specific peaks are absent and vary, which means the formation of different impurities with changes in their structures (Hwang et al., 2020).

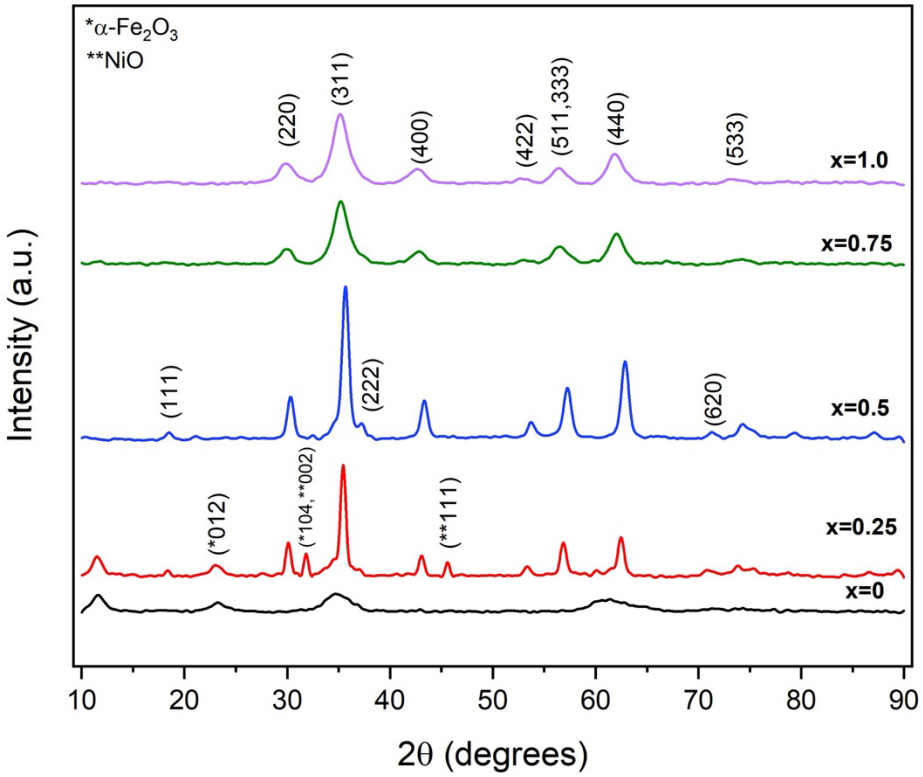

Figure 10. XRD diffractograms of $Ni_{1-x}Zn_xFe_2O_4$ with x=0, 0.25, 0.5, and 0.75 with their characteristic planes assigned, including the possible content of hematite (α-Fe_2O_3) and nickel oxides.

When x=1.0, 0.75 and 0, (001) plane is not located in the diffractogram, while with x=0.5 and 0.25, the peak was presented with diminished intensity. Specifically, in the sample with x=0, the planes (533), (220), (400), (422), and (511) are not distinguished, which could signify that this sample is more likely to be amorphous. Nevertheless, this sample agree in its highest peak with the other proportions, being in this case the (311) plane.

To analyze the differences between samples in terms of their crystalline structure, the peak positions of the relevant peaks are presented in Table 2. Additionally, interplanar spacing *d* of all planes are calculated (Table 3) from the X-ray diffraction patterns by using the Bragg's law (10):

$$2dsin\theta = n\lambda \quad (10)$$

Where λ is the wavelength of X-ray radiation, which in this case corresponds to 1.54184 Å (Cu-Kα). Furthermore, the lattice parameter a has been calculated from the highest peak, corresponding to (311) plane in all samples, using the equation $a = \sqrt{h^2 + k^2 + l^2}$ (11). The calculated interplanar distances and lattice parameters are in accordance with the reported values in literature (Hwang et al., 2020).

As can be seen, the lattice parameter value tends to increase with Zn^{2+} content (with exception of x=0.5), which can be due to the difference between the ionic radius of Ni (0.78 Å) and Zn (0.83Å). Remembering that distances between A-sites and B-sites are 0.58 Å and 0.73 Å, respectively, the lattice parameter is increased by having larger ionic radius than Fe^{3+} (Taha et al., 2018). The previous explanation can be also the reason of the slight shift in the (311) peak position, which decreases with the addition of Ni^{2+} content.

Table 2. Peak position of characteristic peaks of $Ni_{1-x}Zn_xFe_2O_4$ ferrite samples with x=0, x=0.25, x=0.5, x=0.75, and x=1.0.

x	**Peak position: 2θ(°)**					
	(2 2 0)	**(3 1 1)**	**(4 0 0)**	**(4 2 2)**	**(5 1 1)**	**(4 4 0)**
0	-	34.94	-	-	-	-
0.25	30.07	35.46	43.01	53.43	56.90	62.42
0.5	30.34	35.66	43.33	53.72	57.26	62.86
0.75	29.97	35.25	42.89	52.92	56.58	62.13
1	29.90	35.19	42.62	52.50	56.42	62.07

Table 3. Interplanar distances of characteristic peaks of $Ni_{1-x}Zn_xFe_2O_4$ ferrite samples with x=0, x=0.25, x=0.5, x=0.75, and x=1.0, and lattice parameter considering the (311) plane.

x	Interplanar distances (Å)						Lattice parameter (Å)
	(2 2 0)	(3 1 1)	(4 0 0)	(4 2 2)	(5 1 1)	(4 4 0)	
0	-	2.57	-	-	-	-	8.52
0.25	2.97	2.53	2.10	1.71	1.62	1.49	8.40
0.5	2.95	2.52	2.09	1.71	1.61	1.48	8.35
0.75	2.98	2.55	2.11	1.73	1.63	1.49	8.45
1	2.99	2.56	2.12	1.74	1.63	1.50	8.47

On the other hand, the peak position and the full width at half maximum (FWHM) of the (311) plane are used to calculate the average crystallite size (D), the X-ray density (ρ_x), the tetrahedral radius (r_A), and the octahedral radius (r_B). For calculating the crystallite size, the Scherrer equation is proposed (12):

$$D = \frac{0.9\lambda}{\beta cos\theta} \tag{12}$$

Where β is the FWHM, and θ is the Bragg's angle; FWHM and the peak position are estimated by fitting a Lorentzian model to the highest peak (311) (Sivakumar et al., 2011). In contrast, the crystallite size is also obtained by creating a Williamson-Hall (W-H) plot for each sample (except for x=0, given that it does not have the needed peaks for the plotting). For this, the next equations are followed (13) (14):

$$\beta = \beta_{size} + \beta_{strain} \tag{13}$$

$$\frac{\beta cos\theta}{\lambda} = \frac{k}{D} + \frac{4\varepsilon\, sin\theta}{\lambda} \tag{14}$$

Where, β_{size} is FWHM due to the effect of crystallite size only, β_{strain} is the FWHM due to the effect of micro-strain only, and ε is the lattice strain (Hwang et al., 2020). In Figure 11, the W-H plots with the respective Lorentzian fit of all samples are presented, while a comparison between both crystallite size values (nm) and the lattice strains are shown in Table 4.

A difference of 12.46 to 12.81% can be observed in all cases, and the value of the lattice strain is negative in all cases, which indicate the presence of a compressive microstrain. This was found to increase with the content of Zn^{2+}, while the lattice parameter increased as well.

Table 4. Comparison between size values of $Ni_{1-x}Zn_xFe_2O_4$ ferrite samples with x=0, x=0.25, x=0.5, x=0.75, and x=1.0 obtained by Lorentz model and W-H plot.

x	FWHM [rad]	2θ [°]	D [nm] by Lorentz model	D (nm) by W-H plot	ε	%Diff
0	2.90	34.94	5.02	-	-	
0.25	0.51	35.46	28.59	25.19	-0.054	12.63
0.5	0.77	35.66	18.86	16.59	-0.083	12.81
0.75	1.93	35.25	7.54	6.65	-0.204	12.50
1	2.00	35.19	7.29	6.44	-0.211	12.46

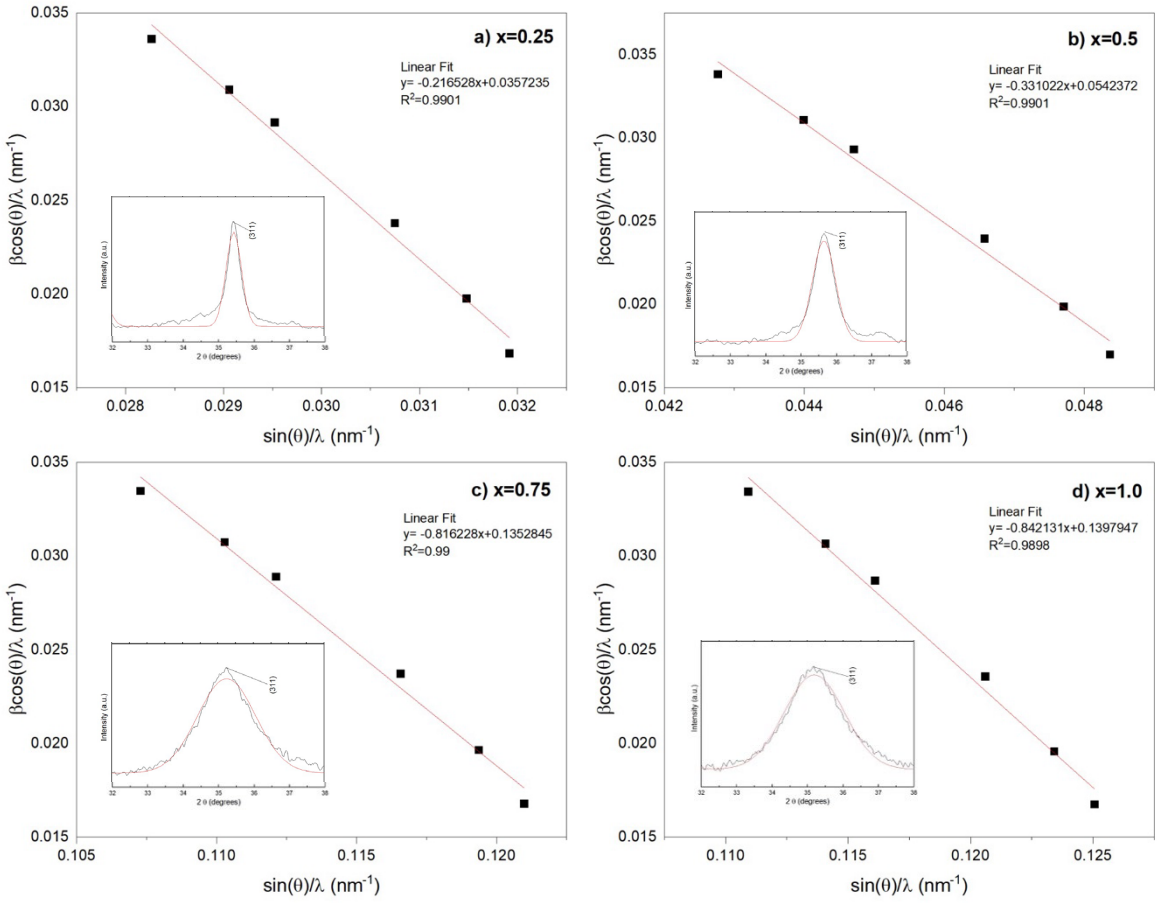

Figure 11. W-H plots of $Ni_{1-x}Zn_xFe_2O_4$ with a) 0.25, b) 0.5, c) 0.75, and d) 1.0, with a frame of the Lorentzian fit of the (311) plane.

The previous phenomenon can be explained by several reasons. Firstly, it can be provoked by a cation substitution of iron ions in the crystal lattice, which could lead to a mismatch in size, causing local distortions. Additionally, when Zn^{2+} (larger ion size in comparison to Fe^{3+} and Ni^{2+}) is incorporated into the lattice, it alters the distribution of cations between A and B sites, creating differences in bond lengths and angles, which could lead to adjustments to accommodate new ionic sites (Heuver et al., 2015) (Tasleem et al., 2013).

Besides, the applied sintering could lead to transformations during heating or cooling cycles, which may also contribute to compressive strains (B. G. Kim et al., 2001). In relation, in the XRD patterns, additional peaks can be observed, which could indicate the presence of impurities of hematite with (012) and (104) planes, at 24° and 32°, respectively, and a type of nickel oxide with (002) and (111), at 32° and 46°, respectively (Srivastava & Srivastava, 2010), (Zainuri, 2017), (Zou et al., 2018).

To determine the value of X-ray density, the next equation is used (15):

$$\rho_x = \frac{ZM}{N_A V_c} \tag{15}$$

Where Z is the number of molecules per unit cell (Z=8), M is the molecular weight of the ferrite, N_A is the Avogadro's number (N_A= 6.023x10^{23} atoms per mole), and V_c is the unit cell volume ($V=a^3$). Additionally, to calculate the radii of tetrahedral (16) and octahedral sites (17), these relations are used:

$$r_A = [C_{Zn} r(Zn^{2+}) + C_{Fe} r(Fe^{3+})] \tag{16}$$

$$r_A = \frac{1}{2}[C_{Ni} r(Ni^{2+}) + C_{Fe} r(Fe^{3+})] \tag{17}$$

Where $r(Zn^{2+})$ is the ionic radius of zinc ion (A site: 0.570 Å), $r(Ni^{2+})$ is the ionic radius of nickel ion (B site: 0.690 Å), $r(Fe^{3+})$ is the ionic radius of iron ion (A site: 0.490, and B site: 0.645 Å), and $C_{M=Zn,Ni,Fe}$ is the percent of metal ions in the sample. To accurately evaluate these two values, an estimation can be made by the percentage obtained in EDX analysis.

In Figure 12, the SEM images of the $Ni_{1-x}Zn_xFe_2O_4$ with x=0, 0.25, 0.5, 0.75 and 1.0 are presented with 100x and 150 x magnifications. The images show that calcined powder nanoparticles are very small (<50 nm), resulting in a high surface tension that causes them to agglomerate. This phenomenon happens frequently in small magnetic nanoparticles, however, when they are sintered, the morphology is softer, produced by van der Waals forces (Costa et al., 2009).

Besides, the EDX spectra of the samples are added in Figure 12. Specifically, in Table 4, the content of identified atoms for each sample is presented, additionally, the atomic percentage of the relevant elements (Ni, Zn, Fe, O) are listed by normalizing the data without considering the contaminants.

Table 4. EDX atomic percentage and normalized atomic percentage of $Ni_{1-x}Zn_xFe_2O_4$ with x=0, x=0.25, x=0.5, x=0.75, and x=1.0.

x	EDX Atomic Percentage								
	Fe	**O**	**Ni**	**Zn**	**C**	**Al**	**Si**	**Cl**	**Na**
0	14.37	37.28	4.29	-	42.13	0.80	0.61	0.21	0.29
0.25	17.12	54.39	5.68	6.02	14.65	1.32	0.32	0.53	-
0.5	13.77	37.19	3.58	4.96	38.28	0.90	1.10	0.22	-
0.75	12.43	49.30	4.71	7.98	23.83	1.17	0.48	0.09	-
1	16.38	37.46	-	9.42	35.50	0.93	0.27	0.05	-

x	EDX Normalized Atomic Percentage			
	Fe	**O**	**Ni**	**Zn**

0	25.69	66.64	7.67	-
0.25	20.57	65.35	6.82	7.23
0.5	23.14	62.50	6.02	8.34
0.75	16.70	66.25	6.33	10.72
1	25.91	59.24	-	14.98

To determine the value of X-ray density, a comparison between the theoretical data (considering the expected x value for each sample) and the experimental values is made. In the Table 5, the calculated values of x-ray density and the theoretical and experimental values of A and B sites radii are presented. Furthermore, the percentage error is calculated for each radius.

Table 5. Molecular weight, X-ray density, theoretical and experimental values of A and B sites radii, and their percentage error of $Ni_{1-x}Zn_xFe_2O_4$.

x	M [g/mol]	ρ_x [g/cm^3]	Theoretical		Experimental		%Error (r_A)	%Error (r_B)
			r_A	r_B	r_A	r_B		
0	234.38	5.04	0.14	0.28	0.13	0.22	-10.09	-22.71
0.25	236.05	5.29	0.16	0.26	0.14	0.18	-11.45	-30.39
0.5	237.72	5.43	0.18	0.23	0.16	0.19	-10.95	-18.32
0.75	239.40	5.28	0.20	0.21	0.14	0.15	-28.91	-27.54
1	241.07	5.29	0.22	0.18	0.21	0.17	-4.10	-9.31

As can be observed, the experimental of A and B sites radii values in all cases are lower in comparison to the theoretical values, contributing to the explanation of the compressive

strain. Besides, the high error percentage of the sample with x=0.25 is related to the presence of different XRD peaks that involves the formation of secondary phases, such as hematite and nickel oxides. However, it should be established that the EDX spectra only shows the superficial composition of the samples, which means that the atomic percentage is not necessarily the actual conformation.

Then, also remembering that the oxygen percentage in the ferrites with x=0.25 is almost three times the atomic percentage of iron, the sample is more likely to be superficially oxidized, meaning that the diffraction peaks corresponding to iron and nickel oxides are components of a superficially modified ferrite nanocomposite. Furthermore, it should be noted that it exists an important contamination of carbon in all the samples, which could corresponds to the formation of carbon dots during synthesis and/or sintering, and the contribution of the carbon tape used for sample preparation (Rabi et al., 2020).

Additionally, contamination by Cl and Na could be related to the participation of ions during synthesis that did not get washed out, while the Si content can be explained by the detachment of particles from crystal recipients and/or agate mortar during the pulverization of the ferrite powders and their manipulation.

In Figure 13, the FTIR spectra of $Ni_{1-x}Zn_xFe_2O_4$ with x=0, x=0.25, x=0.5, x=0.75, and x=1.0, are presented. They showed the characteristic peaks of ferrite nanoparticles, with slight variations in peaks around 385 and 560 cm^{-1}, which are related to the octahedral and tetrahedral complexes, respectively. Remembering that zinc is mainly replace in A site, while nickel establishes in B sites, the band corresponding to octahedral site reduces its intensity as the Zn^{2+} increases (Taha et al., 2018).

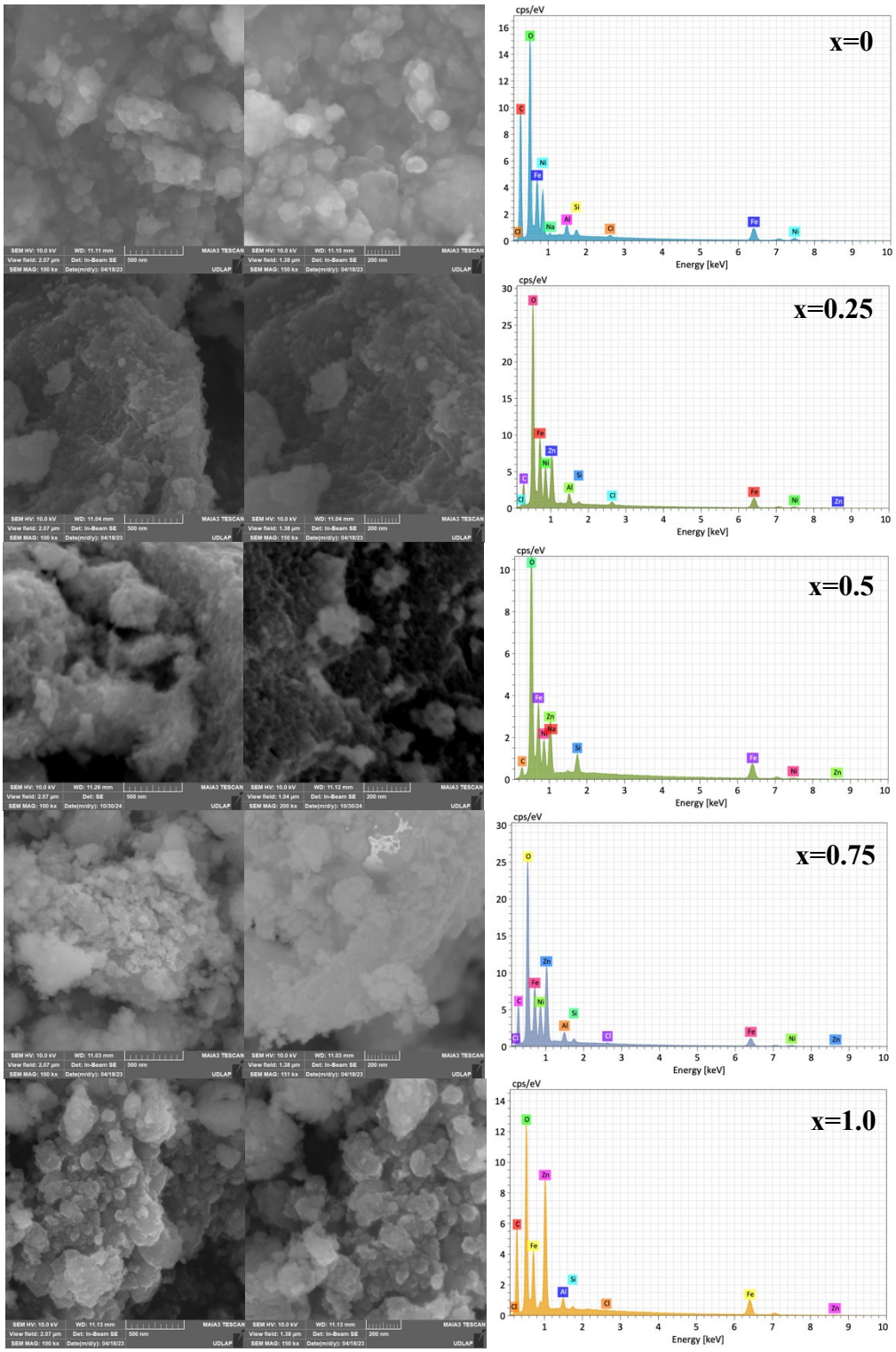

Figure 12. SEM images of $Ni_{1-x}Zn_xFe_2O_4$ with x=0, 0.25, 0.5, 0.75 and 1.0 using 100x and 150x magnifications, and their respective EDX spectra.

Additionally, the peak around 950 cm^{-1} is related to the stretching vibrations of the bivalent metal-oxygen bonds in the crystal lattice (Basha et al., 2024). The bands around 1640 cm^{-1} and 3400 cm^{-1} are commonly assigned to stretching vibrations of bonded -OH and H-O-H of adsorbed water hydroxyl ions (Pathak et al., 2010). The peak around 1640 cm^{-1} can be also be collapsed with an asymmetric stretching vibration of C-O carbonyl groups (Taha et al., 2018). Besides, the peaks around 1565 to 1340 cm-1, are mainly related to the stretching of the bonding Fe-OH (Iglesias et al., 2019).

Furthermore, the Raman spectra of the five samples are shown in Figure 14a, and in Table 6, the information about the peak location, the elements participating, and the type of bonding is presented. Remembering that there are eight formula units per unit cell, and that of the 56 atoms in the complete cells, only 14 atoms comprise in the smallest Bravais cell, the number of possible vibrational modes is 42. Given the group theory, the predicted optical phonon distribution is $5T_{1u}+A_{1g}+E_g+3T_{2g}$, being only $5T_{1u}$ an infrared-active mode, while the other five are Raman-active modes caused by the motion of oxygen ions and A- and B-sites ions (Yadav et al., 2019). In addition, the patterns also have bands around 1200-1350 cm-1, which corresponds to the magnon excitation (Figure 14b) (Aliyeva et al., 2017)

Table 6. Characteristic peaks of Raman spectra of $Ni_{1-x}Zn_xFe_2O_4$, with x=0, x=0.25, x=0.5, x=0.75, and x=1.0 (Yadav et al., 2019), (Aliyeva et al., 2017), (Ehi-Eromosele et al., 2015).

Raman-active mode	**Raman shift (cm^{-1})**					**Intensity**	**Description**
	0	**0.25**	**0.5**	**0.75**	**1.0**		
T_{2g} (1)	200	247	200	240	232	Weak	Translatory movement of the complete Fe_2O_4 unit
E_g	314	301	313	323	292	Weak	O symmetric bends with respect to Fe

T_{2g} (2)	471	474	480	478	460	Moderate	Asymmetric stretching of Fe and O
E	536	514	495	511	500	Moderate	O symmetric bends with respect to Fe
T_{2g} (3)	578	567	565	-	-	Weak	Asymmetric bends of O with Fe
A_{1g}	678	683	659	-	-	Strong	Symmetric stretching of O atoms along Fe-O bonds
A_{1g} (1)	-	-	-	593	584	Strong	
A_{1g} (2)	-	-	-	665	662	Strong	

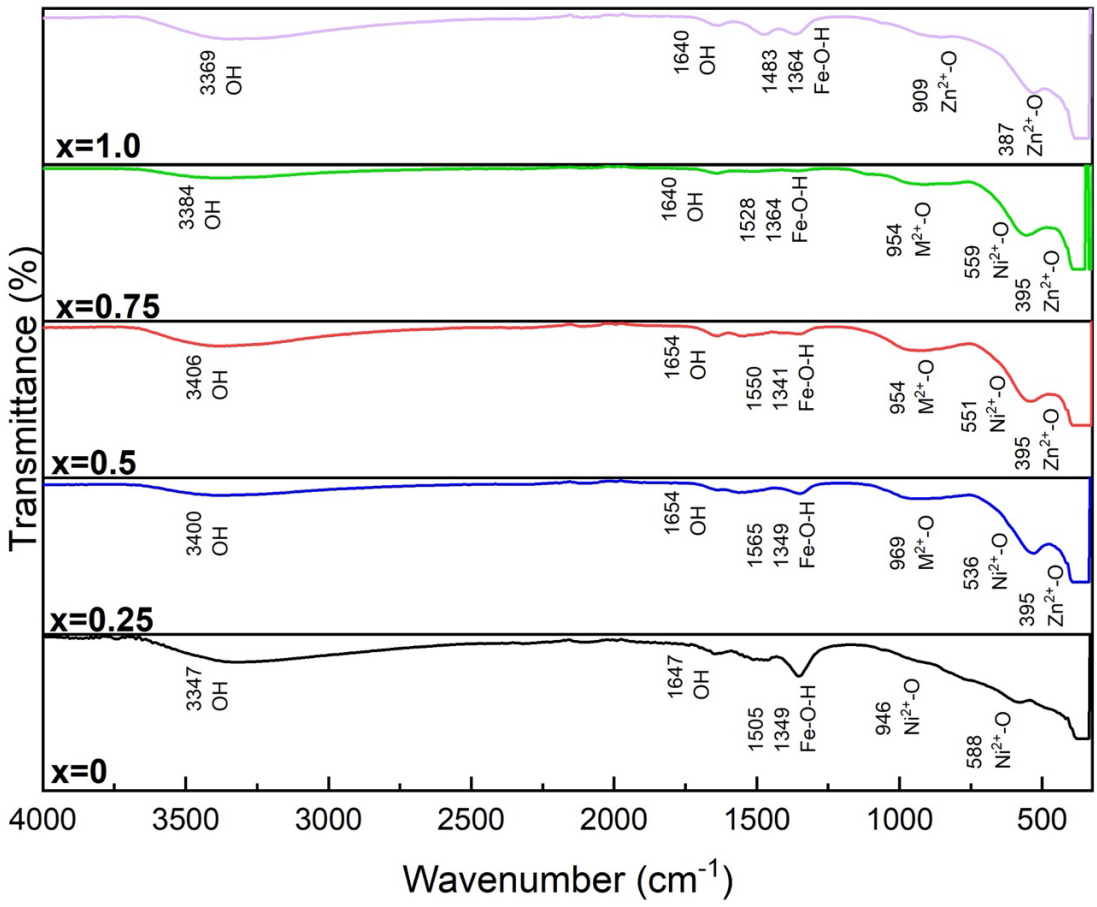

Figure 13. FTIR spectra of $Ni_{1-x}Zn_xFe_2O_4$ with x=0, 0.25, 0.5, 0.75, and 1.0, with their characteristic bands assigned.

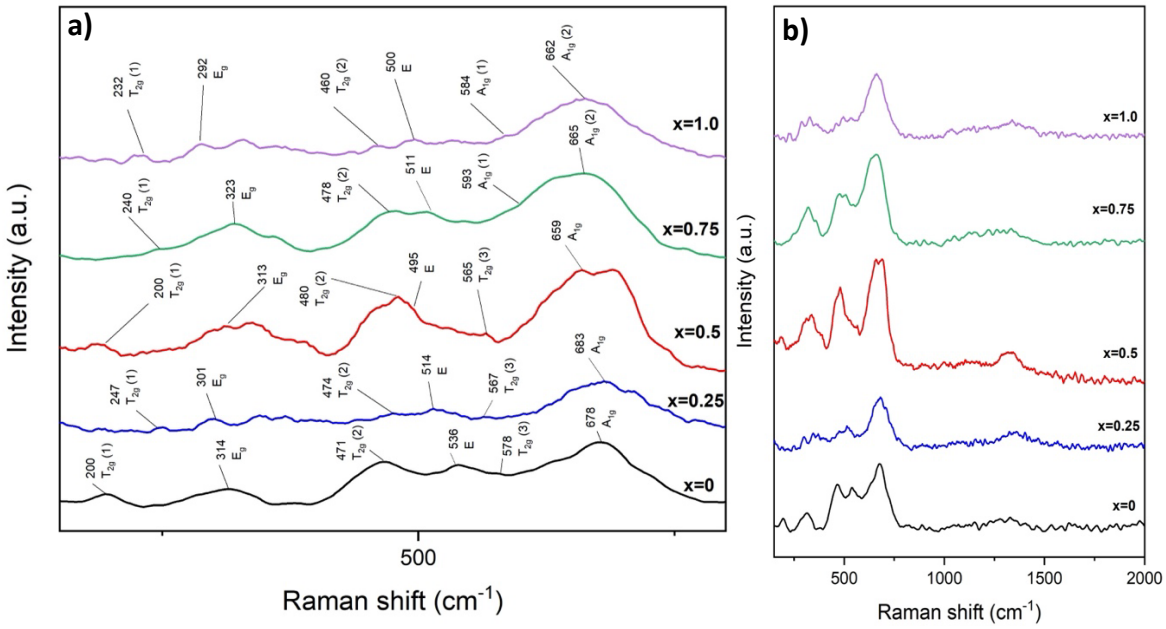

Figure 14. Raman spectra of $Ni_{1-x}Zn_xFe_2O_4$ with x=0, 0.25, 0.5, 0.75, and 1.0, a) at a range of 150-800 cm^{-1} with their characteristic bands assigned and b) with a range of 150–2000 cm^{-1}.

6.2 Physicochemical characterization of Ni1-xFe2O4 ferrite nanoparticles after acidic treatment

In order to achieve a better solubility and stability, ferrite nanoparticles were treated with an acidic solution (HCl 10%). The XRD patterns of the ferrites containing x=0.25, 0.5, and 0.75 are shown in Figure 15. Characteristic peaks related to planes (111), (220), (311), (222), (400), (422), (511), (333) and (440) are shown at 35°, 41.5°, 50.5°, 63°, 67.5°, and 74° peak positions. In comparison to the ferrite nanoparticles synthesis without acidic treatment, in these XRD patterns no additional peaks corresponding to secondary phases cannot be seen. It is important to highlight that a shift of approx. 5° in peak positions can be seen, given that the X-ray radiation source changed to a Co (1.78901 Å).

This could indicate that the components presented in the sample x=0.25 before the acidic treatment, which were proposed to be hematite and nickel oxide phases, are mainly superficial and were dissolved by interacting with the acidic solution, following any of the next possible reactions (Lin & Popp, 1984):

Nickel oxide dissolution

$$NiO_{(s)} + 2HCl^{0}_{(aq)} \rightarrow NiCl^{0}_{2\,(aq)} + H_2O \quad (18)$$

$$NiO_{(s)} + 2HCl^{0}_{(aq)} \rightarrow NiCl^{+}_{(aq)} + Cl^{-}_{(aq)} \quad (19)$$

$$NiO_{(s)} + 2HCl^{0}_{(aq)} \rightarrow Ni^{2+}_{(aq)} + 2Cl^{-}_{(aq)} \quad (20)$$

Hematite dissolution

$$Fe_2O_{3\,(s)} + 6HCl^{0}_{(aq)} \rightarrow 2FeCl_3 + 3H_2O \quad (21)$$

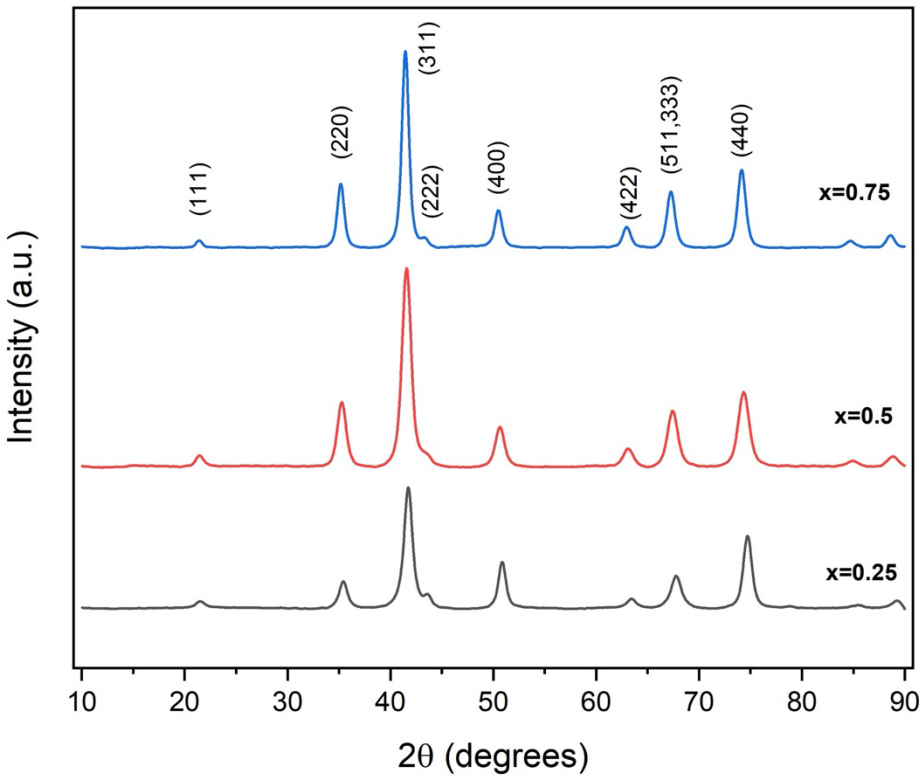

Figure 15. XRD diffractograms of $Ni_{1-x}Zn_xFe_2O_4$ with x=0, 0.25, 0.5, and 0.75 after the acidic treatment with their characteristic planes assigned.

As was performed for the previous XRD results, the peak position of the characteristic peaks as well as the interplanar distances are shown in Tables 7 and 8, respectively, both calculated with the equations (10) and (11). From these, it is possible to calculate the values of crystallite size by the proposed methods using Lorentz models and W-H plots (following eq. 14). The W-H plots of all samples are presented in Figure 16, with the addition of the Lorentzian fit for the (311) plane.

Table 7. Peak position of characteristic peaks of $Ni_{1-x}Zn_xFe_2O_4$ ferrite samples with x=0.25, x=0.5 and x=0.75, after acidic treatment.

x	**Peak position: 2θ(°)**					
	(2 2 0)	**(3 1 1)**	**(4 0 0)**	**(4 2 2)**	**(5 1 1)**	**(4 4 0)**
0.75	35.17	41.46	50.50	62.96	67.26	74.13
0.50	35.28	41.58	50.64	63.13	67.59	74.32
0.25	35.42	41.73	50.86	63.42	67.77	74.71

Table 8. Interplanar distances of characteristic peaks of $Ni_{1-x}Zn_xFe_2O_4$ ferrite samples with x=0.25, x=0.5 and x=0.75 after acidic treatment, and lattice parameter considering the (311) plane.

x	**Interplanar distances (Å)**						**Lattice**
	(2 2 0)	**(3 1 1)**	**(4 0 0)**	**(4 2 2)**	**(5 1 1)**	**(4 4 0)**	**parameter (Å)**
0.25	2.96	2.53	2.10	1.71	1.62	1.48	8.38
0.50	2.95	2.52	2.09	1.71	1.61	1.48	8.36
0.75	2.94	2.51	2.08	1.70	1.60	1.47	8.33

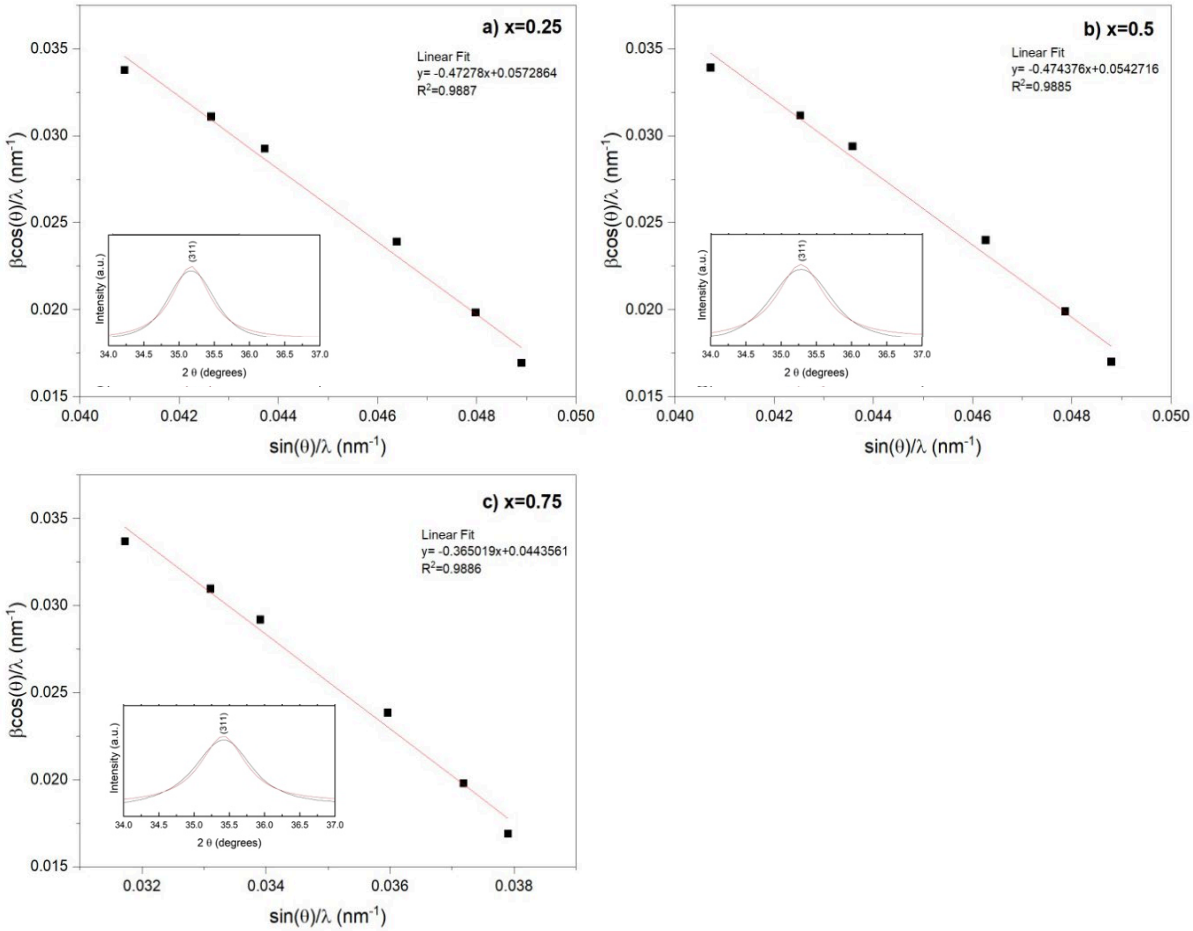

Figure 16. W-H plots of $Ni_{1-x}Zn_xFe_2O_4$ with a) 0.25, b) 0.5 and c) 0.75 after treatment with acidic solution, with a frame of the Lorentzian fit of the (311) plane.

In Table 9, the size values calculated from both methods are compared, obtaining in all cases a percentage difference of 16.51-17.68%, being the obtained strain values negative, indicating that these samples still present a compressive strain behavior. In addition to the possible reasons of the compression by effect of the lattice strain (sintering process, formation of additional components and substitution of iron sites by zinc ions), it has been

reported that an acidic treatment can induce this phenomenon, involving also the compression of the material strength and modulus (Rudawska, 2020).

Table 9. Comparison between size values of $Ni_{1-x}Zn_xFe_2O_4$ ferrite samples with x=0.25, x=0.5 and x=0.75 after acidic treatment obtained by Lorentz model and W-H plot.

x	FWHM [rad]	2θ [°]	D [nm] by Lorentz model	D (nm) by W-H plot	ε	%Diff
0.25	0.71	41.46	24.20	20.29	-0.09	-17.58
0.5	0.92	41.58	18.76	15.71	-0.12	-17.69
0.75	0.92	41.73	18.80	15.93	-0.11	-16.51

On the other hand, values of X-ray density (eq. 15), and the radii of tetrahedral (eq. 16) and octahedral sites (eq. 17) are calculated considering the theoretical composition of the respective samples, and then values are compared with experimental data extracted from the EDS spectra (Figure 13). In the Table 10, the atomic percentage of all elements involved is presented, as well as a normalized atomic percentage considering the participating elements in the ferrite nanoparticles structure.

It is important to mention that in the obtained SEM images (Figure 17), the magnetic nanoparticles still show a very small size, provoking their agglomeration due to the high surface tension. Additionally, their form is very similar to the initially synthesized formed nanoparticles, showing a *quasi*-spherical morphology.

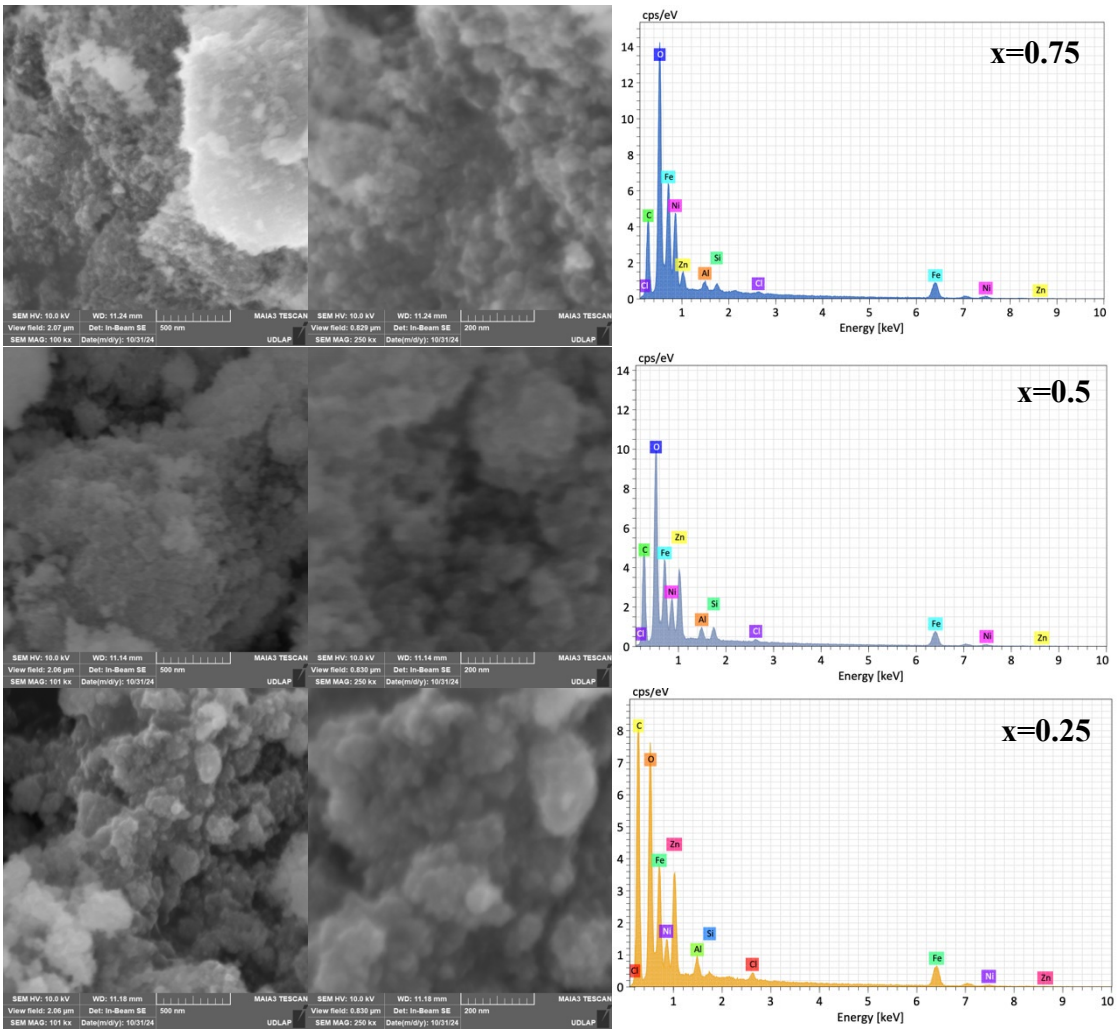

Figure 17. SEM images of $Ni_{1-x}Zn_xFe_2O_4$ with x=0.25, 0.5, and 0.75 after acidic treatment using 100x and 150x magnifications, and their respective EDX spectra.

Table 10. EDX atomic percentage and normalized atomic percentage of $Ni_{1-x}Zn_xFe_2O_4$ with x=0, x=0.25, x=0.5, x=0.75, and x=1.0 after acidic treatment.

x	EDX Atomic Percentage								
	Fe	O	Ni	Zn	C	Al	Si	Cl	Na
0.25	16.32	43.47	6.95	3.21	14.69	0.71	0.70	0.19	-
0.5	13.77	37.19	3.58	4.96	38.28	0.9	1.10	0.22	-

0.75	11.44	27.83	1.56	3.55	54.41	0.69	0.18	0.34	-

x	EDX Normalized Atomic Percentage			
	Fe	O	Ni	Zn
0.25	23.33	62.14	9.94	4.59
0.5	23.14	62.50	6.02	8.34
0.75	25.78	62.71	3.52	8.00

Using the previous information, X-ray density and theoretical and experimental values of A and B sites radii are presented in the Table 11, in which the percentage error was found to be negative, supporting the obtained information about the compressive strain behavior. Additionally, an important difference in content between Ni and Zn in the sample x=0.5 can be seen, having a considerably lower content of Ni, which could affect to its magnetic performance. However, it should be highlighted that this analysis gives more information about the superficial content of the samples.

Table 11. Molecular weight, X-ray density, theoretical and experimental values of A and B sites radii, and their percentage error of $Ni_{1-x}Zn_xFe_2O_4$ ferrites after acidic treatment.

x	M [g/mol]	ρ_x [g/cm^3]	Theoretical		Experimental		%Error (r_A)	%Error (r_B)
			r_A	r_B	r_A	r_B		
0.25	236.05	5.32	0.160	0.258	0.140	0.219	-12.396	-15.162
0.5	237.72	5.41	0.160	0.258	0.161	0.191	0.353	-26.111

0.75	239.4	5.50	0.181	0.234	0.172	0.191	-4.865	-18.411

x=0.25 **x=0.5** **x=0.75**

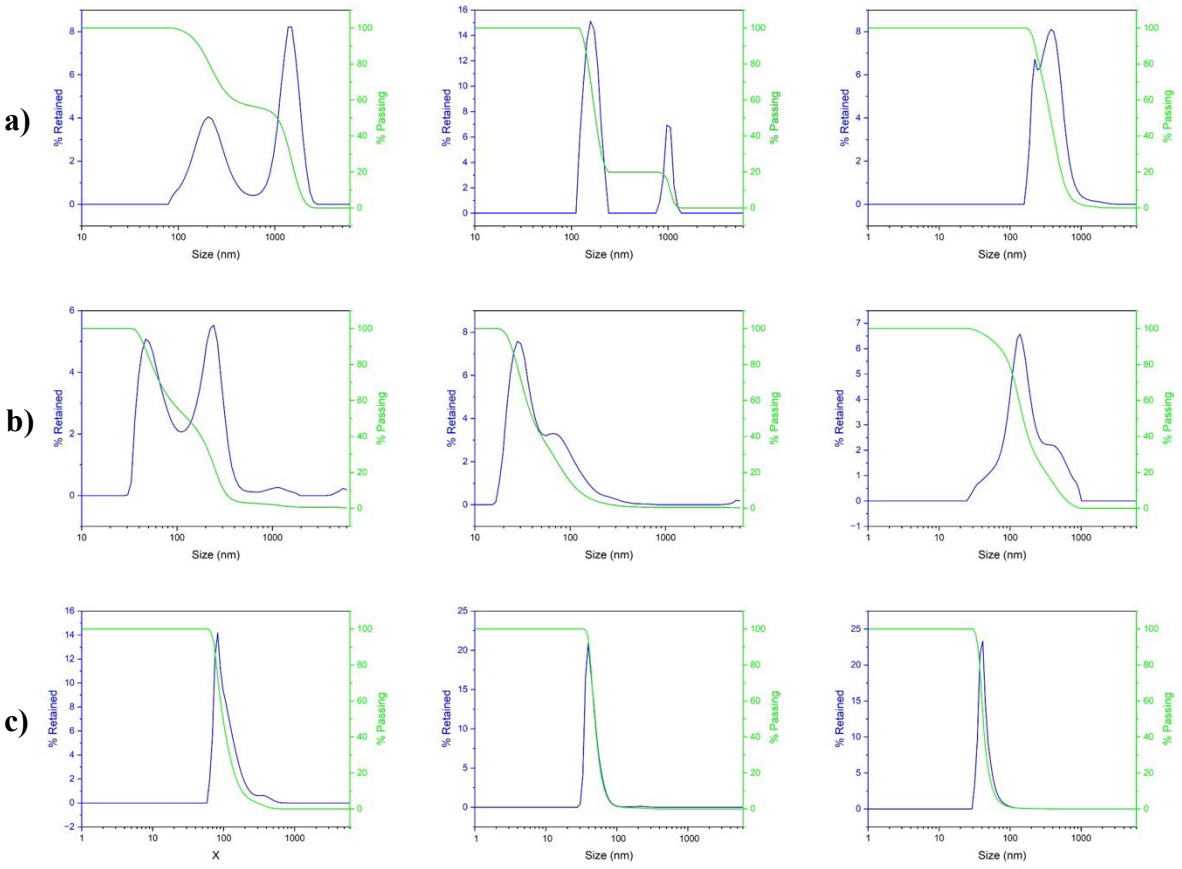

Figure 18. DLS spectra of $Ni_{1-x}Zn_xFe_2O_4$ with x=0.25, 0.5 and x=0.75 (a) before acidic treatment using Intensity mode, and after acidic treatment using (b) Intensity and (c) Number modes.

In Figure 18, the DLS spectra of the ferrite nanoparticles with x=0.25, 0.5, and 0.75 before and after acidic treatment is compared. Specifically, the intensity modes are shown, and the number mode is added to estimate the most relevant group of nanoparticles, ignoring the possible agglomerates that have the possibility to diffract higher quantities of light.

Analyzing the intensity mode, ferrite nanoparticles before the acidic treatment are highly agglomerated as they show different populations close to 1000 nm, but when they interact with the acidic solution, the populations reduce their difference almost forming only one, resulting in a more linear slope of passing percentage.

Additionally, in the size distribution by Number mode, the most relevant population of the samples is conformed by particles agglomerating at ranges below 100 nm, indicating better stability in comparison to the initial conformations.

6.3 Magnetic hyperthermia

For the determination of the performance of the $Ni_{1-x}Zn_xFe_2O_4$ as a magnetic hyperthermia agent, tests using the magneTherm equipment were performed at different concentrations (4, 8, 16, 32 mg/mL) using a magnetic field of 17.94 mT, (179.4 Oe) and a frequency of 329.9 Hz. In Figure 19, a comparison between the magnetic behavior of the ferrite nanoparticles with x=0.25, 0.5, and 0.75, is presented. As can be inferred from the results, the synthesized and calcined ferrite nanoparticles resulted in an increase of heating performance as the content of nickel ions is higher, being the sample with x=0.25 the one with better magnetic hyperthermia performance.

Specifically, the system with x=0.75 showed a nearly homogeneous performance by increasing approx. 3.5°C after 300 s when its concentration is 32 or 16 mg/mL. When the latter value drops to 8 and 4 mg/mL, their maximum heating value reduces to almost 1°C. In contrast, the sample with better heating performance is the one with x=0.25, which showed a maximum temperature increasement of nearly 30°C when its concentration is 32 mg/mL,

showing a curve behavior. When dropping to 16 and 8 mg/mL, the maximum temperature diminished to 8-7.5°C, while with 4 mg/mL, the value decreased to 3°C.

Additionally, having x=0.5, the heating performance presented a similar form of the plots, resulting in a maximum temperature of nearly 10°C when the concentration is 32 mg/mL, but then showing a considerable diminution for 16, 8 and 4 mg/mL, all three with very similar slope and values, reaching a maximum temperature of almost 3°C.

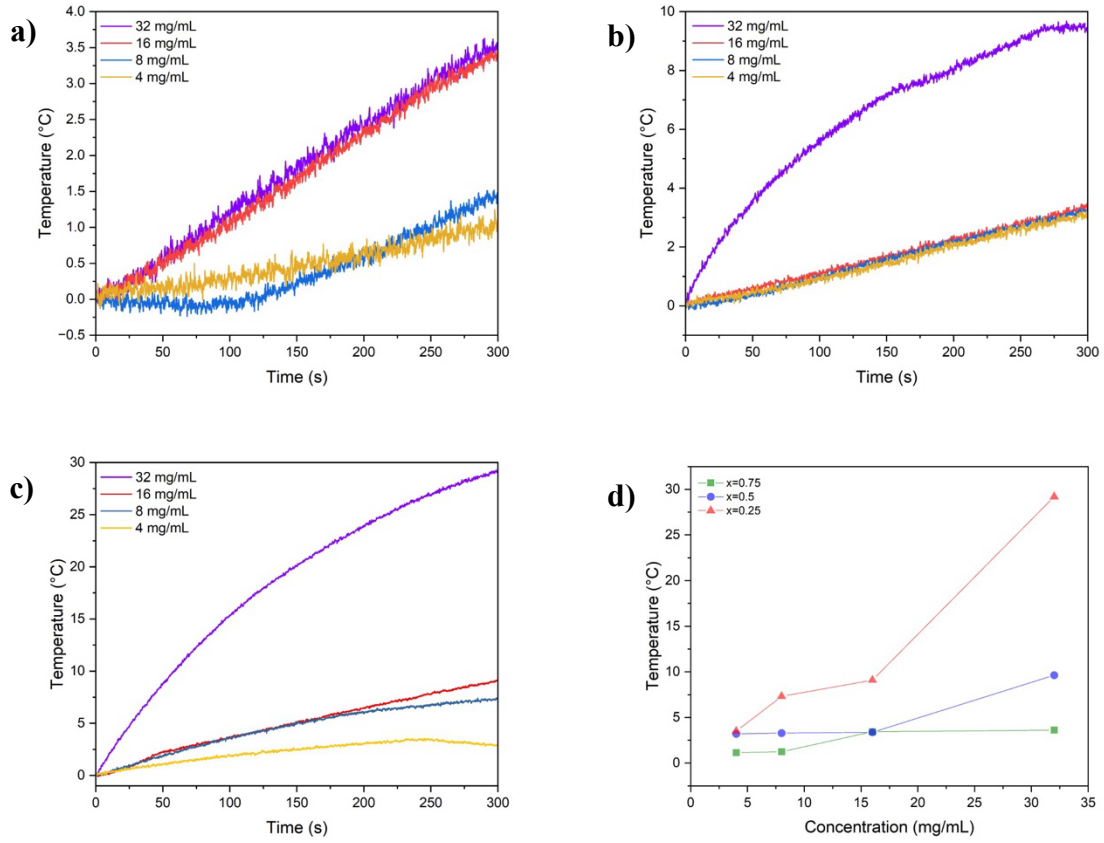

Figure 19. Magnetic hyperthermia performance of $Ni_{1-x}Zn_xFe_2O_4$ with x=a) 0.25, b) 0.5, and c) 0.75, and d) a plot comparing the maximum values for each concentration.

The previous results could be explained by the possible inclusion of secondary phases in the sample x=0.75, specifically, nickel oxide and hematite. As discussed before, these could be components of the sample included in the surface acting as a sort of core-shell alike structure,

given that after the acidic treatment, the presence of these impurities were deleted. Additionally, this behavior could be attributed to the magnetic performance of the nickel oxide component, as it has been reported that usually has an antiferromanetic behavior, but when increasing the annealing temperature above 600°C, it starts to show a superparamagnetic behavior, improving its magnetic properties, such as magnetization and coercivity. Being also both parameters favored by the decreasing of the crustallite size, strain, and lattice constant (Jafari et al., 2019).

It is important to mention that, the value of the specific absorption rate (SAR, also known as the specific power loss, SLP) of the dispersed nanoparticles in water can be obtained by the following equation (22), slightly modified from (6):

$$SAR = c\left(\frac{dT}{dt}\right)\left(\frac{m_s}{m_m}\right) \tag{22}$$

Where c is the specific heat capacity of water (4.186 J/g°C), m_s and m_m are the masses of the suspension and the nanoparticle in the suspension, respectively, and dT/dt is the maximum of the derivative (slope) that occurs within few seconds after intiate the process (Salunkhe et al., 2016). Considering the previous equations, the SAR of the three samples at the different concentrations are estimated in Table 12.

Table 12. SAR of $Ni_{1-x}Zn_xFe_2O_4$ ferrite nanoparticles with x=0.25, 0.5, and 0.75 at 32, 16, 8, and 4 mg/mL.

x	Specific absorption rate (SAR) (W/g)			
	32 mg/mL	**16 mg/mL**	**8 mg/mL**	**4 mg/mL**
0.25	28.35	7.65	12.81	11.04

0.5	18.69	2.88	6.00	11.10
0.75	1.59	3.10	2.80	3.48

In Figure 20, the magnetic hyperthermia performance of the ferrite nanoparticles after the acidic treatment for stabilization is shown at the same concentrations of 32, 16, 8, and 4 mg/mL (except for x=0.5, given that there was not enough sample to characterize at 32 mg/mL), using the same parameters for the magnetic field. In the Table 13, the SAR values are reported.

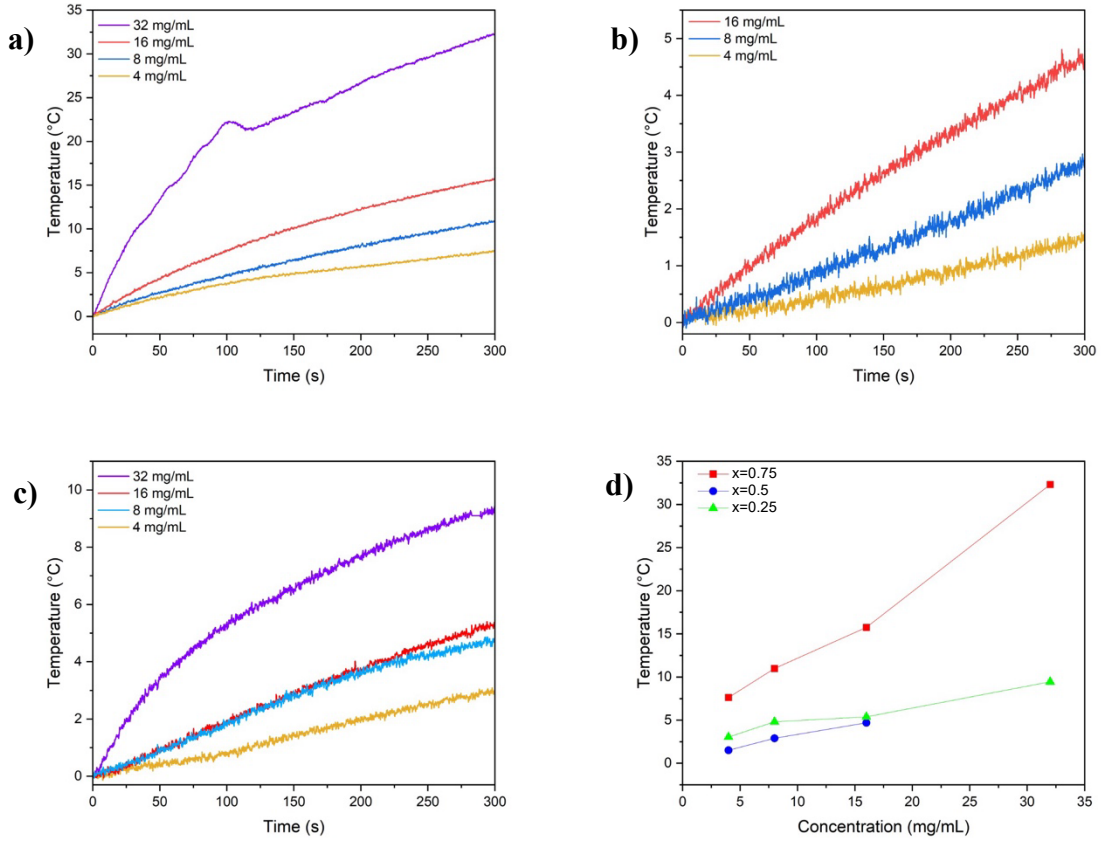

Figure 20. Magnetic hyperthermia performance of $Ni_{1-x}Zn_xFe_2O_4$ with x=a) 0.75, b) 0.5, and c) 0.25 after acidic treatment, and d) a plot comparing the maximum values for each concentration.

Table 13. SAR of $Ni_{1-x}Zn_xFe_2O_4$ ferrite nanoparticles with x=0.25, 0.5, and 0.75 after acidic treatment at 32, 16, 8, and 4 mg/mL.

x	Specific absorption rate (SAR) (W/g)			
	32 mg/mL	**16 mg/mL**	**8 mg/mL**	**4 mg/mL**
0.25	9.28	4.17	7.89	15.86
0.5	-	5.29	5.66	4.94
0.75	46.94	23.01	36.85	44.34

As can be seen in Figure 20d and in the SAR Tables 12 and 13, after the acidic treatment, the ferrite nanoparticles with x=0.75 perfomed the best magnetic hyperthermia performance as it achieve a maximum temperature of 33°C approx. with a SAR of 46.94 W/g. This in contrast to the best result in the ferrite nanoparticles before the acidic treatment, being x=0.25 with nearly 30°C and SAR of 28.35 W/g.

The disminution of the x=0.25 sample could be related to the dissolution of the nickel oxide and hematite phases formed in the surface during the sintering process by acting of the HCl solution. However, the x=0.75 presents a remarkable performance, which could be related to the reduction and/or relocation of cations in the spinel lattice during the stabilization process (Kmita et al., 2021).

6.4 Carboxymethylation of chitosan

The carboxymethylation of chitosan was confirmed by the FTIR analysis presented in Figure 21a. Between the main assigned peaks of the chitosan, the wide band at 3000-3600 cm^{-1}

corresponds to N-H and O-H stretching, involving also the intramolecular hydrogen bonds. Besides, the bands at 2905 and 2870 cm^{-1} can be related to the C-H symmetric and asymmetric stretching, respectively. The peaks at 1654 and 1659 cm^{-1} can be attributed to the C=O stretching and NH_2 deformation, while the bands at 1423 and 1375 cm^{-1} are related to the bending of CH_2 and the symmetrical deformation of CH_3, respectively. 1070 cm^{-1} peak corresponds to the stretching in C-O-C bridges (Chen et al., 2004), (Fernandes Queiroz et al., 2015).

In comparison to the chitosan sample, carboxymethylation of the sample shows a much less wide band at 3000-3600 cm^{-1} given that the N-H stretching is no longer contributing. Besides, the peak 1580 indicate the formation of the carboxymethyl groups, being related to the stretching of -COO-. At 1377 cm^{-1}, occurs the deformation of the group -CH2COOH (Fernandes Queiroz et al., 2015).

In Figure 21b, the Raman spectra of both samples are presented, being in accordance to the peaks proposed in the literature, finding a slight shift backwards from CMC sample (Mondéjar-López et al., 2024). In addition, in Figure 22, the SEM micrograph of carboxymethyl chitosan is presented, showing that this sample is not crystalline, and is completely amorphous.

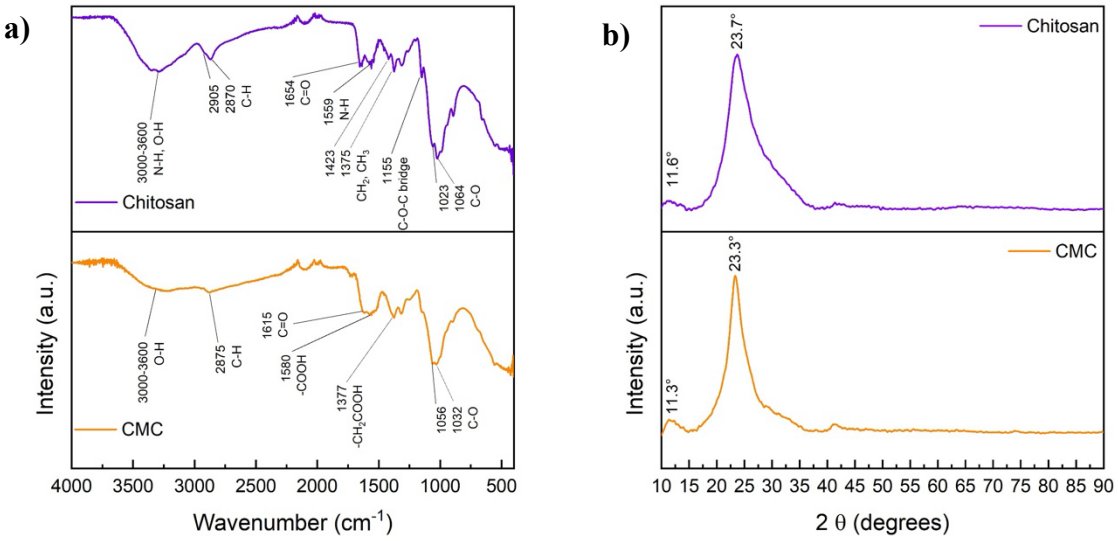

Figure 21. a) FTIR spectra of chitosan, and CMC, and their corresponding b) Raman spectra.

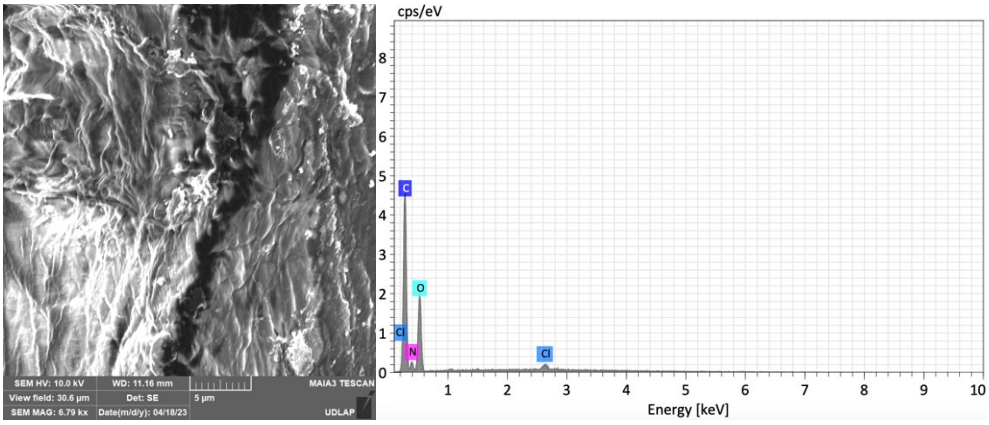

Figure 22. SEM images (10x) of carboxymethyl chitosan with its corresponding EDX spectra.

6.5 Synthesis and characterization of nanofibers / nanocomposites

In Table 14, a summary of all the tested samples in electrospinning process with conditions and concentrations of PVA, PVA/CMC, PVA/Ch, PVA/Ch/ferrite nanoparticles, and PVA/CMC/ferrite nanoparticles is presented, describing the corresponding observations of each one. It is important to mention that CMC/PVA 1:4 v/v solutions using water as solvent was not achievable, as they were not completely soluble in any concentration, probably caused for a nature of partial carboxymethylation (Doshi et al., 2018). Thus, the tests involving CMC were continued by using acetic acid/water (50:50 % v/v) as solvent.

Table 14. Summary of solutions of PVA, PVA/CMC, PVA/CMC/MNPs and PVA/Ch/MNPs tested for electrospinning

Concentrations (wt. %)				Ratio (v/v)	Conditions			Description
PVA	CMC	Ch	$Ni_{1-x}Zn_xFe_2O_4$	CMC:PVA or Ch:PVA	Voltage (kV)	Distance (cm)	Feed rate (mL/h)	
8	-	-	-	-	19	10	0.15	Smooth nanofibers with presence of some beads.
10	-	-	-	-	19	10	0.15	Smooth and homogeneous nanofibers
12	-	-	-	-	19	10	0.15	Nanofibers with a variety of beads.
10	5	-	-	3:1	20	10	0.15	No deposition due to instable jet cone. High viscosity solution.
10	4.5	-	-	3:1	20	10	0.15	No deposition due to instable jet cone. High viscosity solution.
10	4	-	-	3:1	18	8	0.15	No deposition due to instable jet cone. High viscosity solution.

10	3.5	-	-	3:1	19	10	0.15	Formation of like-dust in the collector, not reproducible.
10	3	-	-	3:1	15.5-16	10	0.15	Formation of like-dust in the collector, not reproducible
10	2.75	-	-	3:1	20	15	0.15	Formation of like-dust in the collector, not reproducible
10	2.625	-	-	3:1	21.5	10	0.15	Formation of homogeneous deposition in the collector. Adequate viscosity solution.
10	2.5	-	-	3:1	21.5	10	0.15	Formation of homogeneous deposition in the collector. Adequate viscosity solution.
10	2.0	-	-	3:1	18.5	12.5	0.2	Formation of homogeneous deposition in the collector. Low viscosity solution.
10	-	3	-	3:1	20	10	0.3	Formation of non-homogeneous deposition in the collector, instable jet cone
10	-	2.5	-	3:1	21	15	0.45	Formation of homogeneous deposition in the collector, instable jet cone with droplets presence
10	-	2.0	-	3:1	15 / 20 / 25	15 / 15 / 20	0.4 / 0.3 / 0.3	Formation of homogeneous deposition in the collector, stable jet but droplets presence
10	-	4.0	-	1:3	20 / 25	10 / 15	0.3 / 0.3	No deposition in the collector due to high viscosity solution.
10	-	3.5	-	1:3	20 / 25	10 / 15	0.3 / 0.3	Formation of non-homogeneous deposition in the collector due to high viscosity solution. Instable jet cone.

10	-	3.0	-	1:3	21 / 23	10 / 15	0.3 / 0.3	Formation of homogeneous deposition. Stable jet cone but droplets appearance.
10	-	2.75	-	1:3	19.5 / 23	10 / 15	0.3 / 0.3	Formation of homogeneous deposition. Stable jet cone and homogeneous nanofibers were obtained.
10	-	2.5	-	1:3	19.5 /24	10 / 15	0.3 / 0.5	Formation of homogeneous deposition. Stable jet cone and homogeneous nanofibers were obtained with presence of some droplets.
10	-	2.0	-	1:3	21 / 25	10 / 15	0.3 / 0.3	No deposition in the collector. Instable jet cone due to low viscosity solution.
10	2.625	-	20 per polymer weight (x=0.25)	3:1	25	20	0.5	Formation of homogeneous deposition in the collector, stable jet but droplets presence
10	-	2	20 per polymer weight (x=0.25)	3:1	25	20	0.5	Formation of homogeneous deposition in the collector, stable jet but droplets presence
10	-	2	10 per polymer weight (x=0.25)	1:3	25 / 25	20 / 15	0.5 / 0.5	Formation of homogeneous deposition in the collector, stable jet but droplets presence
10	-	2.75	10 per polymer weight (x=0.25)	1:3	25	15	0.3	Formation of homogeneous deposition in the collector, stable jet but droplets presence.
10	-	2.75	10 per polymer weight (x=0.5)	1:3	20 / 25	10 / 15	0.5 / 0.5	Formation of homogeneous deposition in the collector, stable jet but droplets presence.
10	-	2.75	10 per polymer weight (x=0.75)	1:3	20 / 25	10 / 15	0.5 / 0.5	Formation of homogeneous deposition in the collector, stable jet but droplets presence.

In Figure 23, the SEM images of different results of nanofibers containing only PVA can be visualized. It should be highlighted that size distributions are estimated by using the Fiber analysis tool in Mountains 8 software for analyzing SEM images. Specifically, in Figure 3a, pictures of PVA 8% nanofibers using water as solvent can be seen. The obtained nanofibers are roughly homogeneous with the presence of some beads, resulting in a size average of 34.22 nm $\pm$ 36.32 nm. In contrast, in Figure 23b, smooth and homogeneous PVA 10% nanofibers can be seen, with a size dispersion that indicates that nanofibers have an average size of 53.02 nm $\pm$ 33.93 nm. Both processes were performed using 0.15 mL/h, 19 kV, and 10 cm of distance from the collector to the needle.

In Figure 23c, the electrospinning of the PVA 12% resulted in the formation of beads of 133.5 nm (in average), connected by nanofibers of 32.3 nm (in average), with an overall average size of 53.40 nm $\pm$ 46.55 nm. The conditions were the same as the used for the PVA 10% and 8% processes. The reason behind the beads presence could be that the solution had a higher viscosity (higher concentration), and that the applied voltage increased the electrostatic repulsive force on the charged jet, favoring the bead formation in a constant rate.

On the other hand, in Figure 24a and b, two composites between CMC and PVA (10%) 3:1 v/v with 2.625 wt. % and 2 wt. % of chitosan, respectively, can be seen. Both have a spherical form and are nearly monodispersed, presenting only two important size populations. The first one having 2.625 wt.% CMC have an average size in the small population of 47 nm, while its large population presents a value of 249 nm, with an overall average value of 168.14 nm $\pm$ 134.89 nm. In contrast, the small population of the spheres with 2 wt.% CMC has an average size of 154 nm, and its large population has an average of

671 nm, having as a general average, 523.42 nm ± 331.64 nm. Both samples had conditions of 21.5 kV, 10 cm of distance needle-to-collector, and 0.15 mL/h

The obtention of the previous nano- (<100 nm) and microspheres (>100 nm) of CMC/PVA could be caused by the low flexibility of CMC chains, as well as the presence of too much charge on the jet due to the high applied voltage, provoking repulsive forces that prevent the chain cohesion required for fiber formation. To overcome these challenges, the testing with different solvents and voltages could be performed (Sohofi et al., 2014).

In Figure 25, SEM pictures and distributions of PVA/Ch with a ratio of 3:1 v/v are shown, and the same spherical form of the previous samples can be seen in all attempts. In the Figure 25a, the particles correspond to a sample with PVA 10% / Ch 2%, and present three different populations around 363 nm, 730 nm, and 1729 nm, being the overall average, 723.59 nm ± 616.72 nm. The formation of large populations is more likely to be bubbles from the polymer solution given that its viscosity was very small, preventing even the interaction between the droplet and the electric field.

On the other hand, Figure 25b shows the SEM images and distribution of PVA 10% / Ch 2.5% composites, resulting in the formation of particles with three populations, with averages of 410.55 nm, 691.49 nm, and 1853.20 nm. 892.39 nm ± 708.71 nm. These microspheres are having the same behavior as the previous sample, presenting even larger size populations.

In Figure 25c, the SEM information is related to PVA 10% / Ch 3% composites, which presented a higher viscosity appearance in comparison to the initial PVA 10% solution. The sample appears to have two important populations around 297 nm, and 825.28,

being the first one more impactful, as the overall average size is 432.57 nm ± 305.36 nm. Their behavior can be related to the CMC microspheres, which presented low flexibility and too much charge on the jet.

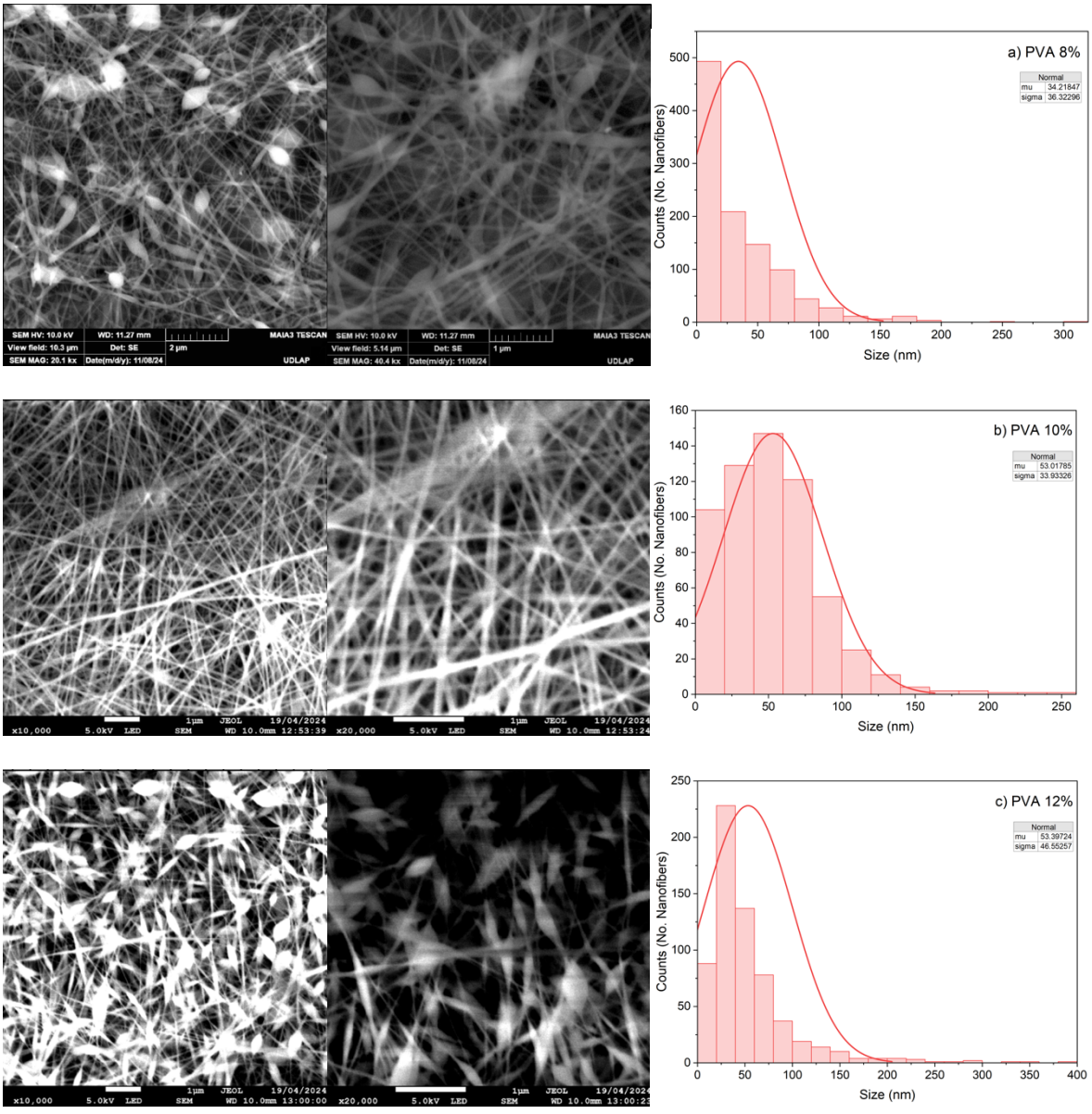

Figure 23. SEM images (at different magnifications) of nanofibers and their size distribution: a) PVA 8%, b) PVA 10%, and c) PVA 12%.

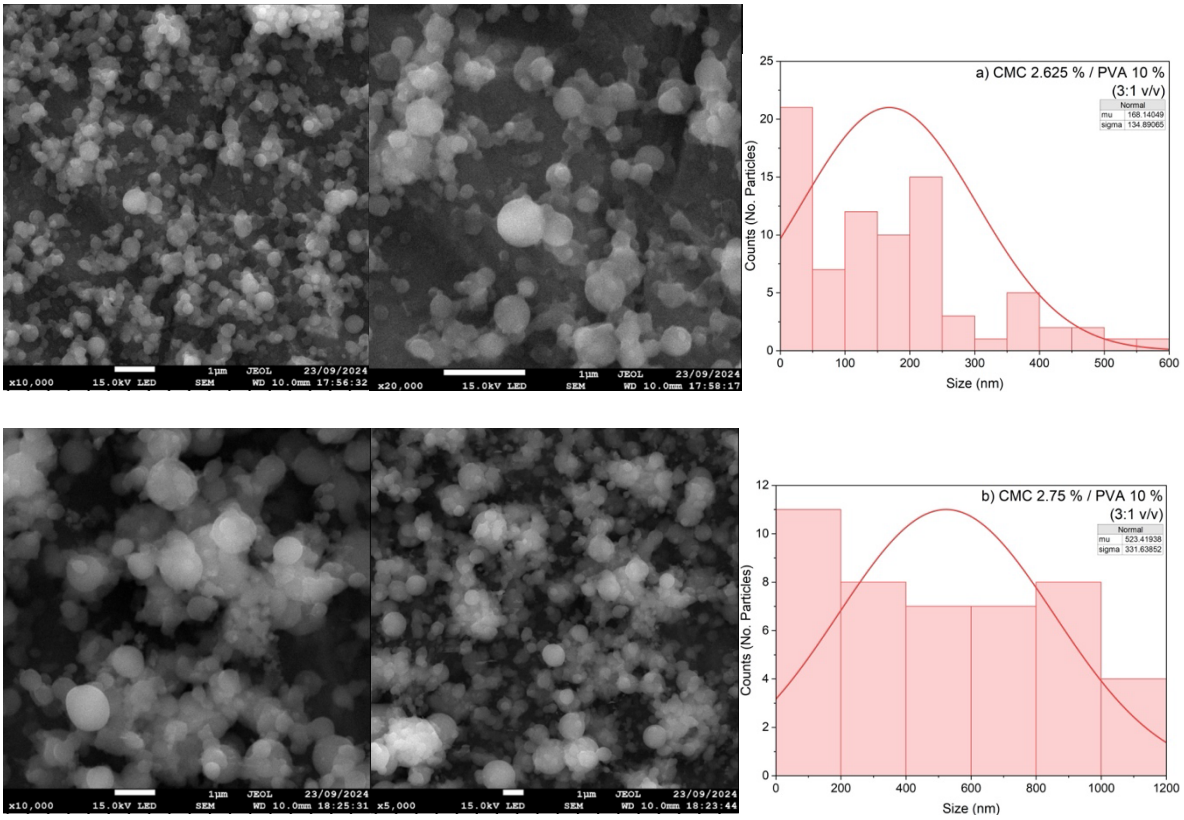

Figure 24. SEM images (at different magnifications) of trial PVA/CMC (1:3 v/v) solutions for electrospinning process and their size distribution: a) 10%/2.625%, b) 10%/2%.

In addition, in Figure 26, the SEM images and size distributions of Ch/PVA (1:3 v/v) nanofibers at different concentrations are presented. In Figure 26a, the formation of non-homogeneous nanofibers with the presence of microbubbles is shown. Interestingly, the nanofibers are also presented inside the bubbles that probably were produced by the action of the high voltage to the jet cone, provoking the presence of repulsive forces in the sample. The size analysis was performed only considering the well-formed nanofibers and the populations inside the microbubbles, resulting in an overall value of 36.65 nm $\pm$ 46.53 nm.

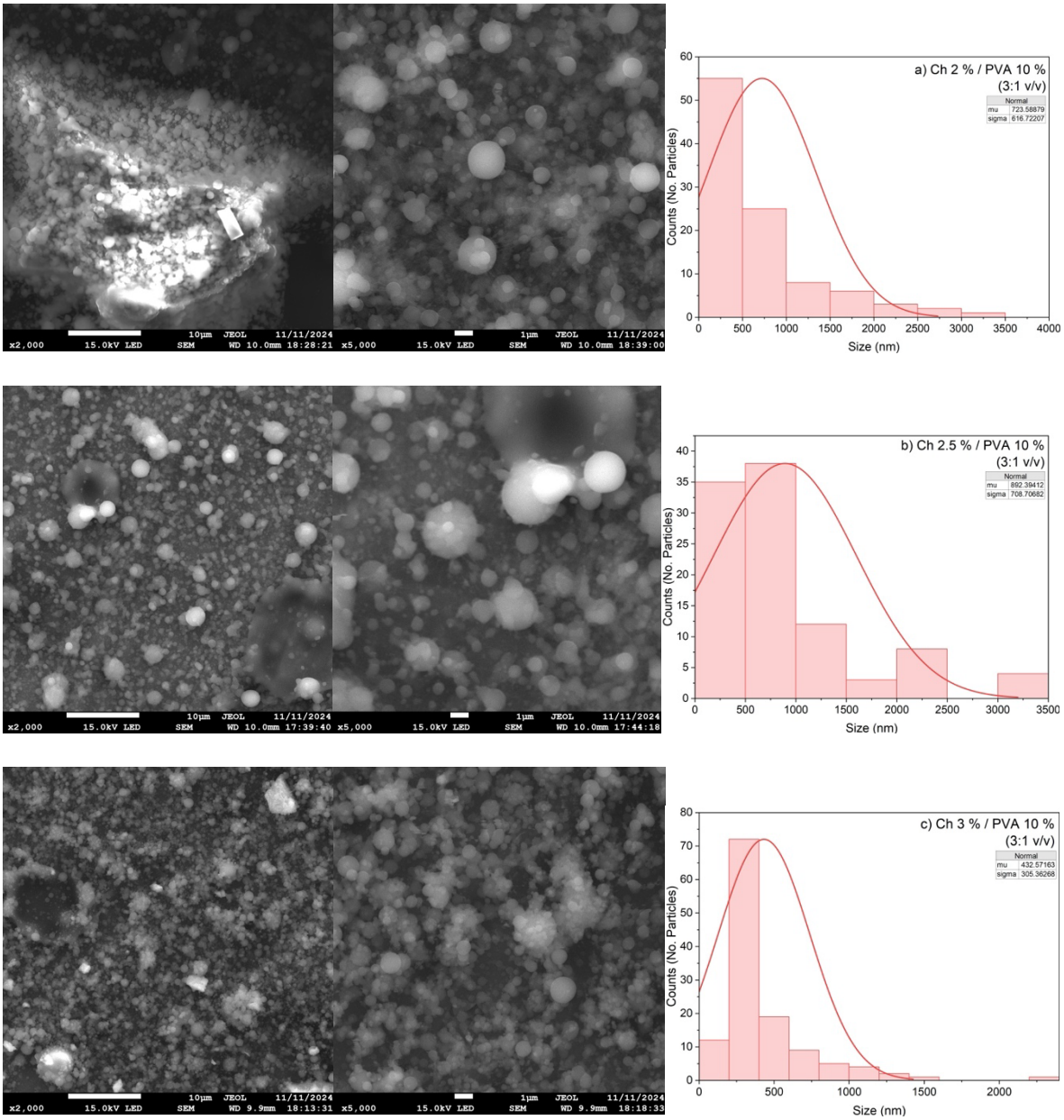

Figure 25. SEM images (at different magnifications) of trial PVA/CMC (1:3 v/v) solutions for electrospinning process and their size distribution: a) 10%/2%, b) 10%/2.5%, c) 10%/3%.

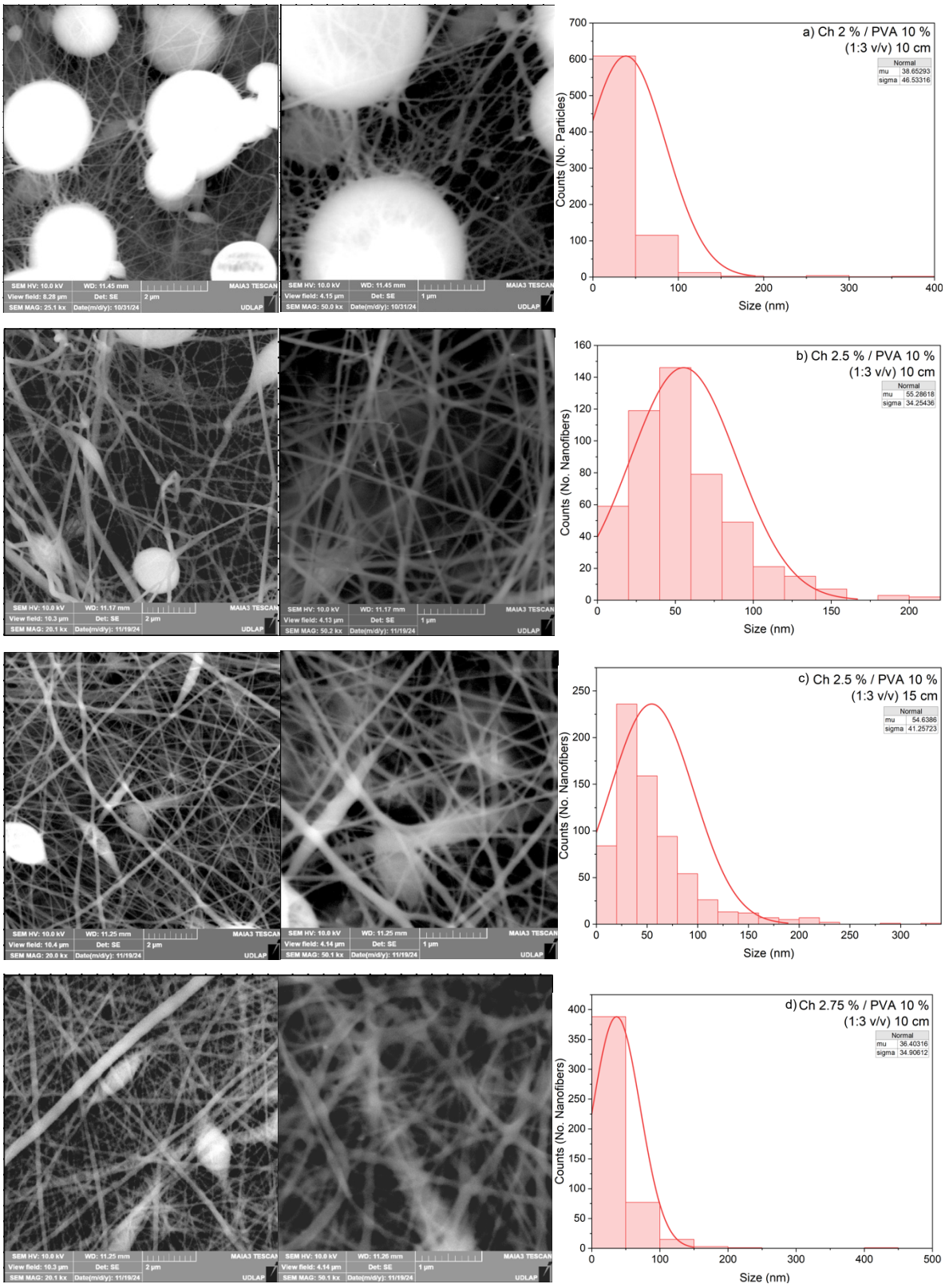

Figure 26 (Part 1).

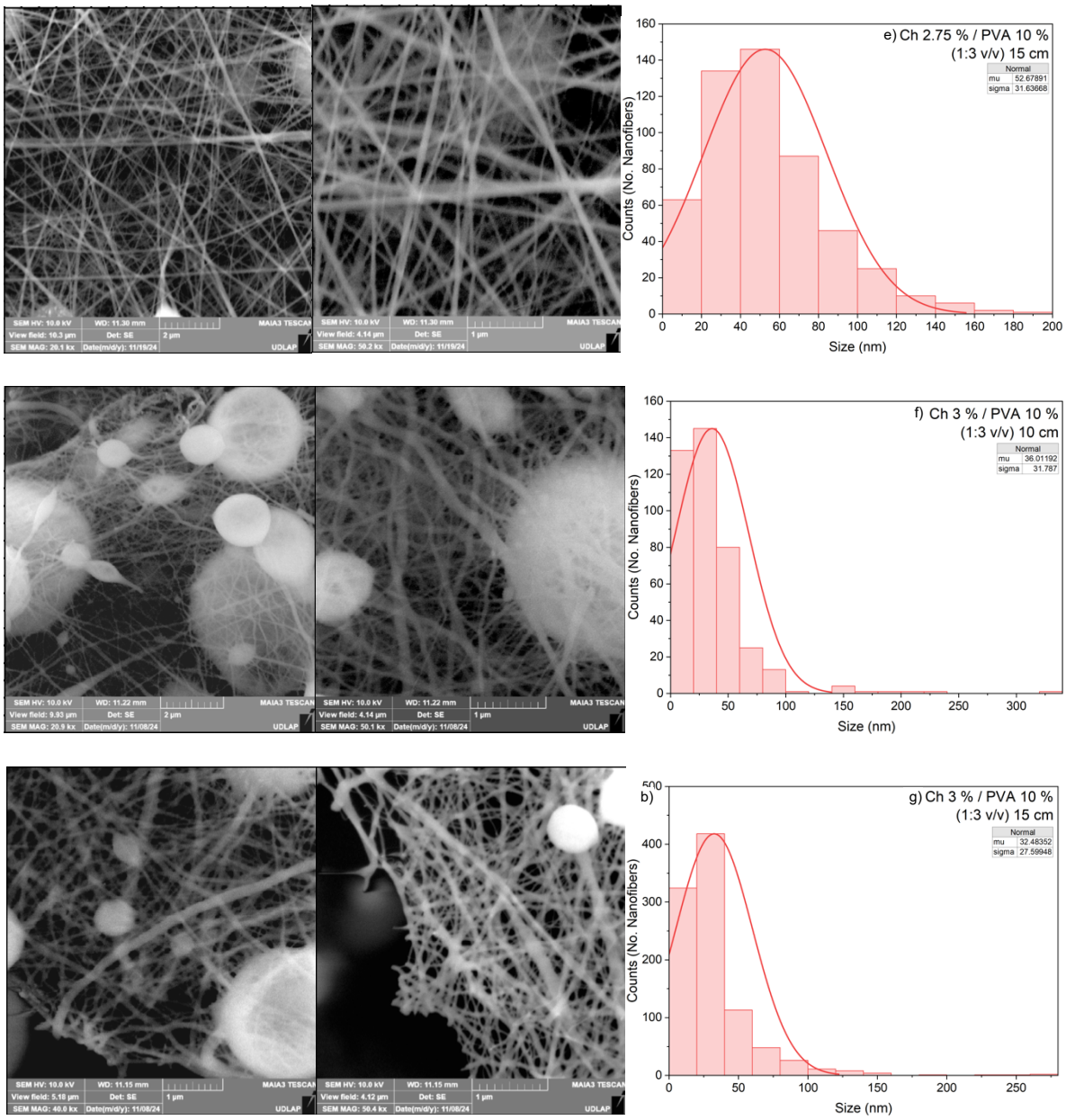

Figure 26 (Part 2). SEM images (with different magnifications) of Ch/PVA (1:3 v/v) nanofibers and their size distribution: a) 2%/10%–10 cm, b) 2.5%/10%–10 cm, c) 2.5%/10%–15cm, d) 2.75%/10%–10 cm, e) 2.75%/10%–15 cm, f) 3%/10%–10 cm, g) 3%/10%–15 cm.

In addition, in Figure 26b, nanofibers with Ch 2.5% / PVA 10% (1:3 v/v) with a tip-to-collector distance of 10 cm during electrospinning can be seen. The presence of a few bubbles could affect the monodispersion of the sample, however, the nanofibers are mostly homogeneous, with an average size of 55.29 nm $\pm$ 34.25 nm. In contrast, the Figure 26c presents the nanofibers with the same concentration values and 15 cm of tip-to-collector distance during electrospinning process. This resulted in the increasement of polydispersity, as the average value resulted in almost the same value, but with the presence of larger fibers that affected the standard deviation, being in this case 54.64 nm $\pm$ 41.26 nm.

In Figure 26d and e, the nanofibers of Ch 2.75% / PVA 10% (1:3 v/v), with 10 cm and 15 cm of tip-to-collector distance, respectively, are presented. The sample with 10 cm distance presented a very small size average of 36.4 nm $\pm$ 34.91 nm. The reason behind this behavior could be related to the tip-to-collector distance, allowing the stretching of the jet cone in a more controlled environment, reducing the travel time before solidification.

For the sample in Figure 26e, the average size increased to 52.68 nm $\pm$ 31.64 nm, as the distance tip-to-collector was higher. The formed nanofibers have better monodispersity in comparison to the previous sample, and beads are not constantly present among the fibers, indicating that this is near the optimal configuration for obtaining smooth and homogeneous nanofibers of chitosan and PVA (1:3 v/v) blend.

For the samples in Figure 26f and 26g, the formation of root-like nanofibers. The size dispersion analysis was performed without considering the bubbles in the samples which are larger than 1 micrometer in almost all cases. For the sample with tip-to-collector distance of

10 cm, the nanofibers average is 36.01 nm ± 31.79 nm with presence of some fibers between 150 and 200 nm.

However, for the sample with 15 cm in distance, the size decreases to 32.48 nm ± 27.60 nm. The latter appears to be cross-linked, but no crosslinking agents have been added to the sample. The qualitative appearance could have been provoked by the fast evaporation of the solvent and the increasement of chitosan concentration. To support this idea, it should be noted that the temperature when performing this electrospinning process was nearly 30°C, consequently increasing the evaporation rate (Park et al., 2010)

In Figure 27, SEM images of two different attempts of encapsulation of ferrite nanoparticles are shown. The one in Figure 27a corresponds to a sample of Ch 2%/PVA 10% (3:1 v/v) with 20 wt.% per polymer weight of ferrite nanoparticles (x=0.25), while the other in Figure 27b is Ch 2%/PVA 10% (1:3 v/v) with 10 wt.% per polymer weight of ferrite nanoparticles (x=0.25). Both resulted in the formation of microbubbles with traces of magnetic nanoparticles inside them, which could indicate that the viscosity of the solution was not the optimal, as well as the concentrations of the components. However, the formation of fiber connectors was achieved in the second sample, which could indicate that further investigation about conformations with PVA/CMC 3:1 v/v could be developed.

In Figure 28, SEM images and size distributions of different attempts for obtaining nanofibers of Ch 2.75% / PVA 10% with $Ni_{1-x}Zn_xFe_2O_4$ nanoparticles inside with electrospinning process were performed. The size distribution estimations do not consider the presence of microbubbles, which are persistent in all the samples. Additionally, the SEM images were further treated with Mountains 8 software to change their contrast, as it is easier

to see the magnetic nanoparticles inside the fibers (they are covered in black when contrast is changed).

Figure 28a presents the information for the sample using MNPs with x=0.25 and a tip-to-collector distance of 15 cm. The fibers have an average size of 53.28 nm ± 55.38 nm, however, the presence of nanoparticles inside the nanofibers is limited, and they appeared to be encapsulated in beads between the fibers. The EDX of the sample confirmed that the ferrite nanoparticles are present in the sample, however, is not possible identify the content, as the atomic percentages are very low (below 1%).

It should be mentioned that it could exist a certain quantity of nanoparticles inside the nanofibers that it is not possible to see using only SEM. A better analysis could be done by analyzing the samples with STEM or TEM techniques, as they give better contrast between organic material and metallic compounds.

In the remain nanofibers with magnetic nanoparticles interaction, the SEM images showed a smaller quantity of nanofibers to analyze, given that the collection time was reduced to only 15 min per sample at 0.5 mL/h for deadline purposes. Then, Figure 28b and c present data of nanofibers including MNPs with x=0.5 and tip-to-collector distances of 10 and 15 cm, respectively, are proposed. The average size of nanofibers in the first sample resulted in 43.52 nm ± 34.21 nm. According to the reversed-contrast SEM images, the magnetic nanoparticles uptake was decreased considerably.

When using 15 cm of tip-to-collector distance, the nanofibers size average increased to 48.11 nm ± 34.73 nm, however, the sample is not homogeneous. When analyzing the reverse-contrast images, magnetic nanoparticles can be seen in adhesion to the surface and

inside of some nanofibers, however, the presence is lower in comparison to the sample with x=0.25 MNPs (NZ75).

For Figures 28d and e, it can be seen the SEM-EDX data and distributions of nanofibers with x=0.75 of MNPs using 10 cm and 15 cm of tip-to-collector distance, respectively. The formation of nanofibers seemed to be more homogenous in both cases, and the presence of ferrite nanoparticles is confirmed by the EDX analysis and the reverse-contrast SEM images.

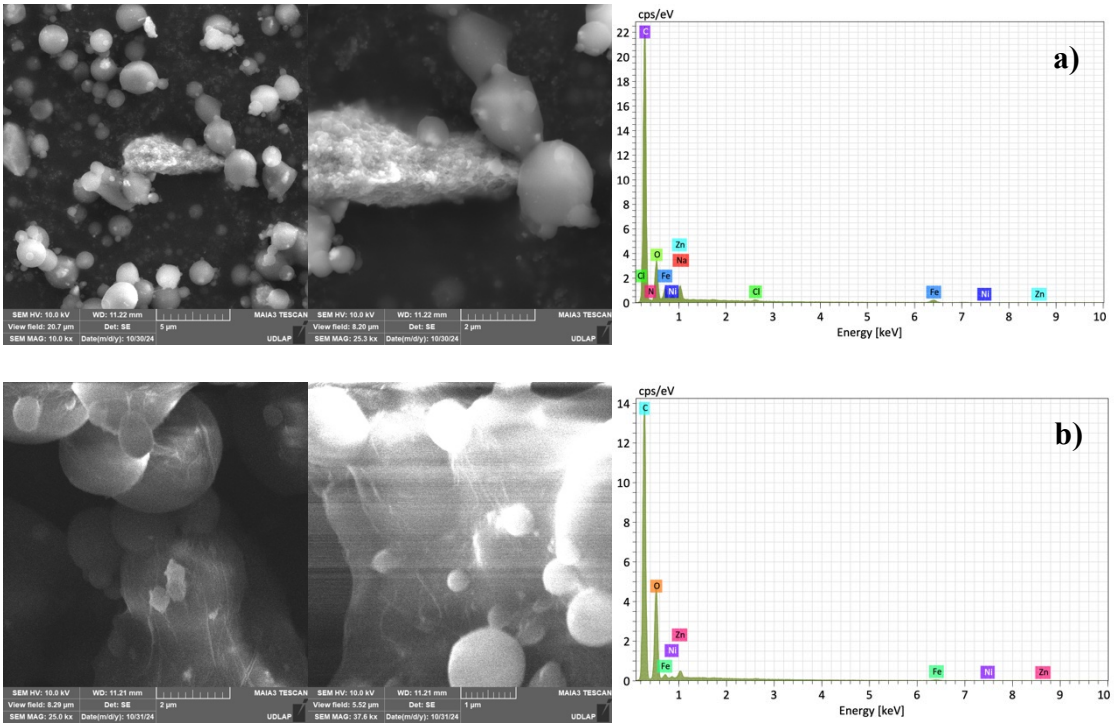

Figure 27. SEM images (different magnifications) and EDX analysis of a) Ch/PVA 2%/10% (3:1 v/v) with 20 wt.% per polymer weight of ferrite nanoparticles (x=0.25), and b) Ch/PVA 2%/10% (1:3 v/v) with 10 wt.% per polymer weight of ferrite nanoparticles (x=0.25).

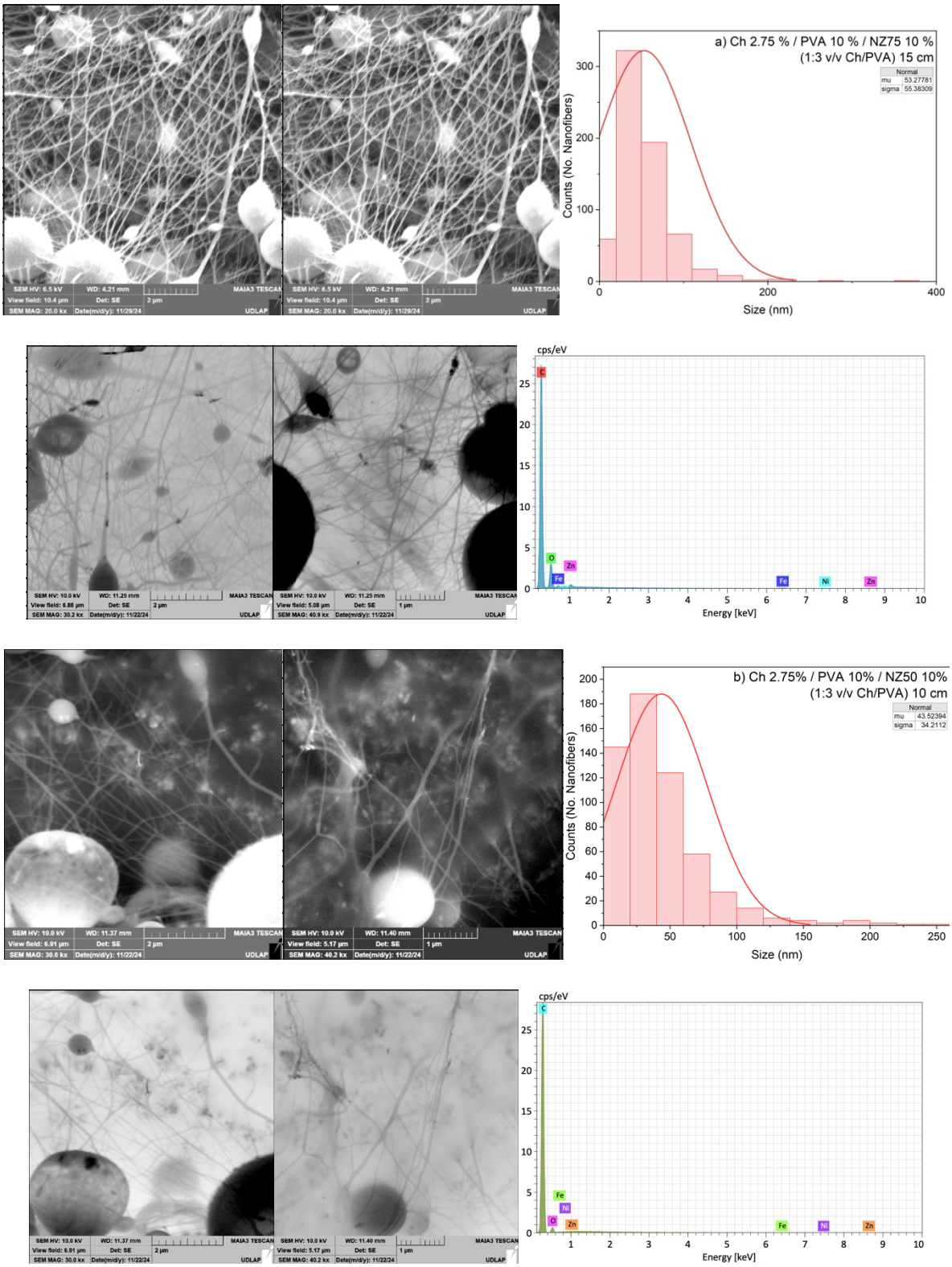

Figure 28 (Part 1).

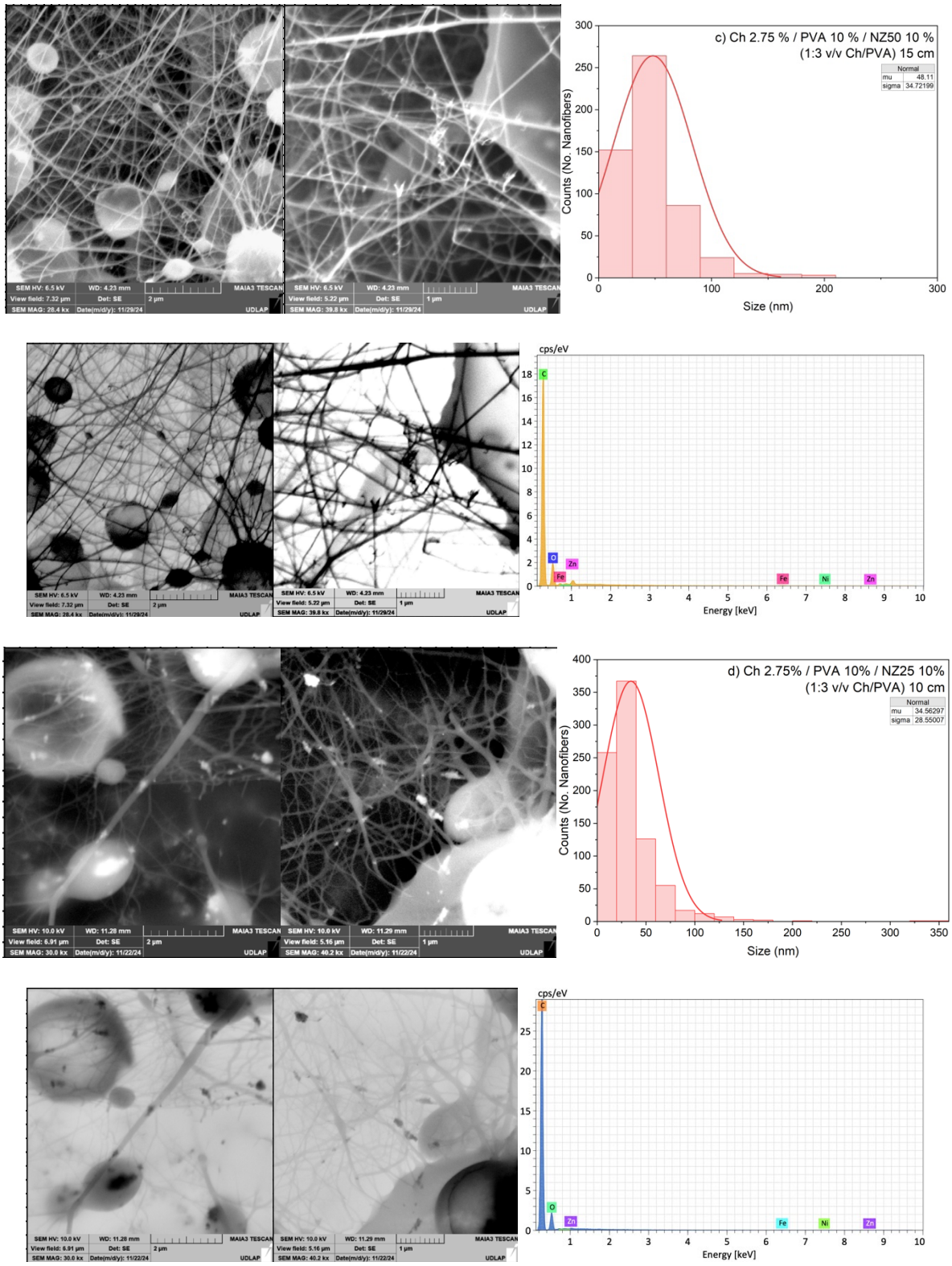

Figure 28 (Part 2).

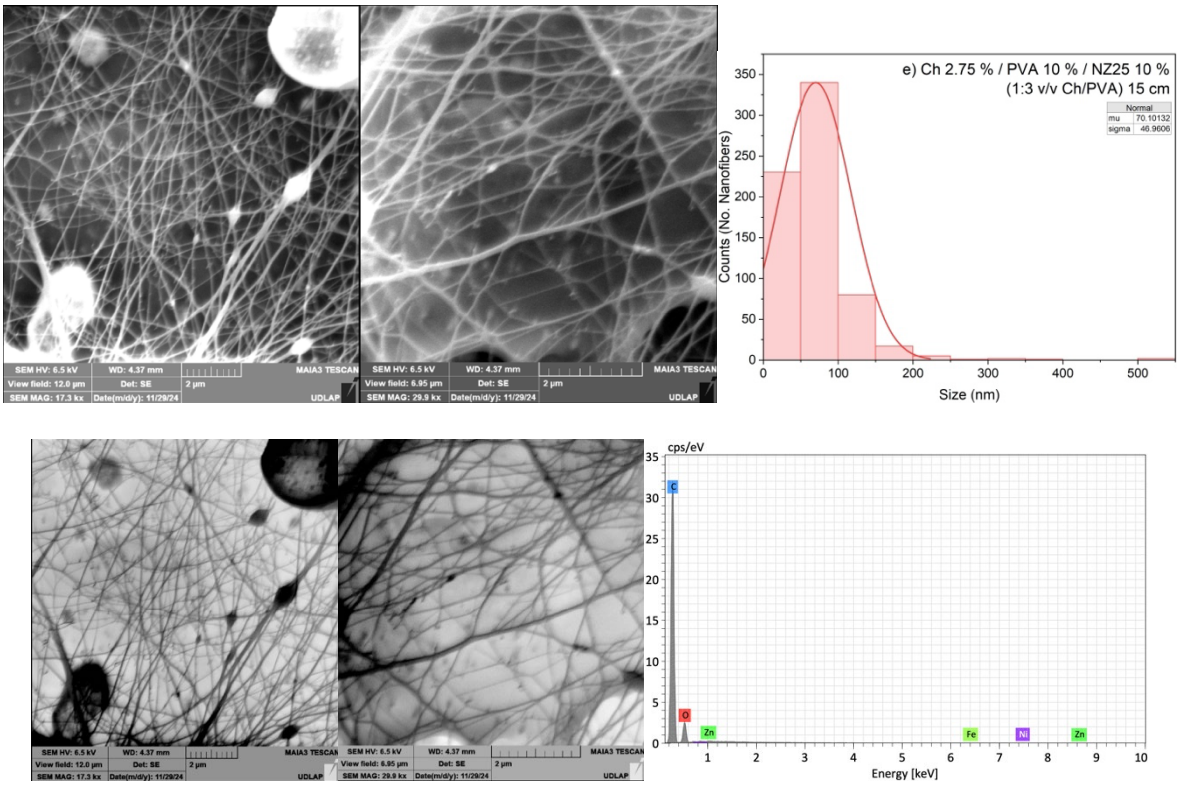

Figure 28 (Part 3). SEM images (with different magnifications and inverse contrast for better magnetic ferrite NPs visualization) of Ch 2.75% / PVA 10% (1:3 v/v) nanofibers with $Ni_{1-x}Zn_xFe_2O_4$ and their size distribution: a) x=0.25–15 cm, b) x=0.5–10 cm, c) x=05–15cm, d) x=0.75–10 cm, e) x=0.75–15 cm.

Specifically, in the Figure 28d, with the SEM size distribution analysis it was estimated that the average size value is 34.56 nm $\pm$ 28.55 nm. While the mean size value for the second trial is 70.01 nm $\pm$ 46.96 nm, having almost two times the value of the first trial. Additionally, the morphology of the sample synthesized with 15 cm of tip-to-collector distance seems to be optimal, presenting almost homogeneous nanofibers with presence of some bubbles.

Finally, as a preview of research in development, in Figure 29, SEM images and their respective size distributions are shown, corresponding to the testing process being carried to

obtain homogeneous and smooth core-shell nanofibers with PVA/Ch/MNPs as core and PCL as polymeric shell. In the case of samples in Figure 29a and b, PCL 5% nanofibers are presented. In the first one, the distance tip-to-collector is 10 cm, and the nanofibers presented an average size of 84.88 nm ±146.68 nm. The sample is not homogeneous and show a wave shape in all its morphology.

When increasing the distance to collector to 15 cm, the fibers almost lose the wave shape and reduce their average size to 46.56 nm ± 118.77 nm. Having still polydispersity, the nanofibers look more homogeneous and smoother in their shape, what could indicate that the small distance to collector was affecting the formation of nanofibers as the jet was instable and the solvent could be evaporating considerably fast.

In Figures 29c and d, the first attempts for obtaining the core-shell nanofibers using Ch/PVA@PCL were performed. The first trial had concentrations of 2.75%/10%@5% and a tip-to-collector distance of 10 cm, while the second was done with 15 cm. In theory, as they are including the different components that have been reviewed previously in this report, the value of their average size should increase.

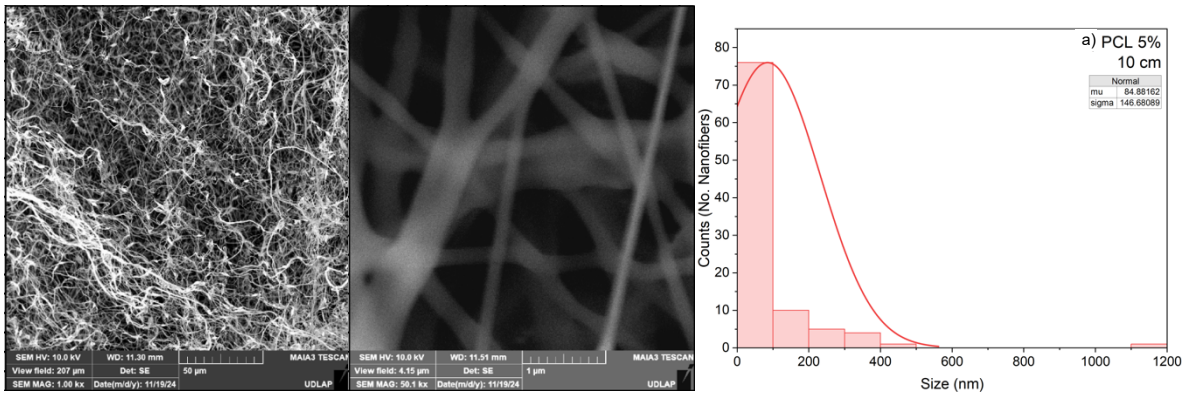

Figure 29 (Part 1).

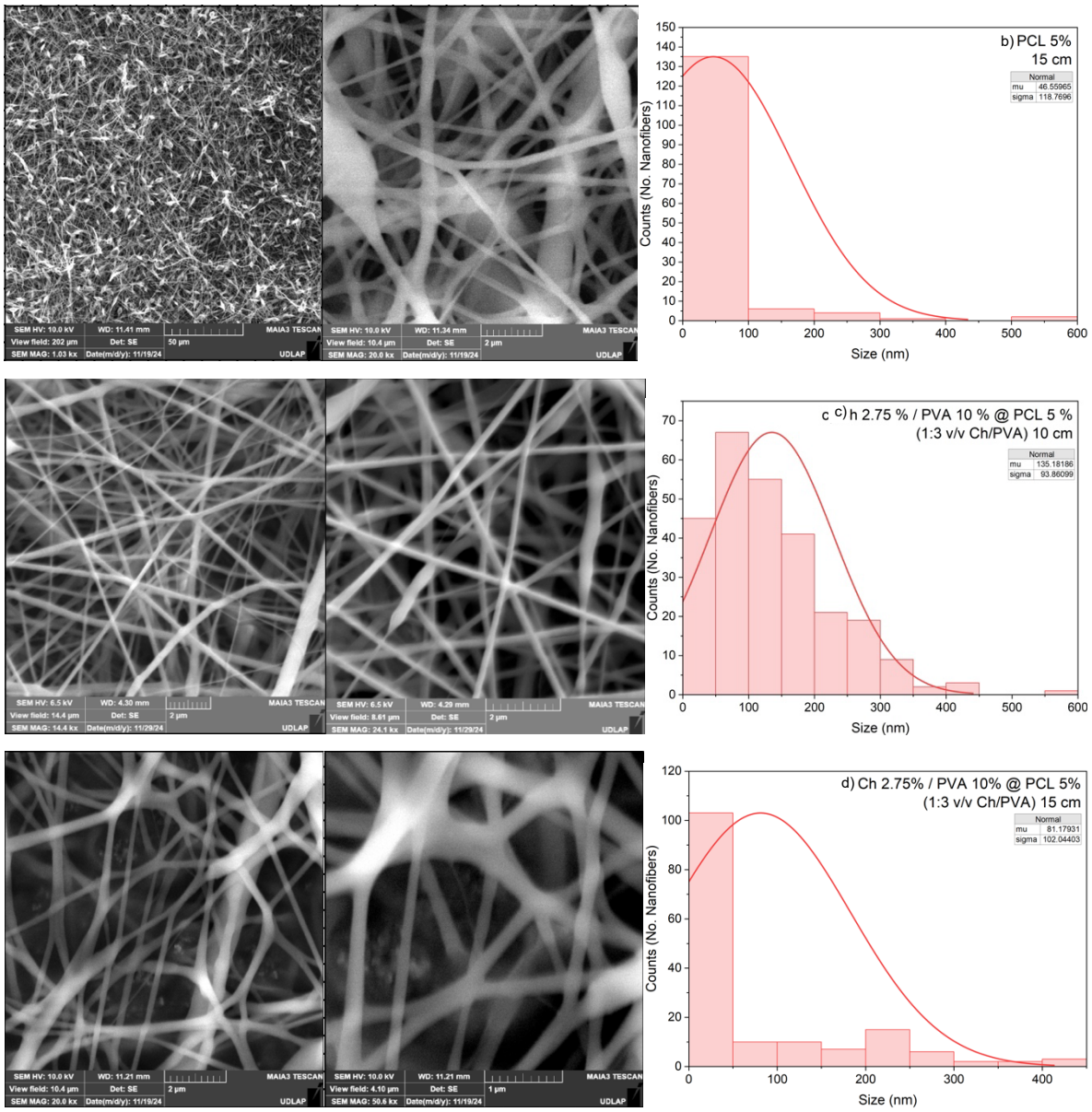

Figure 29 (Part 2). SEM images (at different magnifications) of PCL shell and core-shell nanofibers and their size distribution: a) PCL 5%–10 cm, b) PCL 5%-15 cm, c) Ch 2.75% / PVA 10% @ PCL 5%–10 cm, d) Ch 2.75% / PVA 10% @ PCL 5%–15 cm.

As expected, the calculated means are larger than the values obtained for the core nanofibers. Specifically, the average size of the first trial is 135.18 nm ± 93.86 nm, while the value for the second trial is 81.18 nm ± 102.04 nm. Then, it can be determined that the size value of

the core-shell nanofibers can decrease when the tip-to-collector distance increase, however, it could be possible that the measurement of the second trial is not completely accurate.

7. Conclusions and Recommendations

In this work, a system of $Ni_{1-x}Zn_xFe_2O_4$ nanoparticles was presented with the Zn^{2+} ion content as a variable x=0, 0.25, 0.5, 0.75. These nanomaterials were synthesized by chemical co-precipitation and sintered at 1000°C to improve their magnetic properties. They were physiochemically characterized in depth about their crystalline structure and size dispersion, resulting in their analysis by XRD, SEM, EDX, Raman, FTIR, and magnetic hyperthermia studies.

Specifically, the ferrite nanoparticles resulted in the formation of crystalline structures with sizes below 20 nm (favoring their magnetic characteristics as they are more likely to be superparamagnetic), except for the sample x=0.25, which presented sizes around 25-28 nm. These parameters were confirmed by the XRD patterns, from which was possible to make W-H plots and Lorentzian fits to present valuable information about the crystallite size of all samples.

From the previous studies, it was possible to determinate that the x=0 sample synthesized was amorphous, while the x=0.25 presented secondary phases corresponding to hematite and nickel oxide. These were presumed to be surface impurities, as they were further removed by the treatment with an acidic solution, which allows the ferrite nanoparticles to show better crystallinity without any peaks corresponding to additional impurities.

Ferrite nanoparticles before acidic treatment were also characterized in terms of functional groups by FTIR and Raman analysis, showing complete cohesion with the

literature reports. Furthermore, SEM and EDX studies were also discussed, resulting in the screening of very small magnetic nanoparticles with high surface tension that resulted in the agglomeration of all samples. EDX data provided the required information for estimating the value of important lattice parameters, such as the radii of A- and B-sites in the spinel cubic structure, giving an insight of the molecular interaction within the samples, as they resulted to be in compressive strain.

DLS studies were performed to confirm that ferrite nanoparticles increased their stability when they were treated with an acidic solution in comparison to be previous samples, which were only calcined (possible reason for formation of secondary phases in x=0.25). Additionally, XRD, SEM and EDX studies were also done for the ferrite system after the acidic treatment to discuss the changes in crystallinity, sizes, lattice arrangements, strain, X-ray density, radii of A- and B-sites, morphology and compositions.

Previous information was relevant to explain the performance of the synthesized ferrite nanoparticles for magnetic hyperthermia. Before the acidic process took place, x=0.25 sample presented a remarkable heating performance, increasing almost 30°C in 300 s with a calculated SAR value of 28.35 W/g. In this case, the zinc content increasement resulted in the diminution of magnetic hyperthermia performance and characteristics.

However, after the treatment with acidic solution, the sample with the highest performance was x=0.75, being the one containing more Zn^{2+}, being confirmed by the EDX spectrum, having as a possible reason of this situation the rearrangement of the lattice parameters.

Finally, a series of PVA, PVA/CMC, PVA/Ch, and PVA/Ch/ferrite nanoparticles solutions were used as trials for the obtention of homogeneous nanofibers. Several reasons

about the possible constrains in the methodology that prevented the formation of homogeneous nanofibers are discussed by analyzing them using SEM and EDX. However, the objective of obtaining core/shell nanofibers with chitosan/PVA/ferrite nanoparticles as a core and polycaprolactone as a shell, is still in progress, and it is intended to be developed in future research.

8. Bibliography

Abreu, F. R. de, & Campana-Filho, S. P. (2005). Preparation and characterization of carboxymethylchitosan. *Polímeros*, *15*, 79–83. https://doi.org/10.1590/S0104-14282005000200004

Acklin, B., & Lautens, E. (2012). *Magnetic Nanoparticles: Properties, Synthesis and Applications*. Nova Science Publishers, Inc. https://research.ebsco.com/linkprocessor/plink?id=2ce26fa7-24be-31ad-b81d-db1d7fbe166f

Ahmadi Bonakdar, M., & Rodrigue, D. (2024). Electrospinning: Processes, Structures, and Materials. *Macromol*, *4*(1), Article 1. https://doi.org/10.3390/macromol4010004

Akbarzadeh, A., Samiei, M., & Davaran, S. (2012). Magnetic nanoparticles: Preparation, physical properties, and applications in biomedicine. *Nanoscale Research Letters*, *7*(1), 144. https://doi.org/10.1186/1556-276X-7-144

Aliyeva, S., Babayev, S., & Mehdiyev, T. (2017). Raman spectra of Ni 1-X Zn X Fe 2 O 4 nanopowders. *Journal of Raman Spectroscopy*, *49*. https://doi.org/10.1002/jrs.5276

Arteaga-Cardona, F., Santillán-Urquiza, E., Pal, U., Méndoza-Álvarez, M. E., Torres-Duarte, C., Cherr, G. N., de la Presa, P., & Méndez-Rojas, M. Á. (2017). Unusual variation

of blocking temperature in bi-magnetic nanoparticles. *Journal of Magnetism and Magnetic Materials*, *441*, 417–423. https://doi.org/10.1016/j.jmmm.2017.06.024

Asefa, T., & Dubovoy, V. (2016). Ordered Mesoporous/Nanoporous Inorganic Materials via Self-Assembly. In *Reference Module in Chemistry, Molecular Sciences and Chemical Engineering*. https://doi.org/10.1016/B978-0-12-409547-2.12649-6

Assa, F., Jafarizadeh-Malmiri, H., Ajamein, H., Vaghari, H., Anarjan, N., Ahmadi, O., & Berenjian, A. (2017). Chitosan magnetic nanoparticles for drug delivery systems. *Critical Reviews in Biotechnology*, *37*(4), 492–509. https://doi.org/10.1080/07388551.2016.1185389

Barbosa, M. A., Pêgo, A. P., & Amaral, I. F. (2011). 2.213—Chitosan. In P. Ducheyne (Ed.), *Comprehensive Biomaterials* (pp. 221–237). Elsevier. https://doi.org/10.1016/B978-0-08-055294-1.00072-6

Barrera, G., Coïsson, M., Celegato, F., Olivetti, E. S., Martino, L., Miletto, I., & Tiberto, P. (2018). Magnetic and Thermal Characterization of Core-Shell Fe-Oxide@SiO2 Nanoparticles for Hyperthermia Applications. *IEEE Journal of Electromagnetics, RF and Microwaves in Medicine and Biology*, *2*(4), 257–261. IEEE Journal of Electromagnetics, RF and Microwaves in Medicine and Biology. https://doi.org/10.1109/JERM.2018.2869197

Basha, B., Shakir, I., Alrowaili, Z. A., Al-Buriahi, M. S., Anwar, M., Yousaf, S., & Warsi, M. F. (2024). WO3–NiO/rGO Based Photocatalyst for Effectively Degradation of Colored and Colorless Pollutants Using Solar Light Irradiation. *Journal of Inorganic and Organometallic Polymers and Materials*, *34*(6), 2635–2646. https://doi.org/10.1007/s10904-024-03001-x

Bhattacharya, S. (2021). Chapter 4—Nanostructures in gene delivery. In A. K. Bajpai & R. K. Saini (Eds.), *Advances in Polymeric Nanomaterials for Biomedical Applications* (pp. 101–135). Elsevier. https://doi.org/10.1016/B978-0-12-814657-6.00007-0

Binandeh, M., Karimi, F., & Rostamnia, S. (2021). Application of magnetic nanoparticles by comparing the absorbance and stabilization of biomolecules DNA-C, L by the electrophoretic detection. *International Journal of Health Sciences*, *15*(2), 3–8.

Brennan, G., Bergamino, S., Pescio, M., Tofail, S. A. M., & Silien, C. (2020). The Effects of a Varied Gold Shell Thickness on Iron Oxide Nanoparticle Cores in Magnetic Manipulation, T1 and T2 MRI Contrasting, and Magnetic Hyperthermia. *Nanomaterials*, *10*(12), Article 12. https://doi.org/10.3390/nano10122424

Chandraprasad, M. S., Dey, A., & Swamy, M. K. (2022). 1—Introduction to cancer and treatment approaches. In M. K. Swamy, T. Pullaiah, & Z.-S. Chen (Eds.), *Paclitaxel* (pp. 1–27). Academic Press. https://doi.org/10.1016/B978-0-323-90951-8.00010-2

Chen, S.-C., Wu, Y.-C., Mi, F.-L., Lin, Y.-H., Yu, L.-C., & Sung, H.-W. (2004). A novel pH-sensitive hydrogel composed of N,O-carboxymethyl chitosan and alginate cross-linked by genipin for protein drug delivery. *Journal of Controlled Release*, *96*(2), 285–300. https://doi.org/10.1016/j.jconrel.2004.02.002

Chiozzi, V., & Rossi, F. (2020). Inorganic–organic core/shell nanoparticles: Progress and applications. *Nanoscale Advances*, *2*(11), 5090–5105. https://doi.org/10.1039/D0NA00411A

Chireh, M., Naseri, M., & Kamalianfar, A. (2020). 57Fe Mossbauer spectroscopy investigation of NiFe2O4 and MnFe2O4 ferrite nanoparticles prepared by thermal treatment method. *Applied Physics A: Materials Science & Processing*, *126*(7), 1–6.

https://doi.org/10.1007/s00339-020-03716-x

Chitra Devi, E., & Singh, S. (2021). Tracing the Magnetization Curves: A Review on Their Importance, Strategy, and Outcomes. *Journal of Superconductivity and Novel Magnetism*. https://doi.org/10.1007/s10948-020-05733-6

Colobatiu, L., Gavrilas, L., & Mocan, A. (2021). Chapter 10 - Natural compounds as chemosensitizers: A lesson from plants. In C. T. Supuran & S. Carradori (Eds.), *pH-Interfering Agents as Chemosensitizers in Cancer Therapy* (Vol. 10, pp. 147–165). Academic Press. https://doi.org/10.1016/B978-0-12-820701-7.00009-9

Costa, A. C. F. M., Diniz, A. P., Silva, V. J., Kiminami, R. H. G. A., Cornejo, D., Gama, A. M., Rezende, M. C., & Gama, L. (2009). Influence of calcination temperature on the morphology and magnetic properties of Ni–Zn ferrite applied as an electromagnetic energy absorber. *Journal of Alloys and Compounds*, *483*, 563–565. https://doi.org/10.1016/j.jallcom.2008.08.108

Doshi, B., Ayati, A., Tanhaei, B., Repo, E., & Sillanpää, M. (2018). Partially carboxymethylated and partially cross-linked surface of chitosan versus the adsorptive removal of dyes and divalent metal ions. *Carbohydrate Polymers*, *197*, 586–597. https://doi.org/10.1016/j.carbpol.2018.06.032

Ehi-Eromosele, C., Ita, B., Iweala, E., Adalikwu, S., & Anawe, P. (2015). Magneto-structural properties of Ni-Zn nanoferrites synthesized by the low-temperature auto-combustion method. *Bulletin of Materials Science*, *38*, 1465–1472. https://doi.org/10.1007/s12034-015-1038-1

Fabris, F., Lohr, J. H., Lima, E., de Almeida, A. A., Troiani, H., Rodríguez, L. M., Vásquez Mansilla, M., Aguirre, M., Goya, G. F., Rinaldi, D., Ghirri, A., Peddis, D., Fiorani,

D., Zysler, R. D., De Biasi, E., & Winkler, E. (2020). Adjusting the Néel relaxation time of Fe3O4/ZnxCo1-xFe2O4 core/shell nanoparticles for optimal heat generation in magnetic hyperthermia. *Nanotechnology*. https://doi.org/10.1088/1361-6528/abc386

Fernandes Queiroz, M., Melo, K. R. T., Sabry, D. A., Sassaki, G. L., & Rocha, H. A. O. (2015). Does the Use of Chitosan Contribute to Oxalate Kidney Stone Formation? *Marine Drugs*, *13*(1), Article 1. https://doi.org/10.3390/md13010141

Ghosh Chaudhuri, R., & Paria, S. (2012). Core/Shell Nanoparticles: Classes, Properties, Synthesis Mechanisms, Characterization, and Applications. *Chemical Reviews*, *112*(4), 2373–2433. https://doi.org/10.1021/cr100449n

Gupta, S., & Tripathi, M. (2012). A review on the synthesis of TiO2 nanoparticles by solution route. *Open Chemistry*, *10*(2), 279–294. https://doi.org/10.2478/s11532-011-0155-y

Hammad, M., Nica, V., & Hempelmann, R. (2016). Synthesis and Characterization of Bi-Magnetic Core/Shell Nanoparticles for Hyperthermia Applications. *IEEE Transactions on Magnetics*, *PP*, 1–1. https://doi.org/10.1109/TMAG.2016.2635696

Hanahan, D. (2022). Hallmarks of Cancer: New Dimensions. *Cancer Discovery*, *12*(1), 31–46. https://doi.org/10.1158/2159-8290.CD-21-1059

Hanahan, D., & Weinberg, R. A. (2000). The hallmarks of cancer. *Cell*, *100*(1), 57–70. https://doi.org/10.1016/s0092-8674(00)81683-9

Hanahan, D., & Weinberg, R. A. (2011). Hallmarks of cancer: The next generation. *Cell*, *144*(5), 646–674. https://doi.org/10.1016/j.cell.2011.02.013

Heuver, J. A., Scaramucci, A., Blickenstorfer, Y., Matzen, S., Spaldin, N. A., Ederer, C., & Noheda, B. (2015). Strain-induced magnetic anisotropy in epitaxial thin films of the

spinel CoCr2O4. *Physical Review B*, *92*, 214429. https://doi.org/10.1103/PhysRevB.92.214429

Hwang, J., Choi, M., Shin, H.-S., Ju, B.-K., & Chun, M. (2020). Structural and Magnetic Properties of NiZn Ferrite Nanoparticles Synthesized by a Thermal Decomposition Method. *Applied Sciences*, *10*(18), Article 18. https://doi.org/10.3390/app10186279

Iglesias, S. P., Arias-Durán, A., Yañez-Limón, J. M., Ramirez-Bon, R., Hurtado-Macias, A., Arnache, O., Gómez, M. E., Lopera, W., & Zambrano, G. (2019). Effect of Zn Concentration on the Structure, Morphology, and Magnetic Behavior of Ni1 − xZnxFe2O4 Ferrofluid. *Journal of Superconductivity and Novel Magnetism*, *32*(7), 2199–2208. https://doi.org/10.1007/s10948-018-4950-y

Imran, M., Ansari, A. R., Shaik, A. H., Abdulaziz, Hussain, S., Khan, A., & Chandan, M. R. (2018). Ferrofluid synthesis using oleic acid coated Fe3O4 nanoparticles dispersed in mineral oil for heat transfer applications. *Materials Research Express*, *5*(3), 036108. https://doi.org/10.1088/2053-1591/aab4d7

Issa, B., Obaidat, I. M., Albiss, B. A., & Haik, Y. (2013). Magnetic Nanoparticles: Surface Effects and Properties Related to Biomedicine Applications. *International Journal of Molecular Sciences*, *14*(11), Article 11. https://doi.org/10.3390/ijms141121266

Jafari, A., Pilban Jahromi, S., Boustani, K., Goh, B. T., & Huang, N. M. (2019). Evolution of structural and magnetic properties of nickel oxide nanoparticles: Influence of annealing ambient and temperature. *Journal of Magnetism and Magnetic Materials*, *469*, 383–390. https://doi.org/10.1016/j.jmmm.2018.08.005

Jean-Pierre, P., & McDonald, B. C. (2016). Chapter 17—Neuroepidemiology of cancer and treatment-related neurocognitive dysfunction in adult-onset cancer patients and

survivors. In M. J. Aminoff, F. Boller, & D. F. Swaab (Eds.), *Handbook of Clinical Neurology* (Vol. 138, pp. 297–309). Elsevier. https://doi.org/10.1016/B978-0-12-802973-2.00017-3

Kemp, J. A., & Kwon, Y. J. (2021). Cancer nanotechnology: Current status and perspectives. *Nano Convergence*, *8*(1), 34. https://doi.org/10.1186/s40580-021-00282-7

Kesse, X., Adam, A., Begin-Colin, S., Mertz, D., Larquet, E., Gacoin, T., Maurin, I., Vichery, C., & Nedelec, J.-M. (2020). Elaboration of Superparamagnetic and Bioactive Multicore–Shell Nanoparticles (γ-Fe2O3@SiO2-CaO): A Promising Material for Bone Cancer Treatment. *ACS Applied Materials & Interfaces*, *12*(42), 47820–47830. https://doi.org/10.1021/acsami.0c12769

Kharisov, B. I., Dias, H. V. R., & Kharissova, O. V. (2019). Mini-review: Ferrite nanoparticles in the catalysis. *Arabian Journal of Chemistry*, *12*(7), 1234–1246. https://doi.org/10.1016/j.arabjc.2014.10.049

Kharisov, B. I., Dias, H. V. R., Kharissova, O. V., Jiménez-Pérez, V. M., Pérez, B. O., & Flores, B. M. (2012). Iron-containing nanomaterials: Synthesis, properties, and environmental applications. *RSC Advances*, *2*(25), 9325–9358. https://doi.org/10.1039/C2RA20812A

Kim, B. G., Dong, S. L., & Park, S. D. (2001). Effects of thermal processing on thermal expansion coefficient of a 50 vol.% SiCp/Al composite. *Materials Chemistry and Physics*, *72*(1), 42–47. https://doi.org/10.1016/S0254-0584(01)00306-6

Kim, J.-E., Shin, J.-Y., & Cho, M.-H. (2012). Magnetic nanoparticles: An update of application for drug delivery and possible toxic effects. *Archives of Toxicology*, *86*(5), 685–700. https://doi.org/10.1007/s00204-011-0773-3

Klomp, S., Walker, C., Christiansen, M., Newbold, B., Griner, D., Cai, Y., Minson, P., Farrer, J., Smith, S., Campbell, B. J., Harrison, R. G., & Chesnel, K. (2020). Size-Dependent Crystalline and Magnetic Properties of 5–100 nm Fe $_3$ O $_4$ Nanoparticles: Superparamagnetism, Verwey Transition, and FeO–Fe $_3$ O $_4$ Core–Shell Formation. *IEEE Transactions on Magnetics*, *56*(11), 1–9. IEEE Transactions on Magnetics. https://doi.org/10.1109/TMAG.2020.3018154

Kmita, A., Żukrowski, J., Kuciakowski, J., Marciszko-Wiąckowska, M., Żywczak, A., Lachowicz, D., Gajewska, M., & Sikora, M. (2021). Effect of Thermal Treatment at Inert Atmosphere on Structural and Magnetic Properties of Non-stoichiometric Zinc Ferrite Nanoparticles. *Metallurgical and Materials Transactions A*, *52*(5), 1632–1648. https://doi.org/10.1007/s11661-021-06154-3

Kurian, M., & Thankachan, S. (2021). Structural diversity and applications of spinel ferrite core—Shell nanostructures- A review. *Open Ceramics*, *8*, 100179. https://doi.org/10.1016/j.oceram.2021.100179

Kush, P., Kumar, P., Singh, R., & Kaushik, A. (2021). Aspects of high-performance and bio-acceptable magnetic nanoparticles for biomedical application. *Asian Journal of Pharmaceutical Sciences*, *16*(6), 704–737. https://doi.org/10.1016/j.ajps.2021.05.005

Laurent, S., Forge, D., Port, M., Roch, A., Robic, C., Vander Elst, L., & Muller, R. N. (2008). Magnetic Iron Oxide Nanoparticles: Synthesis, Stabilization, Vectorization, Physicochemical Characterizations, and Biological Applications. *Chemical Reviews*, *108*(6), 2064–2110. https://doi.org/10.1021/cr068445e

Licciulli, S. (2022, January 21). New Dimensions in Cancer Biology: Updated Hallmarks of Cancer Published. *American Association for Cancer Research (AACR)*.

https://www.aacr.org/blog/2022/01/21/new-dimensions-in-cancer-biology-updated-hallmarks-of-cancer-published/

Lim, J., Yeap, S. P., Che, H. X., & Low, S. C. (2013). Characterization of magnetic nanoparticle by dynamic light scattering. *Nanoscale Research Letters*, *8*(1), 381. https://doi.org/10.1186/1556-276X-8-381

Lin, S., & Popp, R. K. (1984). Solubility and complexing of Ni in the system NiO-H2O-HCl. *Geochimica et Cosmochimica Acta*, *48*(12), 2713–2722. https://doi.org/10.1016/0016-7037(84)90318-1

Liu, X., Zhang, Y., Wang, Y., Zhu, W., Li, G., Ma, X., Zhang, Y., Chen, S., Tiwari, S., Shi, K., Zhang, S., Fan, H. M., Zhao, Y. X., & Liang, X.-J. (2020). Comprehensive understanding of magnetic hyperthermia for improving antitumor therapeutic efficacy. *Theranostics*, *10*(8), 3793–3815. https://doi.org/10.7150/thno.40805

Luo, Z. (2016). *A Practical Guide to Transmission Electron Microscopy: Fundamentals* (First edition). Momentum Press. https://research.ebsco.com/linkprocessor/plink?id=9bce4cf8-f45c-3680-af97-ed49805770c9

Marghussian, V. (2015). 4—Magnetic Properties of Nano-Glass Ceramics. In V. Marghussian (Ed.), *Nano-Glass Ceramics* (pp. 181–223). William Andrew Publishing. https://doi.org/10.1016/B978-0-323-35386-1.00004-9

Markhulia, J. (2017, June 20). *CHEMICAL CO-PRECIPITATION SYNTHESIS AND CHARACTERIZATION OF POLYETHYLENE GLYCOL COATED IRON OXIDE NANOPARTICLES FOR BIOMEDICAL APPLICATIONS*. https://doi.org/10.5593/sgem2017/61/S24.007

Martinez-Boubeta, C., Simeonidis, K., Oró, J., Makridis, A., Serantes, D., & Balcells, L. (2021). Finding the Limits of Magnetic Hyperthermia on Core-Shell Nanoparticles Fabricated by Physical Vapor Methods. *Magnetochemistry*, *7*(4), Article 4. https://doi.org/10.3390/magnetochemistry7040049

Mathews, P. D., Patta, A. C. M. F., Madrid, R. R. M., Ramirez, C. A. B., Pimenta, B. V., & Mertins, O. (2023). Efficient Treatment of Fish Intestinal Parasites Applying a Membrane-Penetrating Oral Drug Delivery Nanoparticle. *ACS Biomaterials Science & Engineering*, *9*(6), 2911–2923. https://doi.org/10.1021/acsbiomaterials.1c00890

Mitra, S., Naskar, N., Reeves, A., & Chaudhuri, P. (2024). Chapter Twenty-Four—Prospects of mangrove-derived phytochemicals in cancer research. In R. C. Sobti, M. Watanabe, & A. Sobti (Eds.), *Biomarkers in Cancer Detection and Monitoring of Therapeutics* (pp. 499–532). Academic Press. https://doi.org/10.1016/B978-0-323-95114-2.00020-0

Mohallem, N. D. S., Silva, J. B., Nascimento, G. L. T., Guimarães, V. L., Mohallem, N. D. S., Silva, J. B., Nascimento, G. L. T., & Guimarães, V. L. (2012). Study of Multifunctional Nanocomposites Formed by Cobalt Ferrite Dispersed in a Silica Matrix Prepared by Sol-Gel Process. In *Nanocomposites—New Trends and Developments*. IntechOpen. https://doi.org/10.5772/51154

Mohammadi, H., Nekobahr, E., Akhtari, J., Saeedi, M., Akbari, J., & Fathi, F. (2021). Synthesis and characterization of magnetite nanoparticles by co-precipitation method coated with biocompatible compounds and evaluation of in-vitro cytotoxicity. *Toxicology Reports*, *8*, 331–336. https://doi.org/10.1016/j.toxrep.2021.01.012

Mondal, S., Manivasagan, P., Bharathiraja, S., Santha Moorthy, M., Nguyen, V. T., Kim, H.

H., Nam, S. Y., Lee, K. D., & Oh, J. (2017). Hydroxyapatite Coated Iron Oxide Nanoparticles: A Promising Nanomaterial for Magnetic Hyperthermia Cancer Treatment. *Nanomaterials*, *7*(12), Article 12. https://doi.org/10.3390/nano7120426

Mondéjar-López, M., García-Martínez, J. C., Gómez-Gómez, L., Ahrazem, O., & Niza, E. (2024). New gel from a water-soluble Carboxymethyl chitosan-Cinnamaldehyde Schiff base derivative as an effective preservative against soft rot in ginger. *Food Chemistry*, *461*, 140970. https://doi.org/10.1016/j.foodchem.2024.140970

Moore, E. (2016). *Fourier Transform Infrared Spectroscopy (FTIR): Methods, Analysis, and Research Insights*. Nova Science Publishers, Inc. https://research.ebsco.com/linkprocessor/plink?id=f1425012-8bde-3342-8a80-625b201de2db

Mosquera, E., Rosas, N., Debut, A., & Guerrero, V. H. (2015). Síntesis y caracterización de nanopartículas de dióxido de titanio obtenidas por el método de sol-gel. *Revista Politécnica*, *36*(3), Article 3.

Mourdikoudis, S., Pallares, R. M., & Thanh, N. T. K. (2018). Characterization techniques for nanoparticles: Comparison and complementarity upon studying nanoparticle properties. *Nanoscale*, *10*(27), 12871–12934. https://doi.org/10.1039/C8NR02278J

Niculescu, A.-G., Chircov, C., Bîrcă, A. C., & Grumezescu, A. M. (2021). Nanomaterials Synthesis through Microfluidic Methods: An Updated Overview. *Nanomaterials*, *11*(4), Article 4. https://doi.org/10.3390/nano11040864

Nomoev, A. V., Bardakhanov, S. P., Schreiber, M., Bazarova, D. G., Romanov, N. A., Baldanov, B. B., Radnaev, B. R., & Syzrantsev, V. V. (2015). Structure and mechanism of the formation of core–shell nanoparticles obtained through a one-step

gas-phase synthesis by electron beam evaporation. *Beilstein Journal of Nanotechnology*, *6*, 874–880. https://doi.org/10.3762/bjnano.6.89

Nuzhina, J. V., Shtil, A. A., Prilepskii, A. Y., & Vinogradov, V. V. (2019). Preclinical Evaluation and Clinical Translation of Magnetite-Based Nanomedicines. *Journal of Drug Delivery Science and Technology*, *54*, 101282. https://doi.org/10.1016/j.jddst.2019.101282

Odularu, A. T. (2018). Metal Nanoparticles: Thermal Decomposition, Biomedicinal Applications to Cancer Treatment, and Future Perspectives. *Bioinorganic Chemistry and Applications*, *2018*(1), 9354708. https://doi.org/10.1155/2018/9354708

Osaci, M., & Cacciola, M. (2017). Specific loss power in superparamagnetic hyperthermia: Nanofluid versus composite. *IOP Conference Series: Materials Science and Engineering*, *163*(1), 012008. https://doi.org/10.1088/1757-899X/163/1/012008

Pande, M., & Bhaskarwar, A. N. (2016). *Nanoparticles: Preparation and Characterization*. Momentum Press. https://research.ebsco.com/linkprocessor/plink?id=3ace7dca-8f0f-3631-8a38-a0ecd421c040

Park, J.-C., Ito, T., Kim, K.-O., Kim, K.-W., Kim, B.-S., Khil, M.-S., Kim, H.-Y., & Kim, I.-S. (2010). Electrospun poly(vinyl alcohol) nanofibers: Effects of degree of hydrolysis and enhanced water stability. *Polymer Journal*, *42*(3), 273–276. https://doi.org/10.1038/pj.2009.340

Pathak, T. K., Vasoya, N. H., Lakhani, V. K., & Modi, K. B. (2010). Structural and magnetic phase evolution study on needle-shaped nanoparticles of magnesium ferrite. *Ceramics International*, *36*(1), 275–281. https://doi.org/10.1016/j.ceramint.2009.07.023

Popescu, M. A. (2011). *Drug Delivery*. Nova Science Publishers, Inc. https://research.ebsco.com/linkprocessor/plink?id=b32a17df-387f-3e05-a241-fd1453c1a3dc

Predescu, A. M., Matei, E., Berbecaru, A. C., Pantilimon, C., Drăgan, C., Vidu, R., Predescu, C., & Kuncser, V. (2018). Synthesis and characterization of dextran-coated iron oxide nanoparticles. *Royal Society Open Science*, *5*(3), 171525. https://doi.org/10.1098/rsos.171525

Rabi, B., Essoumhi, A., Sajieddine, M., Greneche, J. M., Hlil, E. K., Razouk, A., & Valente, M. A. (2020). Structural, magnetic and magnetocaloric study of Ni0.5Zn0.5Fe2O4 spinel. *Applied Physics A*, *126*(3), 174. https://doi.org/10.1007/s00339-020-3344-8

Reddy, L. H., Arias, J. L., Nicolas, J., & Couvreur, P. (2012). Magnetic Nanoparticles: Design and Characterization, Toxicity and Biocompatibility, Pharmaceutical and Biomedical Applications. *Chemical Reviews*, *112*(11), 5818–5878. https://doi.org/10.1021/cr300068p

Rodríguez-Rodríguez, A. A., Moreno-Trejo, M. B., & Collins-Martínez, V. H. (2018, April 26). *Synthesis of MFe2O4 nanoparticles by the Oil-in-Water microemulsion reaction method and its exploration for photocatalytic water splitting*. http://cimav.repositorioinstitucional.mx/jspui/handle/1004/1783

Rodríguez-Rodríguez, A. A., Moreno-Trejo, M. B., Meléndez-Zaragoza, M. J., Collins-Martínez, V., López-Ortiz, A., Martínez-Guerra, E., & Sánchez-Domínguez, M. (2019). Spinel-type ferrite nanoparticles: Synthesis by the oil-in-water microemulsion reaction method and photocatalytic water-splitting evaluation. *International Journal of Hydrogen Energy*, *44*(24), 12421–12429.

https://doi.org/10.1016/j.ijhydene.2018.09.183

Rudawska, A. (2020). The Impact of the Acidic Environment on the Mechanical Properties of Epoxy Compounds in Different Conditions. *Polymers*, *12*(12), Article 12. https://doi.org/10.3390/polym12122957

Sabbas, N. P. (2014a). *Magnetic Nanoparticles: Synthesis, Physicochemical Properties and Role in Biomedicine*. Nova Science Publishers, Inc. https://research.ebsco.com/linkprocessor/plink?id=55144b54-e6cf-37a2-b7ad-740bc4c4dc6a

Sabbas, N. P. (2014b). *Magnetic nanoparticles: Synthesis, physicochemical properties and role in biomedicine* (p. 245).

Sabri, M. A., Umer, A., Awan, G. H., Hassan, M. F., & Hasnain, A. (2016). Selection of Suitable Biological Method for the Synthesis of Silver Nanoparticles. *Nanomaterials and Nanotechnology*, *6*, 29. https://doi.org/10.5772/62644

Salunkhe, A. B., Khot, V. M., Ruso, J. M., & Patil, S. I. (2016). Water dispersible superparamagnetic Cobalt iron oxide nanoparticles for magnetic fluid hyperthermia. *Journal of Magnetism and Magnetic Materials*, *419*, 533–542. https://doi.org/10.1016/j.jmmm.2016.06.057

Shih, K. (2013). *X-ray Diffraction: Structure, Principles, and Applications*. Nova Science Publishers, Inc. https://research.ebsco.com/linkprocessor/plink?id=c4b164bb-10e8-3519-b279-3e62d4478ef1

Simeonidis, K., Martinez-Boubeta, C., Serantes, D., Ruta, S., Chubykalo-Fesenko, O., Chantrell, R., Oró-Solé, J., Balcells, Ll., Kamzin, A. S., Nazipov, R. A., Makridis, A., & Angelakeris, M. (2020). Controlling Magnetization Reversal and Hyperthermia

Efficiency in Core–Shell Iron–Iron Oxide Magnetic Nanoparticles by Tuning the Interphase Coupling. *ACS Applied Nano Materials*, *3*(5), 4465–4476. https://doi.org/10.1021/acsanm.0c00568

Singh, R., & Bhateria, R. (2021). Core-shell nanostructures: A simplest two-component system with enhanced properties and multiple applications. *Environmental Geochemistry and Health*, *43*(7), 2459–2482. https://doi.org/10.1007/s10653-020-00766-1

Singh Yadav, R., Kuřitka, I., Vilcakova, J., Jamatia, T., Machovsky, M., Skoda, D., Urbánek, P., Masař, M., Urbánek, M., Kalina, L., & Havlica, J. (2020). Impact of sonochemical synthesis condition on the structural and physical properties of MnFe2O4 spinel ferrite nanoparticles. *Ultrasonics Sonochemistry*, *61*, 104839. https://doi.org/10.1016/j.ultsonch.2019.104839

Sivakumar, P., Ramesh, R., Ramanand, A., Ponnusamy, S., & Muthamizhchelvan, C. (2011). Synthesis and characterization of nickel ferrite magnetic nanoparticles. *Materials Research Bulletin*, *46*(12), 2208–2211. https://doi.org/10.1016/j.materresbull.2011.09.009

Smit, M., & Lutz, M. (2020). Polymer-coated magnetic nanoparticles for the efficient capture of Mycobacterium tuberculosis (Mtb). *SN Applied Sciences*, *2*(10), 1658. https://doi.org/10.1007/s42452-020-03403-9

Sohofi, N., Tavanai, H., Morshed, M., & Abdolmaleki, A. (2014). Electrospinning of 100% Carboxymethyl Chitosan Nanofibers. *Journal of Engineered Fibers and Fabrics*, *9*(1), 155892501400900110. https://doi.org/10.1177/155892501400900110

Soufi, A., Hajjaoui, H., Elmoubarki, R., Abdennouri, M., Qourzal, S., & Barka, N. (2021).

Spinel ferrites nanoparticles: Synthesis methods and application in heterogeneous Fenton oxidation of organic pollutants – A review. *Applied Surface Science Advances*, *6*, 100145. https://doi.org/10.1016/j.apsadv.2021.100145

Srivastava, Dr. N., & Srivastava, P. (2010). Realizing NiO nanocrystals from a simple chemical method. *Bulletin of Materials Science*, *33*, 653–656. https://doi.org/10.1007/s12034-011-0142-0

Suri, S. S., Fenniri, H., & Singh, B. (2007). Nanotechnology-based drug delivery systems. *Journal of Occupational Medicine and Toxicology*, *2*(1), 16. https://doi.org/10.1186/1745-6673-2-16

Svetlichnyi, V., Shabalina, A., Lapin, I. N., Goncharova, D., Velikanov, D., & Sokolov, A. (2017). Characterization and magnetic properties study for magnetite nanoparticles obtained by pulsed laser ablation in water. *Applied Physics A*, *123*. https://doi.org/10.1007/s00339-017-1390-7

Szczygieł, I., & Winiarska, K. (2014). Synthesis and characterization of manganese–zinc ferrite obtained by thermal decomposition from organic precursors. *Journal of Thermal Analysis and Calorimetry*, *115*(1), 471–477. https://doi.org/10.1007/s10973-013-3281-2

Taha, T. A., Elrabaie, S., & Attia, M. T. (2018). Green synthesis, structural, magnetic, and dielectric characterization of NiZnFe2O4/C nanocomposite. *Journal of Materials Science: Materials in Electronics*, *29*(21), 18493–18501. https://doi.org/10.1007/s10854-018-9965-4

Tai, M. F., Lai, C. W., & Abdul Hamid, S. B. (2016). Facile Synthesis Polyethylene Glycol Coated Magnetite Nanoparticles for High Colloidal Stability. *Journal of*

Nanomaterials, *2016*(1), 8612505. https://doi.org/10.1155/2016/8612505

Tanaka, N. (2014). *Scanning Transmission Electron Microscopy Of Nanomaterials: Basics Of Imaging And Analysis*. Imperial College Press. https://research.ebsco.com/linkprocessor/plink?id=32d85b89-4ede-3c83-9654-15363fed1c7f

Tasleem, S., Naeem, A., & Shaharun, M. S. (2013). *Zinc Ferrite Nanoparticle Synthesis and Characterization; Effects of Annealing Temperature on the Size of nanoparticles*. https://www.semanticscholar.org/paper/Zinc-Ferrite-Nanoparticle-Synthesis-and-Effects-of-Tasleem-Naeem/71b1d269890d58ca20086205e59d799b8ad5a507

Tiwari, A. (2010). *Polysaccharides: Development, Properties and Applications*. Nova Science Publishers, Inc. https://research.ebsco.com/linkprocessor/plink?id=08ce808c-1729-36cf-86e8-3f00721dcca5

Velásquez, A. A., Marín, C. C., & Urquijo, J. P. (2018). Synthesis and characterization of magnetite-maghemite nanoparticles obtained by the high-energy ball milling method. *Journal of Nanoparticle Research*, *20*(3), 72. https://doi.org/10.1007/s11051-018-4166-x

Vicente, A., Rivero, P., García, P., Mora, J., Carreño Puertas, F., Fernandez Palacio, J., & Rodríguez, R. (2021). Icephobic and Anticorrosion Coatings Deposited by Electrospinning on Aluminum Alloys for Aerospace Applications. *Polymers*, *13*, 4164. https://doi.org/10.3390/polym13234164

Xian, G., Kong, S., Li, Q., Zhang, G., Zhou, N., Du, H., & Niu, L. (2020). Synthesis of Spinel Ferrite MFe2O4 (M = Co, Cu, Mn, and Zn) for Persulfate Activation to Remove

Aqueous Organics: Effects of M-Site Metal and Synthetic Method. *Frontiers in Chemistry*, *8*. https://doi.org/10.3389/fchem.2020.00177

Xiong, F., Huang, S., & Gu, N. (2018). Magnetic nanoparticles: Recent developments in drug delivery system. *Drug Development & Industrial Pharmacy*, *44*(5), 697–706. https://doi.org/10.1080/03639045.2017.1421961

Yadav, A., Choudhary, P., Saxena, P., Rai, V., & Mishra, A. (2019). Spectroscopic analysis and temperature-dependent dielectric properties of bulk Ni–Zn ceramics. *Journal of Advanced Dielectrics*, *09*, 19500140. https://doi.org/10.1142/S2010135X19500140

Yang, R., Wei, T., Goldberg, H., Wang, W., Cullion, K., & Kohane, D. S. (2017). Getting Drugs Across Biological Barriers. *Advanced Materials*, *29*(37), 1606596. https://doi.org/10.1002/adma.201606596

Zainuri, M. (2017). Hematite from Natural Iron Stones as Microwave Absorbing Material on X-Band Frequency Ranges. *IOP Conference Series: Materials Science and Engineering*, *196*, 012008. https://doi.org/10.1088/1757-899X/196/1/012008

Zhang, H., Liu, X. L., Zhang, Y. F., Gao, F., Li, G. L., He, Y., Peng, M. L., & Fan, H. M. (2018). Magnetic nanoparticles based cancer therapy: Current status and applications. *Science China Life Sciences*, *61*(4), 400–414. https://doi.org/10.1007/s11427-017-9271-1

Zhou, G., Xu, S., Li, W., Yao, Q., & Zhang, D. (2016). *Research on the Preparation and Characterization of Magnetic Nanoparticles (MNPs) By Chemical Co-precipitation*. 175–180. https://doi.org/10.2991/icimm-16.2016.36

Zou, J., Gao, R., Fu, C., Cai, W., Chen, G., & Deng, X. (2018). Influence of Co ion doping on the microstructure, magnetic and dielectric properties of Ni1-xCoxFe2O4

ceramics. *Processing and Application of Ceramics*, *12*(4), 335–341.

9. Annexes

Annex 1. Calculus of magnetic nanoparticles synthesis

Molecular weights

$Fe(NO_3)_3 \cdot 9H_2O$: 403.95 g/mol

NaOH: 39.997 g/mol

$Zn(NO_3)_2 \cdot 6H_2O$: 297.5 g/mol

$Ni(NO_3)_2 \cdot 6H_2O$: 290.81 g/mol

Constants for an expected yield of 270–300 mg

$Fe(NO_3)_3 \cdot 9H_2O$ [2 mmol]: 0.8079 g in 100 mL

NaOH [5 M]: 2.0000 g in 10 mL DI (may vary, recommend measuring using pHmeter or pH papers)

Variables for an expected yield of 270–300 mg (in 30 mL each variable)

- x=0.25

$Ni(NO_3)_2 \cdot 6H_2O$ [0.75 mmol]: 0.2181 g

$Zn(NO_3)_2 \cdot 6H_2O$ [0.25 mmol]: 0.0744 g

- x=0.5

$Ni(NO_3)_2 \cdot 6H_2O$ [0.5 mmol]: 0.1454 g

$Zn(NO_3)_2 \cdot 4H_2O$ [0.5 mmol]: 0.1488 g

- x=0.75

$Ni(NO_3)_2 \cdot 6H_2O$ [0.25 mmol]: 0.0728 g

$Zn(NO_3)_2 \cdot 4H_2O$ [0.75 mmol]: 0.2231 g